An Implantable Low Pressure, Low Drift, Dual BioPressure Sensor and In-Vivo Calibration Methods Thereof

A Dissertation Presented for the

Doctor of Philosophy

Degree

The University of Tennessee, Knoxville

Chad Eric Seaver

December 2018

Copyright © 2018 by Chad E. Seaver
All rights reserved.

ACKNOWLEDGEMENTS

I am very grateful for the opportunity and tremendous support provided by my advisor, Dr. Mohamed Mahfouz. I would like to thank each member of my Dissertation Committee, including Dr. Fathy, Dr. Komistek, and Dr. Sharma. A very special thank you to Dr. James Killeffer for his years of patience and generosity in mentoring me in neurosurgery.

I am particularly grateful for the support of Arkis BioSciences, including data collection by student interns Tony Nguyen, Jon Dreitlein, and Alex Wright. I would like to extend a special thanks to Clif Moyers and Jim O'Hatnick for their encouragement and also for their support through RbM Services including my friend Dan Newby's assistance in sensor fabrication.

I would like to thank Dr. Marvin Sussman for taking a personal interest in this research, revealing prior publications, and providing perspective. I especially appreciate his encouragement and friendship. I also wish to thank Dr. Carlos Hakim for sharing his feedback on the device and methodology.

Finally, thanks to my family for their encouragement and support of this opportunity. Thank you to my mother and father, my two sons, and especially my wife for her enduring love after countless late nights and weekends of work.

ABSTRACT

The human body's intracranial pressure (ICP) is a critical component in sustaining healthy blood flow to the brain while allowing adequate volume for brain tissue within the rigid structures of the cranium. Disruptions in the body's autoregulation of intracranial pressure are often caused by hemorrhage, tumors, edema, or excess cerebral spinal fluid resulting in treatments that are estimated to globally cost up to approximately five billion dollars annually. A critical element in the contemporary management of acute head injury, intracranial hemorrhage, stroke, or other conditions resulting in intracranial hypertension, is the real-time monitoring of ICP. Currently, such mainstream clinical monitoring can only take place short-term within an acute care hospital. The monitoring is prone to measurement drift and is comprised of externally tethered pressure sensors that are temporarily implanted into the brain, thus carrying a significant risk of infection. To date, reliable, low drift, completely internalized, long-term ICP monitoring devices remain elusive. The successful development of such a device would not only be safer and more reliable in the short-term but would expand the use of ICP monitoring for the management of chronic intracranial hypertension and enable further clinical research into these disorders. The research herein reviews the current challenges of existing ICP monitoring systems, develops a new novel sensing technology, and evaluates the same for potentially facilitating long-term implantable ICP sensing. Based upon the findings of this research, this dissertation proposes and evaluates a dual

matched-die piezo-resistive strain sensing device, with a novel in-vivo calibration system and method thereof, for application to long-term implantable ICP sensing.

TABLE OF CONTENTS

Chapter One Introduction and General Information 1
Intracranial Pressure and Disorders Thereof 2
Standard Intracranial Pressure Measurement Techniques 7
Challenges of Intracranial Pressure Monitoring 12
Significance and Contribution 13
Chapter Two Literature Review 18
Overview 18
Direct ICP Measurement 18
Direct Fiber Optic Measurement 20
Direct Microstrain Measurement 23
Other Direct Techniques and Modern Approaches 28
Indirect ICP Measurement 30
Non-Invasive ICP Assessment 33
ICP Telemetric Approaches 37
Raumedic Neurovent-P-tel 41
Meithke Sensor Reservoir 43
Research Gap and Limitations 47
Chapter Three Materials and Methods 49
Overview 49
Requirements 50
Approach 55

Sensor Technology 55
Sensor System Design 82
Deployment and Implantation 93
Electronics Readout Overview 97
Methods 103
Simulation 103
Sensor Evaluation 104
Uncorrected Sensor Drift Assessment 104
System Calibrated Sensor Assessment 106
Chapter Four Results and Discussion 114
Sensor Simulations 115
Uncorrected Sensor Drift Results 122
System Calibrated Sensor Results 132
Non-Ideal Effects and Challenges 165
Chapter Five Conclusions and Recommendations 183
List of References 189
Appendix 204
Vita 209

LIST OF TABLES

Table 1 – Non-Invasive ICP Approaches 36

Table 2 – Key Requirements and Research Objectives Summary 56

Table 3 - Low power instrumentation amplifiers 102

Table 4 – Sensor bridge piezoresistance at 22.1°C 116

Table 5 – Sensor Pressure Range Verification 141

Table 6 – Sensor resolution summary 143

Table 7 – Accuracy measurements for sensors U1 and U2, n=100 144

Table 8 – System calibrated dual matched-die sensor results at gain ±20% 152

Table 9 - System calibrated dual matched-die sensor results for induced offset 154

Table 10 – Power consumption of transponder's main components. 163

Table 11 – Transponder primary component volumes 165

Table 12 – Sensor and supporting substrate cavity volume. 169

Table 13 – Research Objective Fulfillment 186

LIST OF FIGURES

Figure 1 – CSF generation within the brain. 3

Figure 2 – Axial MRI showing enlargement of the lateral ventricles due to elevated ICP. 5

Figure 3 - Intracranial pressure monitoring with a ventricular catheter. 8

Figure 4 – Fiber optic pressure sensor. 10

Figure 5 – Thermal map of primate brain for two frontal sections (14.3 and 0.3). 22

Figure 6 - Illustration of various ICP measurement techniques. 32

Figure 7 – Transponder described by Atkinson et. al. [84] 38

Figure 8 - Raumedic NEUROVENT-P-tel [38] 42

Figure 9 - The Miethke SENSOR RESERVOIR 44

Figure 10 – Conventional metallic micro-strain resistive pattern. 62

Figure 11 – Wheatstone pressure transducer comprising strain sensors. 67

Figure 12 - TE Connectivity 1630 70

Figure 13 – Amphenol All Sensors 30 INCH-D-MV pressure sensor die, approximately 2 mm^2. 73

Figure 14 – 30 INCH-D-MV side view at 40X (photo border provided for clarity) 76

Figure 15 - Amphenol sensor die deployment upon ceramic PCB with soldermask. 76

Figure 16 – Laser trimmed film compensation resistors. 77

Figure 17 – Amphenol published equivalent circuit. 81

Figure 18 – Derived Wheatstone bridge pressure sensor model. 81

Figure 19 – Illustrative cross-section concept of dual pressure sensors with each P1 and P2 cross-coupled to top-side and bottom-side dies. 83
Figure 20 – Cross coupled dual sensor configuration for error compensation. ... 85
Figure 21 - Independent dual sensor with absolute reference configuration for error compensation. 87
Figure 22 – Independent output dual sensors with common power/bias rails. ... 87
Figure 23 – Biopressure transponder deployment with ventricular catheter. 88
Figure 24 – Alternative transponder deployment with fluid bladder as a parenchyma pressure transducer. 90
Figure 25 – System deployment of biopressure sensor with reference fluid column and shunt integration (shunt peritoneal catheter shown). 92
Figure 26 – Transponder and readout deployment block diagram. 96
Figure 27 – Operational amplifier differential configuration. 98
Figure 28 – Instrumentation amplifier. 100
Figure 29 – Long term drift chamber with external and local power supply regulation and thermal stability with data acquisition system under UPS. . 105
Figure 30 – Front-end circuit for long-term cross-coupled sensor assessment. 107
Figure 31 – Dual biopressure sensor test bench with pressure source, precision power supply, instrumentation amplifier, and oscilloscope measurement. 108
Figure 32 – Isolation chamber with self-contained pressure source for offset testing. 110
Figure 33 – Front-end circuit for benchtop testing of system calibrated sensor. 111

Figure 34 – Piezoresistor temperature response 117
Figure 35 – Sensor bridge PSPICE simulation circuit for piezoresistor mismatch and temperature sweep. 118
Figure 36 – PSPICE simulation showing piezoresistance for R1 at 20°C, 36°C, 37°C, 38°C, and 40°C. 119
Figure 37 - PSPICE simulation showing bridge output of 329.076 µV for all temperatures 20°C - 40°C. 120
Figure 38 – Temperature gradient from sensor's Joule heating upon 37°C CSF. 122
Figure 39 – Laboratory setup for uncorrected long-term drift measurement of cross-coupled sensor. 124
Figure 40 – Long-term test sensor with pressure cylinder and read-out circuit. 125
Figure 41 – Uncorrected pressure sensor initial transfer function. 126
Figure 42 – Long-term uncorrected pressure sensor drift for 31 mm H_2O liquid (BLVR-L30D-B1NS). 128
Figure 43 - Uncorrected pressure sensor initial and 2.5-year transfer function. 129
Figure 44 – Six-month drift results for dual pressure sensor build 0517 131
Figure 45 – Custom dual biopressure sensor exploded illustration. 133
Figure 46 – Custom dual matched die biopressure sensor prototype showing absolute reference chamber and top-side dies therein. 135
Figure 47 - Custom dual matched die biopressure sensor prototype showing both independent chambers and top-side reference chamber. 137
Figure 48 – Custom dual matched-die sensor readout circuit. 138

Figure 49 – Custom dual biopressure sensor transfer function (Build 0517). ... 139
Figure 50 - +502 mm H_2O signal 142
Figure 51 - -499 mm H_2O signal 142
Figure 52 – Accuracy measurement for sensor U1, 150 mm H2O, n=100 samples 145
Figure 53 - Accuracy measurement for sensor U2, 150 mm H_2O, n=100 samples 145
Figure 54 – Precision measurement histogram for 150 mm H_2O and n = 100 .. 147
Figure 55 - Dual sensor die comparison for 80%, 100%, and 120% gain. 148
Figure 56 – Custom dual biopressure sensor system test bench. 149
Figure 57 – Reference reservoir for liquid fluid column. 150
Figure 58 - Isolation pressure chamber with self-contained pressure source. .. 150
Figure 59 – Vacuum pressure chamber measurement 156
Figure 60 – System calibrated dual sensor performance for 100 mm H_2O and induced gain shift. 157
Figure 61 - System calibrated dual sensor performance for 150 mm H_2O and induced gain shift. 158
Figure 62 - System calibrated dual sensor performance for 150 mm H_2O and induced offset shift. 159
Figure 63 – 5V front-end circuit design with V_o of 0-3.08 V supporting TI CC2541 161
Figure 64 – Initial outgassing of polyvinyl chloride (PVC) tubing. 168

Figure 65 – Bubble formation and air voids from advanced outgassing of tubing. 168
Figure 66 – Sensor cavity air-liquid transfer and bubble formation. 170
Figure 67 – COMSOL axisymmetric pressure gradient..... 174
Figure 68 - COMSOL axisymmetric water vapor concentration. 174
Figure 69 - COMSOL axisymmetric water volume fraction. 175
Figure 70 - COMSOL axisymmetric fluid velocity..... 175
Figure 71 – Top-side die metal migration from liquid media contact. 178
Figure 72 – Custom dual biopressure sensor absolute reference temperature response. 180

CHAPTER ONE

INTRODUCTION AND GENERAL INFORMATION

The human body is comprised of various organs that generate, or are subject to, a variety of pressures. These pressures are primarily induced externally due to gravity and include atmospheric compression and body weight opposition. However, there are also a wide range of pressures induced within the body itself. These pressures include those generated by the cardiovascular system, urinary system, digestive tract, musculoskeletal system, central nervous system, among others. Most of these pressures are critical for good health and require precise regulation. Blood pressure within the cardiovascular system and intracranial pressure (ICP) within the central nervous system, arising from the generation of cerebral spinal fluid (CSF), are two such components that must be precisely maintained. The ability to continuously monitor these pressures would allow for early detection and intervention in the event autoregulation becomes impaired. To date, long-term ICP sensing remains a challenge, primarily due to sensor inaccuracies over long periods of time.

With the advancement of micro-electro-mechanical system (MEMS) elements, low power inductively charged electronics, standardized wireless methods, as well as wireless hand-held computing devices, it has recently become feasible to potentially realize long-term telemetric implantables for physiological monitoring. ICP pressure is one such candidate that is desirable for telemetric monitoring. It

is among the most critical pressures found within the body whereby intracranial hypotension can lead to ruptured blood vessels and hematomas while hypertension can lead to decreased blood perfusion within the brain. Either case is quickly life threatening and affects one- to two-percent of the population congenitally by hydrocephalus, or is acquired due to brain tumor, traumatic brain injury, or from arachnoid villi damage from meningitis, for example. The work herein seeks to overcome the challenges of ICP monitoring where high-resolution pressures, on the order of several millimeters of water, must be measured in-vivo with low drift over long periods of time (e.g. years). This research undertakes a review of the scientific literature to assess the current challenges of ICP monitoring and to develop a new novel approach for overcoming the fundamental limitations of long-term implantable ICP sensing, particularly measurement drift. The goal of this work is for the research and initial evaluation of a novel biopressure sensor system to serve as a platform technology for accurate and clinically relevant long-term measurements of ICP.

Intracranial Pressure and Disorders Thereof

Pressure within the cranium is due to the arterial and venous pressure acting against the pressure head of the intracranial contents. Blood flow to the brain, characterized by cerebral perfusion pressure (CPP), is commonly calculated using ICP and mean arterial pressure (MAP) using the relationship CPP = MAP – ICP. Intracranial pressure is normally generated primarily from the formation of cerebral spinal fluid (CSF) and is a result of the pressure-volume relationship of

incompressible fluids within the semi-rigid intracranial compartment. Therefore, any changes in the volume of the intracranial contents alters ICP. CSF is primarily formed by the choroid plexus within the first and second lateral ventricles of the brain, illustrated in Figure 1, where it thereafter flows into the third and fourth ventricles. Flowing from the ventricles, CSF then surrounds the spinal cord and subarachnoid space, where it is reabsorbed by the arachnoid villi. CSF pressure varies in human beings, but generally falls within the range of 68 to 136 mm H_2O in normal adults in the recumbent position [1, 2] although some clinicians cite normal pressures as high as 180 mm H_2O or 200 mm H_2O [3, 4]. In the upright position, ventricular pressure is typically around atmospheric (i.e. ~0 mm H_2O) or even negative due to gravitational forces upon the spinal fluid column [4].

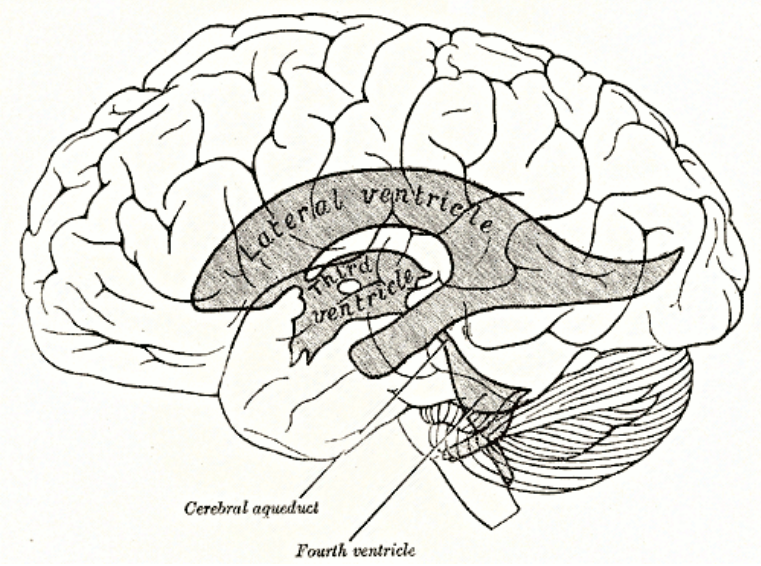


Figure 1 – CSF generation within the brain.

(Source: Gray's Anatomy of the Human Body, 20th edition)

Abnormalities occur when there is an over generation of CSF by the choroid plexus or a malabsorption of the fluid by the arachnoid villi, such as that with hydrocephalus. Abnormal pressures can also result when restrictions or obstructions in the fluid pathway retard or prevent CSF reabsorption. These obstructions can often be congenital but may also result from brain tumors or head trauma. Figure 2 shows an axial MR brain scan where enlargement of the lateral ventricles has occurred as a result of abnormally high ICP.

Koskinen showed that for pathological patients under study in the neuro-ICU, patients' average ICP was 249 mm H_2O, measured intraventricularly [5]. For hydrocephalus patients, who suffer from chronic intracranial hypertension (ICH), a CSF shunt is the most common treatment for maintaining normal pressure levels and for preventing dangerously high levels of ICP. A shunt diverts excess CSF to a resorptive site, commonly in the peritoneum, within a small catheter lumen including a pressure threshold check valve. Without a shunt, or equivalently in the case of a failed shunt (e.g. due to an obstruction), a patient's condition may quickly become life threatening as ICP overcomes MAP, thereby restricting CPP. Short of other interventions, such as 3rd ventriculostomy or temporary external ventricular drainage, untreated hydrocephalus is typically fatal [6, 7].

Lundberg additionally indicated severe ICP has been shown to extend even beyond 500 mm H_2O [8]. Young reported extreme ICP levels in excess of

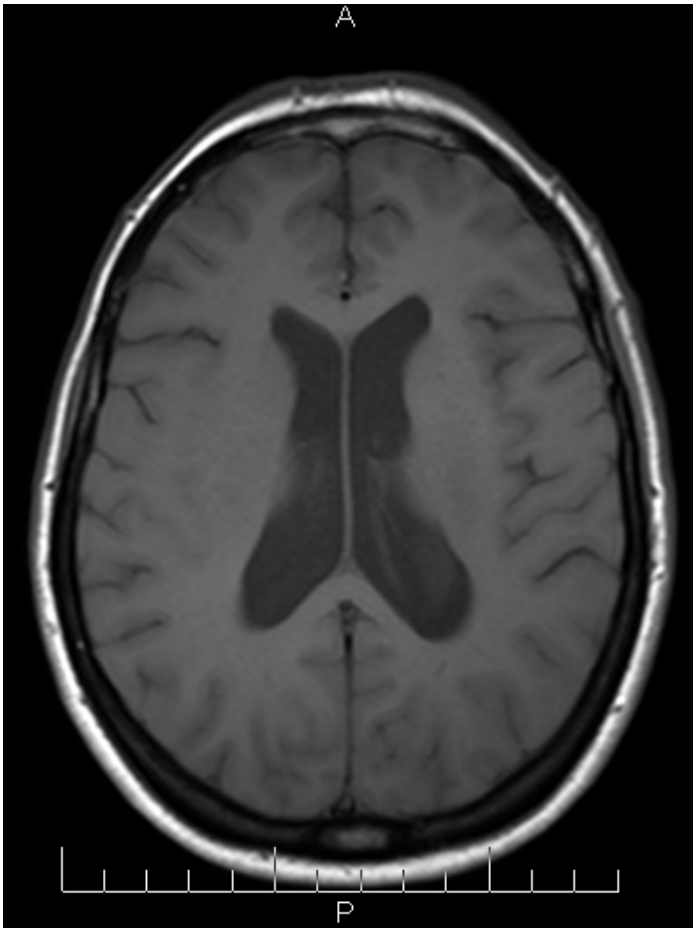


Figure 2 – Axial MRI showing enlargement of the lateral ventricles due to elevated ICP.

(Source: Neurosurgery Center of Colorado)

680 mm H_2O for severe head trauma patients who were provided atypical specialized treatments to maintain CPP above 60 mm Hg with notable success [9]. Nevertheless, for patients whose ICP exceeded 1,019 mm H_2O (i.e. 75 mm Hg), Young reported brain herniation and fatal outcomes within 24 hours. Regardless, the case studies by Young with ICP's above 500 mm H_2O represent acute head trauma cases and not chronically elevated ICP's typically associated with hydrocephalus.

Typical methods for assessing intracranial pressure require a surgical procedure to install a ventricular catheter through the skull and thereafter measuring CSF pressure with an external manometer. Another method involves the use of a tethered electrical or optical pressure sensor that can be inserted into the brain for localized in-vivo readings. For example, optical pressure sensors are commercially available with a pressure transducer located at the tip of a fiber optic strand. Fiber optic instrumentation is used to provide pressure read outs based upon interferometer techniques to detect translation of the pressure transducer's diaphragm.

While these methods provide in-situ assessment of intracranial pressure, they do so most invasively and only upon a temporary basis within a surgical or intensive care setting. Typically, these types of pressure measurements are only carried out after a variety of other expensive diagnostics, such as medical imaging, have been exhausted in an attempt to explain the root cause of a patient's illness. Once it is determined to proceed with invasive pressure measurements, the

patient is often sedated while the sensing element is surgically installed. Thereafter, the pressure sensor element remains temporarily tethered to the patient through a bore hole in the skull. It is then necessary to place the patient under continuing hospital care in order to monitor the pressure over time. Therefore, these assessment techniques are unfortunately the most invasive and expensive approach possible. They furthermore increase patient risk with the potential of surgical complications, such as infection, especially over prolonged periods [10]. Since intracranial pressure can rapidly rise due to an adult's fixed intracranial volume, patients can quickly reach a critical state by the time all preliminary diagnostics have proven negative. Therefore, a need exists for high risk patients to be able to routinely and non-invasively monitor ICP to prevent life threatening emergencies and to allow further research into ICP under various conditions or activities. The work of this dissertation seeks to advance the field of research of this problem by investigating the limiting factors preventing long-term ICP monitoring and potential solutions thereof.

Standard Intracranial Pressure Measurement Techniques

The "gold standard" method of assessing ICP is through the introduction of a catheter, connected to a manometer, into the ventricles of the brain by way of a bore hole though the skull, as shown in Figure 3 [11]. A saline solution is used, if needed, as a translating fluid medium to allow external alignment of the measuring solution with that of the ventricular cavity. Fluid elevation beyond that of the internal cavity ceiling level is then measured to arrive at a pressure relative

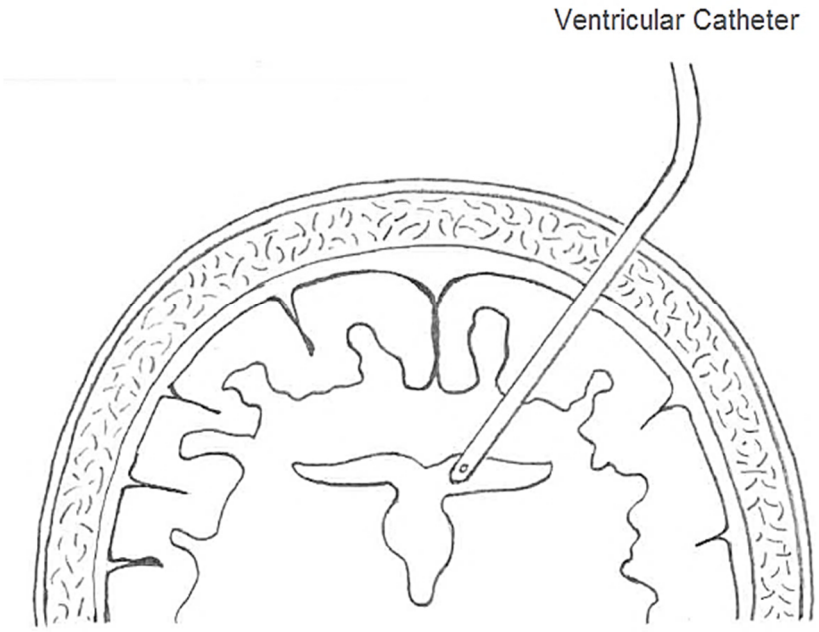


Figure 3 - Intracranial pressure monitoring with a ventricular catheter.

to atmospheric. This technique allows for robust pressure measurement that is immune to drift and which also facilitates drainage relief as necessary. However, the method is also the most invasive of all techniques with studies indicating up to an approximate 10% infection rate [12, 13].

A popular alternative to manometer pressure measurements is that provided by optical pressure transducers, such as those marketed by FISO [14] or Natus [15]. In this technique, a fiber optic strand with a pressure sensitive tip is inserted into a ventricular catheter or into the parenchyma and is read out by interferometer instrumentation bedside to the patient. Figure 4 shows such a fiber optic sensor whereby the strand is configured with a pressure sensitive membrane that translates relative to incident pressure. A collimated light source present within the fiber and reflecting off the sensor membrane varies the amount of reflective constructive or destructive interference. Therefore, the amplitude of the reflected light received at the proximal end is proportional to the pressure present upon the membrane tip. Drift and temperature effects have been widely reported with such sensors, however [2, 11].

Since the fiber optic method is optically based, using interferometry against an absolute pressure reference, and given there are no present devices with temperature sensing and correction, the pressure drifts with temperature. Drift reported for fiber optic pressure sensors may predominately be due to the sensor being “zeroed” ex-vivo at room temperature and then actual pressure assessments taken in-vivo at a temperature of approximately 37°C. Additionally,

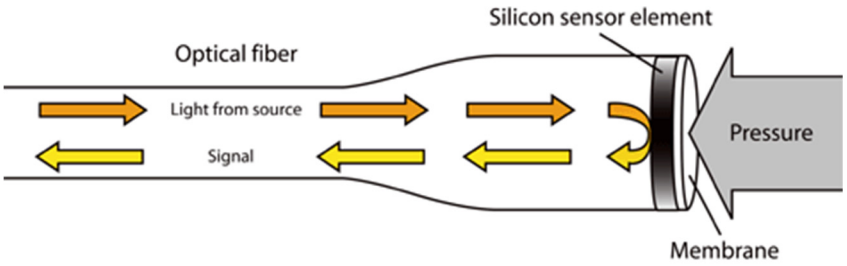


Figure 4 – Fiber optic pressure sensor.

(Source: Sensors by Questex Media Group LLC)

since these types of sensors typically deflect more than the thickness of the pressure diaphragm itself in order to reach desired sensitivities, the diaphragm operates within a non-linear range of deflection, which can extend into plasticity and result in hysteresis. Piper reported that their data indicated more than half of 34 fiber optic pressure transducers explanted had zero drift in excess of 40 mm H_2O [11].

In addition to fiber optic pressure readout systems, additional prevailing techniques include the use of an implantable strain gauge inserted into the brain's ventricles or parenchyma. Commercial offerings, such as those manufactured by Codman (under Integra Life Sciences) [16], offer a titanium probe with a side sensor providing electrical communication of pressure from the transducer to a bedside readout system. The Codman sensor consists of a solid state piezoresistive diaphragm and a Wheatstone bridge readout circuit [2]. As pressure modulates the diaphragm, induced strain changes the resistive properties of the material. The Wheatstone circuit converts this variable resistance into a proportional electrical current representative of the sensor's incident pressure. Advantages of this silicon technique include the option of temperature compensation based upon in-vivo silicon bandgap measurements. Assessments of the Codman strain-based sensor (also referred to as a microstrain device) have shown minimal drift, an average of 12 mm H_2O, and with pressures that correlate accurately with direct intraventricular ICP measurements [2, 5].

While other methods of ICP exist, including qualitative non-invasive techniques discussed within the Literature Review, the formerly described intraventricular catheter manometer, fiber optic sensor, and strain gauge sensor comprise the extent of prevalent and contemporary means of quantitative clinical assessment.

Challenges of Intracranial Pressure Monitoring

The primary challenge of monitoring ICP is accuracy balanced against risk. The most accurate methods are invasive, ranging from lumbar puncture to various cranial access approaches, including ventriculostomy. Accuracy is diminished by pressure sensor drifts, which have been shown to range from 1 - 3 mm Hg (14 – 41 mm H_2O) in just five days, significantly reducing clinical efficacy, especially for longer term use [29]. Lumbar puncture has severe limitations with accuracy [17]. Ventricular cannulation remains the gold standard for the most accurate ICP, but carries the highest risks, which are associated with brain penetration (e.g. placement, hemorrhage, etc.) and infection. Infection rates for a ventriculostomy currently range from 8 – 10% [12, 13]. However, rates for intraparenchymal sensing reside at approximately only 1 - 2% [18]. Other invasive methods, such as subarachnoid, subdural, and epidural devices have proven unreliable and are not commonly used in clinical practice [19]. In all invasive methods, with exception to telemetric sensors which are also currently limited in accuracy, the sensor is tethered to a bedside receiving unit, limiting ambulation and increasing infection risks. With regard to non-invasive approaches, all are currently

qualitative, at best, as Robba recently summarized, there were no prevailing non-invasive techniques to justify substituting for current invasive approaches [20].

Significance and Contribution

Hydrocephalus is presently reported to congenitally afflict between 0.5 to 3 out of every 1,000 live births [21, 22, 23, 24]. However, the disorder can also be acquired from pathologies such as brain tumors, head injury, meningitis, or as a result of intracranial hemorrhage, which altogether represents about 40% of all cases [25]. Procedural statistics from the American Association of Neurological Surgeons (AANS) estimated approximately 70,000 U.S. shunt procedures were performed in 2011 while the Hydrocephalus Association currently reports over one-million people in the U.S. are living with the disorder [24, 26]. Procedural costs in the U.S. have been estimated at an average $35,816 per admission thereby placing the total cost burden in the U.S. into the billions of dollars annually [27].

Although credited to Nulsen and Spitz in 1951 for the first fully internalized shunt, Richard Ames initiated what has now became the most prevalent shunt of modern times when he first implanted the ventriculoperitoneal (VP) shunt in 1958 comprised of silicone rubber [28]. Silicone was first implanted via a shunt by Pudenz in 1957 for the lesser common, at least in the U.S., ventriculoatrial shunt [29]. Nine years thereafter Ames reported promising results, for an otherwise typically fatal disorder, indicating successful VP shunt implants in an additional

120 patients [30]. Still today, shunts are the predominant lifesaving treatment for hydrocephalus, yet unfortunately have about a 50% failure and revision rate by the second year of implantation and 70% to 88% by year ten [31, 32, 33, 34].

Shunt failure is commonly associated with the onset of a headache and can thereafter quickly turn lethal [35, 36]. However, headaches are also typical of shunt mis-adjustment resulting in either under-drainage or over-drainage. Antes et. al. recently described that shunt malfunction, as well as under- or over-drainage, is difficult to diagnose and with shunt radiography and cranial imaging often remaining inconclusive [37, 38]. The problem is further aggravated when a patient is not in a state to sufficiently describe their symptoms. Verification of intracranial pressure then entails costly and risky invasive techniques for the measurement of ICP, as described in detail within the Literature Review. Such invasive techniques are the only current and clinically accurate means of assessing ICP, either for shunted patients suspected of shunt malfunction or for patients initially succumbing to intracranial hypertension for other reasons (e.g. brain trauma, lesions, edema, hemorrhage, etc.).

The benefits of being able to accurately and telemetrically measure ICP are numerous and immense. Within the literature, many investigators have considered ICP-guided valve adjustments by using telemetric ICP measurements as one of the most forward-looking advancements in hydrocephalus management [39, 40, 41]. Benefits are obvious for diagnosing potentially dangerous, yet unspecific headaches, particularly for those whose clinical

symptoms cannot be easily correlated to over drainage or underdrainage [42]. Authors have cited a long-standing need for telemetric ICP technology which would reduce costly imaging dependency for patient monitoring and obviate the need for additionally implanted shunt devices [43, 44]. Furthermore, ICP surveillance for patients who have suffered from traumatic brain injury (TBI) has been one of the most intended indications for long-term ICP measurement. Latent ICP peaks and the development of secondary hydrocephalus could be recognized earlier with regular monitoring to reduce the chances of further brain damage [37]. Moreover, verification of shunt alternatives, such as endoscopic third ventriculostomy (ETV) could be more efficiently enabled to distinguish ETV responders versus non-responders as shown by several recent case studies [37].

As shown in the Literature Review, pressure measurement accuracy has been, and remains, the limiting factor for the deployment of a long-term ICP device. Even for clinically current mainstream tethered devices, such instrumentation is limited by so-called “zero drift” even though it may be from baseline or sensitivity drift, or both. Drifts of 1-3 mm Hg (i.e. 14 – 41 mm H_2O) have been reported over the course of just five days for prevailing ICU tethered instrumentation, diminishing clinical usefulness [45]. Recent commercial attempts for wireless ICP sensor implants have validated the needs of the market for telemetric ICP assessment. However, clinical reviews of the commercialized technology have shown that marked and unpredictable drifts in accuracy limit broad use, rendering such implantable sensors unreliable over the long-term [38].

Nonetheless, these reviews state that effective ICP monitoring over long periods outside the clinic is highly desirable and beneficial for optimizing treatment. In a 2016 review, Robba summarized there were no then-current non-invasive techniques accurate or established enough to substitute for current invasive measurements [20]. Subsequent reviews of the literature and industry performed herein have concluded the same, as of time of writing.

Long-term pressure sensor drift is the persistent culprit that prevents the much-needed diagnostics for millions of people suffering from hydrocephalus, traumatic brain injury (TBI), and other causes of intracranial hypertension. A recent paper reviewing the challenges and state of the field for enabling chronically implantable pressure sensors found it crucial to have a means of drift compensation circuits or zeroing functions to provide correction [46]. Described and researched herein is a novel solution for non-invasive offset and gain calibration based upon dual matched biopressure sensors utilizing an in-vivo hydraulic reference for negating sensor drift. The research described herein resulted in the award of United States patent 9,668,663, having been reviewed, in light of the prior art, for novelty, inventive step, and utility [47]. The device and method utilizes two matched silicon piezoresistive strain sensors and a common gas reference to facilitate corrected ICP measurement by one sensor based upon an in-vivo reference measurement from the other. The device confronts reference degradation and other sources of potential drift in common-mode to first reduce drift and then to leverage matched sensor die characteristics for

applying correction coefficients measured by one sensor for application to the other. Deployment of the sensor would allow forthcoming patients to calibrate the wireless sensor by either using a two-position method (e.g. supine to upright) or by utilizing natural changes in barometric pressure.

CHAPTER TWO

LITERATURE REVIEW

Overview

Over the past decade several authors, including Wiegand [17] and Raboel [48], have provided comprehensive reviews of the methods and instrumentation for measuring ICP. Hawthorne and Piper [49] published an extensive review in 2014 focusing upon ICP for traumatic brain injury (TBI), including historical perspectives citing Alexander Monro's (1697–1767) original publications on intracranial contents. In 2017, Zhang et. al. [18], published what is today's latest review, covering a growing set of research earnestly seeking improvements in ICP instrumentation. The literature review herein summarizes the present technological state of ICP instrumentation, extending beyond the latest published reviews, with a particular emphasis on the research and development of completely implantable transponder approaches. This chapter organizes the literature survey into both direct methods for measuring ICP (all of which are invasive or initially invasive) and indirect methods in which physiologically related measurements may be proportional to actual ICP.

Direct ICP Measurement

Early direct measurement techniques for assessing ICP was pioneered by Lundberg and described in his landmark 1960 publication [8] for the continuous pressure monitoring of 130 patients. His technique employed a saline based

subdural pressure transducer deployed via ventricular cannulation. Wiegand, Raboel, Hawthorne, and Zhang all ascribe intraventricular monitoring as the enduring gold standard of modern day accurate ICP measurement. Zhang's assessment attributed invasive methods, such as intraventricular monitoring, as the most accurate of measuring ICP. Nevertheless, all agree of its shortcomings with regard to infection rates over time, the potential for brain hemorrhage, and the difficulty of successfully performing a ventriculostomy under elevated ICP where a deviated or slit ventricle may be present.

Alternatively, modern day electrical based pressure probes may be utilized such as the fiber optic [15] or electrical impedance strain transducer [16]. These sensors can be used either within the ventricle or the parenchyma. Luerssen described that these modern-day parenchymal sensors are comparable with that of the intraventricular hydrostatic methods and that the complication rate is lower due to the small diameter of the probes and lack of fluidic coupling [50]. Luerssen cites Pople [51] and Shapiro [52] as two large studies resulting in less than a one-percent infection rate for pressure measurements taken within the parenchyma. For ventricular cannulation, however, Luerssen cites several studies indicating infection rates approaching ten percent [12, 13]. He describes the risks of infection increasing with duration of monitoring and for this reason should only be used for as brief a period as possible. He further cited studies showing that prophylactically changing the ventricular catheter used for pressure measurement did not reduce the risk of infection.

Direct Fiber Optic Measurement

Fiber optic pressure transduction utilizes a thin diaphragm, often constructed from a silica fiber itself, comprising a sealed cavity in order to measure diaphragm deflections from incident pressure against an absolute pressure source. Optical interferometric techniques are used in order to measure the diaphragm translation. Piper et al. questions, however, the efficacy of the fiber optic parenchymal or intraventricular pressure probes as a means of accurate direct measurement. Their research found drifts for the Camino fiber optic system in excess of 40 mm H_2O for 50% of the pressure probes tested within a period of days [11]. While the manufacturer of the sensor studied specifies an upper bound on drift of ±27 mm H_2O for day one and 13.6 mm H_2O for each day thereafter, Piper claims this is unacceptable for clinical use. Further, researchers have even confirmed zero drift in excess of the specifications, with average daily drifts of 43.5 mm H_2O, in a study of 136 Camino fiber optic sensors [53]. Such large drifts were also found in an additional study of 1,000 clinical cases utilizing the Camino monitor with 87% of the cases drifting from -231 mm H_2O to 285 mm H_2O over a mean period of only 58 hours [54].

The study by Piper et. al. showed significant drift bias with a dependence on temperature for the fiber optic sensor. Studies have indicated a potential reason for such clinical drift is that the absolute pressure sensors are calibrated (i.e. “zeroed”) ex-vivo at room temperature (e.g. ~20°C) and then measured in-vivo at body temperatures, typically at 37°C [55]. A temperature coefficient of 4 mm

H_2O per °C likely results in a significant pressure error versus the calibration [11]. For a 17°C temperature shift, a 68 mm H_2O error would result. However, once in the brain, temperatures are relatively stable. Figure 5 illustrates temperature measurements taken in over 100 sites in 16 monkeys involving 347 experiments [56]. The values shown are site temperature measurements less aortic arterial blood temperature (all positive values). From the brain's surface to its ventricles, a gradient of 0.4°C was documented. Brain temperatures shifts were found to overall closely track venous blood in the right atrium. From sleep to arousal, brain temperature increases of approximately 0.2°C were found.

While pressure sensor inaccuracy, particularly at time of implant, likely occurs as a result of the fiber optic's thermal coefficient, there are other possible factors that may explain post-implant drift as well. Degradations resulting from mechanical drift mechanisms of the optical diaphragm material, readout electronics, and the systems interconnects may each further contribute to drift over time. For sufficient sensitivity, the optical diaphragm must be very thin. However, pressure deflections may often be larger than the thickness of the material itself. While small deflections can be predicted linearly as with a normal round circular plate [57], large deflections quickly turn non-linear [58] and can extend into plasticity for the material. Once the deflections become plastic, distortion effects occur where deformity can result in hysteresis and therefore drift. Additionally, atmospheric pressure changes over the course of in-vivo measurements have also been suggested as possible drift factors in the Camino

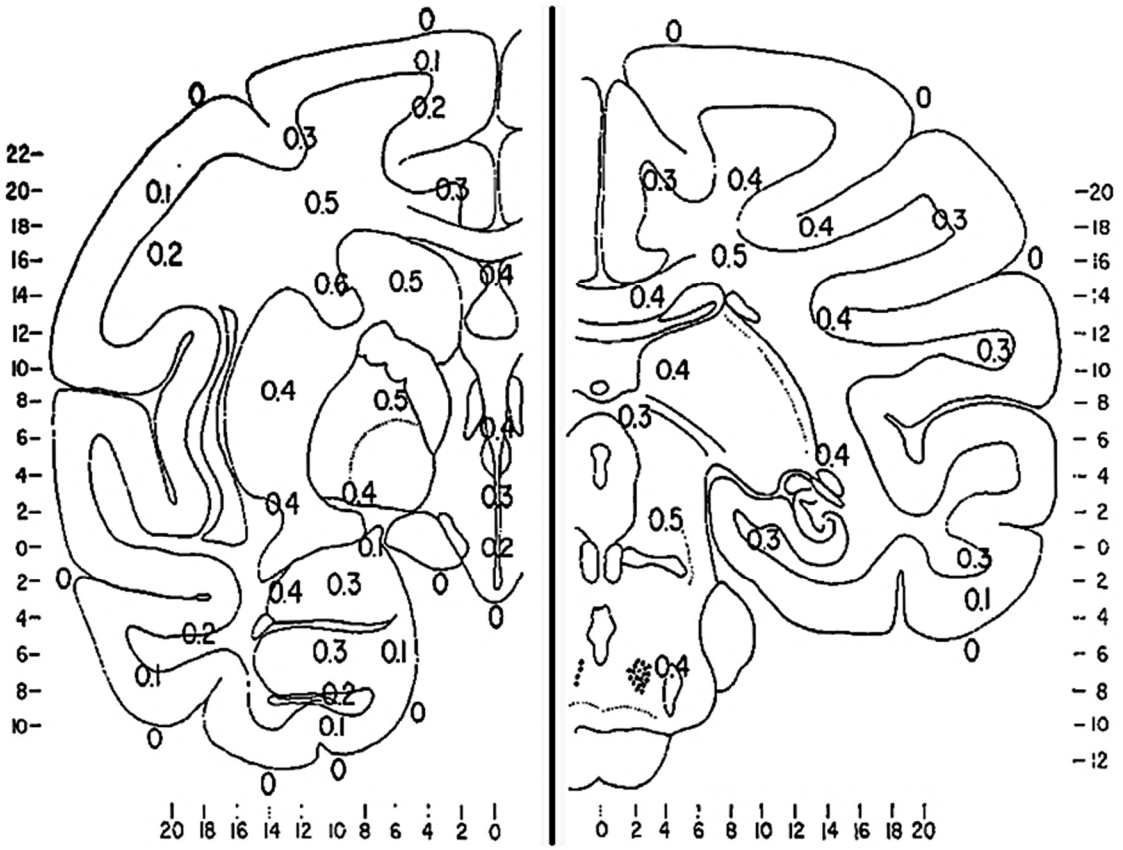


Figure 5 – Thermal map of primate brain for two frontal sections (14.3 and 0.3).

(Source: The American Journal of Physiology, Hayward and Baker, 1968)

sensor system, which are likely given its measurements are relative to a single absolute reference source [59].

Direct Microstrain Measurement

In contrast to the direct fiber optic intraventricular or parenchymal probe reviews, microstrain based sensors (i.e. piezoresistive pressure sensors) have received relatively positive appraisals within the literature. Koskinen performed a prospective study using the Codman Microsensor System (i.e. microstrain sensor) with 128 patients whereby zero drift was measured upon explantation [5]. The study additionally performed 469 measurements on 22 patients that also simultaneously used an intraventricular manometer for comparison. Results were shown for the 22 patients to have an average ICP of 249±4 mm H_2O measured intraventricularly. The microstrain based device produced an average of 258±3 mm H_2O over the range of patient ICP. The overall mean drift across the span of 7.2 ± 0.4 days was reported at 12 mm H_2O (i.e. 1.67 mm H_2O per day) with bounds less than ±27 mm H_2O in 79% of the devices. Koskinen reported the findings from a clinical point of view as acceptable and that the drift was low. A separate study of 88 patient cases utilizing the Codman Microsensor System in two separate neurointensive care units also found a mean drift of ±27 mm H_2O over a mean monitoring time of 108 hours [60]. An additional study further confirmed similar performance in 60 cases using the Codman ICP monitor whereby 43% of the cases demonstrated essentially zero drift while another 40%

was within ±14 mm H_2O. Maximum drift in all cases was reported to be 41 mm H_2O [61].

Spiegelberg also produces brain pressure monitors based on strain gauge technology, but with a different approach allowing in-vivo recalibration. The Spiegelberg monitor utilizes a sealed disposable air-pouch catheter transducer which is semi-inflated by an accurately calibrated air pump [62]. The air pouch catheter may be placed intraventricularly or within the parenchyma and further provides simultaneous CSF drainage via a separate yet integrated lumen. The resulting internal air pouch pressure is measured against the pump pressure to deduce ICP. The advantage is two-fold: 1.) the pressure sensor remains ex-vivo, whereby it can be recalibrated without need to remove the catheter, and 2.) the system can optionally facilitate brain compliance measurements by further displacing a small portion of brain volume (<0.1 ml) while another sensor measures the ensuing rise in ICP. Drifts for the Spiegelberg brain pressure monitor have been shown to be ±41 mm H_2O over 28 days [63].

Another ICP monitor also employing strain gauge technology is the LiquoGuard®7 manufactured by Möller Medical, introduced in 2011 following the original LiquoGuard. The LiquoGuard7 is similar to Spiegelberg's ICP monitor, allowing for simultaneous ICP measurement while draining CSF. However, the LiquoGuard7 is unique in that it regulates drainage via a closed-loop control system comprising ICP measurement feedback to maintain a desired pressure setpoint within the brain [64]. In this way, the system relieves intracranial

hypertension by controlling the drainage of CSF electronically, not by gravity alone. The benefit of this feature over other external ventricular drainage (EVD) systems is that there is no need to level a burette to control CSF pressure and flow. Therefore, patient ambulation is less restricted. For reliability and safety, the monitor incorporates redundant systems for sensing pressure utilizing two separate and independent strain gauge sensors each with independent processing circuits. The sensors are integrated into the CSF drainage lumen and attached to the patient at the level of the Foramen of Monro [65]. Optionally, the control system may be simultaneously connected to a separate ICP monitoring system for the measurement of ICP under conditions such as slit ventricles. The system modulates CSF drainage, based on pressure sensor feedback, by mechanically constricting its CSF drainage lumen using a pinch valve. CSF flow is gravitationally driven by the pressure difference between that of the ICP and a burette, or drip chamber, located at an elevation set lower than a patient's ventricles [66]. However, in a regulatory disclosure of the device, a peristaltic pump is described as being used when ICP exceeds a preset threshold [67]. Drift of the device is largely unreported although the manufacturer indicates the device drifts less than 14 mm H_2O under long-term testing.

Samaun et. al. [68] described some of the early work of silicon microstrain sensing for biomedical instrumentation, in particular for intravascular cardiac measurements. In their work they developed a thin silicon pressure diaphragm for the measurement of low stress with orthogonally oriented p-type implanted

piezoresistors. They go on to describe proper orientation for achieving magnification of stress measurement through the use of a bridge network in which two resistors decrease resistance upon induced strain while the other two likewise increase. Properties of pressure detection with diaphragm mechanics were also thoroughly described in which sensitivity increases by the square of the ratio of the diameter to the diaphragm's thickness. Additionally, linear regions of operation were described to be limited to about 40% deflection compared to the thickness. The researchers fabricated two piezoresistive sensors in which a sensitivity of 83 μV/Vsupply/mmHg and 14 μV/Vsupply/mmHg was achieved for diaphragm diameters of 1.2 and 0.5mm, respectively. After calibration and temperature compensation their work resulted in pressure sensors accurate to within 1 mmHg (13.6 mm H_2O) and with a range of up to 150 mmHg (2,039 mm H_2O). However, Samaun described drift issues with the silicon microstrain sensing technique where temperature sensitivity of the diffused piezoresistors was significant, but correctable. Additionally, Samaun found that mechanical creep due to different expansion coefficients between the sensor and mounting also contributed to drift over time and could very well dominate long-term drift.

Yurish [69] reviewed a variety of techniques concerning the readout of piezo-resistive strain sensors. His review covered high end analog to digital approaches and more cost sensitive microcontroller readout techniques. However, he cautioned against clock trigger noise affecting readout with direct

microcontroller techniques. Yurish provided an overview of modern-day application specific integrated circuits (ASIC) available through commercial means for the dedicated readout of microstrain sensors. Most of the ASICs provided digital outputs via either I^2C or SPI. He cited Smartec as offering a pulse width modulated (PWM) output, but that it was only compatible with resistive bridges ranging from 10Ω to 250Ω. Yurish noted that often, for remote sensing applications, the sensor's signal is converted to a frequency or duty cycle signal. Yurish's work consisted of developing a variable frequency output, representative of the entire bridge resistance, with a variable duty cycle representative of the bridge's unbalance for a very wide variety of bridge parameters. In this way, Yurish approached the problem of bridge temperature variation by encoding the common mode effects into the circuit's frequency output and the bridge's strain signal into the duty cycle.

Similar to Yurish, Crescini et. al. [70] also developed a readout circuit for a piezo-resistive pressure sensor, but with the intentions of high temperature applications. Crescini's readout circuit measured the overall bridge resistance of the sensor and encoded this into an output square-wave carrier frequency. The duty cycle of the square wave depended upon the imbalance within the bridge, representing the incident pressure. Crescini, in agreement with Yurish, explained the advantage of such an approach in that the electronics could be safely located away from the sensor with a minimal degradation in accuracy. Important to Crescini's application was that the implied temperature was encoded by the

carrier frequency. Crescini claimed the sensor's output transmission was highly noise-immune and could be directly interfaced to a microcontroller for A/D conversion.

Other Direct Techniques and Modern Approaches

Capacitive based sensors are not currently prevalent within clinical practice for ICP measurement, but nevertheless have been attempted in the past and are a topic of study within the bioMEMS area of research. George, et. al. recently described fabrication of a micro-electro-mechanical (MEM) based capacitive catheter sensor for ICP measurement [71]. In this type of sensor, metal upon a silicon die was used to form a variable capacitor whereby one electrode was fixed and a second was moveable in response to fluid pressure. George reported typical sensitivities for such sensors on the order of tens to hundreds of atto Farads per millimeter of mercury (i.e. 13.6 mm H_2O) with a fabrication tolerance of only about ±5%. George went on to summarize that not only was the sensitivity of their device low and not well controlled, but that a large offset was present as well. It is likely that George's results are indicative of why such sensors are not as prevalent within the industry as strain and optical interferometry methods. Stanford researchers Chen et. al. reported improved sensitivity gains utilizing a MEMS structure configured in a distributed resonant tank circuit fabricated from styrene butadiene styrene (SBS) elastomer [72]. The sensor was remarkably small at only 1 x 1 x 0.1 millimeters. The team overcame traditional operating frequency limits and deployed the sensor in-vivo in a rat.

One issue, however, was drift in capacitance values that resulted from measurement cycling. Additionally, there was drift due to the slow diffusion of water vapor through the polyimide substrate and adhesives, which caused a gradual decrease of the sensor's resonant frequency. The diffusion of water into the material likely altered the material's permittivity causing an increase in the effective permittivity between substrate layers. This drift mechanism has also been described by others, including most recently by Behfar [73]. Capacitive based biopressure sensors for low-pressure measurements (i.e. <100 mm H_2O) have additionally been subject to drift due to small amounts of biomatter accumulation, particularly for sensitivities less than a femto-Farad per millimeter of mercury.

One successful deployment of capacitive based pressure sensing, however, is in the case of the CardioMEMS™ EndoSure™ sensor [74]. This sensor represents the latest commercialization work for wireless sensing of cardiovascular pressure monitoring, which incorporates a MEMs based capacitive pressure cell. The sensor is installed with a stent graft during endovascular repair and is entirely passive, consisting only of an inductor, capacitor, and a diode. The sensor operates via ex-vivo wireless power stimulation, which results in a resonant frequency proportional to pressure induced capacitance. The resonant frequency is detected by an external radio receiver, which typically results in a sensitivity of 10 kHz per millimeter of mercury (i.e. 13.6 mm H_2O) [75]. Allen also reports that typical frequencies for such a sensor operates around 30 to 40 MHz

and with Q-factors of approximately 50. He indicated ex-vivo readout distances of approximately eight inches. While the EndoSure device provides a novel means of cardiovascular pressure interrogation, the pressures levels associated with blood pressure only begin near the maximum of those necessary for ICP.

Indirect ICP Measurement

Indirect methods of assessing ICP are based upon measuring related physiological parameters that correlate to true ICP. Indirect techniques may be either invasive or non-invasive. This section of the literature review surveys invasive means for indirect ICP assessment while the next section surveys non-invasive indirect methods.

The oldest known method of ICP measurement utilizes lumbar puncture and a manometer while a patient carefully lies in a lateral recumbent position [76]. Commonly, the opening pressure (i.e. initial pressure) and closing pressure (i.e. after drainage of CSF) are used as potential clinical indicators of intracranial hypertension. This technique works for communicating CSF (i.e. without obstruction) and provides an indirect measurement of ICP, albeit with significant disadvantages and inaccuracies [17] especially for patients under general anesthesia. Czonsnka and Pickard [19] reported misleading ICP for instant fluid column measurements and suggested that such pressures should be averaged over at least 30 minutes or more preferably overnight.

Intraparenchymal sensing is likely the most contemporary prevalent method of overall ICP sensing [18]. Hawthorne described it as being the preferred technique of many centers even over intraventricular measurement [49]. Being indirect, the method utilizes a solid-state pressure sensor (e.g. fiber optic or microstrain) placed through a burr hole into the brain's white matter within the non-dominant frontal hemisphere. Wiegand describes intraparenchymal sensors as being the most reliable instrumentation available, easy to place, and with few infections (1 – 2%). The same was supported by Luerssen [50]. He describes their use in Oxford, where surgeons have placed 583 devices, as of the time of publication, in which they (re)zero the devices daily to atmospheric pressure. He indicated the intraparenchymal microstrain sensor (i.e. the Codman MicroSensor) was the device of choice in both emergency and elective cases at Oxford. Several studies have shown microstrain parenchymal sensing to be as accurate as intraventricular measurement [5, 77].

Other indirect invasive approaches exist, as illustrated in Figure 6. Measurements by epidural, subdural, or subarachnoidal access provide pressures which may be associated with ICP. Subdural and subarachnoid measurements are quite rare in modern clinical approaches [17]. They require the use of bolts for anchoring to the skull with an open saline-filled lumen, placed just under the dura, connected to a transducer. Weigand indicates they are less prone to infection than direct measurements (e.g. ventriculostomy), but may be compromised upon brain swelling blocking the lumen. Roboel cited concerns for

intercompartmental pressure gradients and focal ICP elevations as a reason to choose intraparenchymal or intraventricular measurements instead [48].

With respect to epidural measurements for assessing ICP, pressure may be measured in between the skull and dura with a sensor facing the brain. Zhang described the benefits of such measurement as a lower probability for infection, hemorrhages, and seizures compared to direct methods [18]. Further, in the case of an epidural measurement, the dura may be left uncompromised, avoiding the risk of a CSF leak. However, there are concerns with the dura diminishing true ICP translation and overall the method's accuracy has been deemed not support routine clinical use by some clinicians [17, 18].

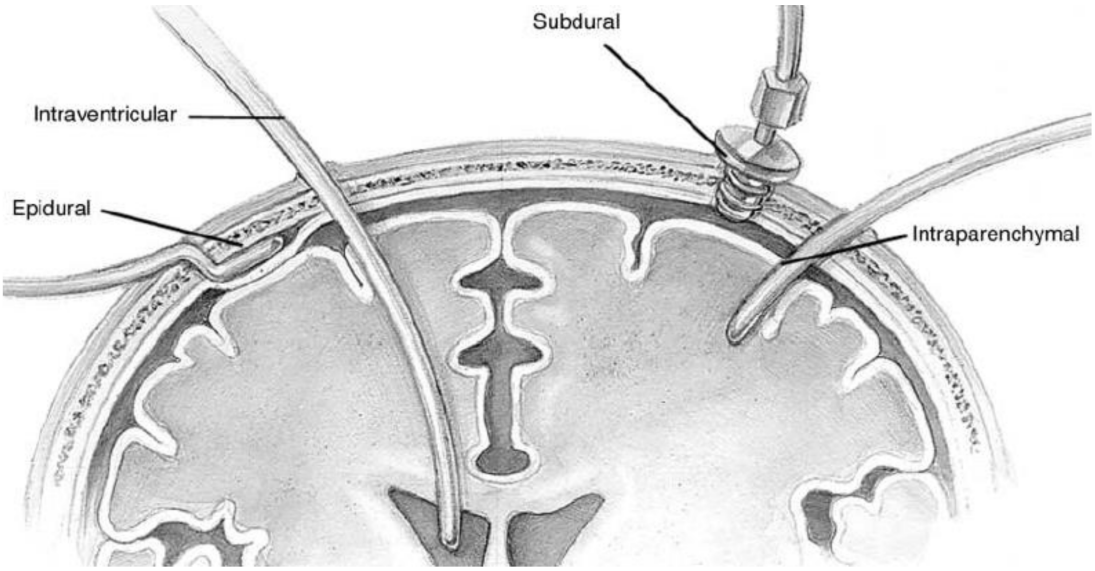


Figure 6 - Illustration of various ICP measurement techniques.

(Source: Harary, Dolmans, & Gormley)

Non-Invasive ICP Assessment

All non-invasive approaches to ICP assessment are indirect, meaning they use physiologically related measurements that may be correlated, or proportional to actual ICP. Sonography techniques allow for one such non-invasive assessment by measuring a patient's optic nerve sheath diameter. The optic nerve sheath is an extension of the dura mater, which is the tough outermost membrane enveloping the brain and spinal cord. The perioptic nerve's fluid is generally in communication with CSF, hence providing an avenue for ICP evaluation [78].

Studies [79] have shown that the nerve diameter, as assessed by transorbital sonography in the transverse plane, 3 mm posterior to the papilla, is linearly related to ICP and can be indicative of hypertension. For patients under normal CSF pressures, the optic nerve sheath was found to have a mean diameter of 3 mm. However, for those patients of increased ICP, the optic nerve sheath diameter was found to average 5 to 6 mm. While this non-invasive technique offers a quick and inexpensive method of qualitatively indicating elevated ICP, the deployment and efficacy of the method may require expert interpretation [17].

Of recent development, and sparsely reviewed in the literature, is the potential for non-invasive ICP assessment by ultrasound measurement of the ophthalmic artery (OA). The OA stems from the internal carotid artery within the cranium, transporting blood along the optic nerve to the orbit. The OA is subject to ICP within the cranium, but not in the orbit where pressure is equal to atmospheric.

The diameter of the OA inside the cranium is smaller than within the eye due to ICP. Consequently, blood flow velocity is higher intracranially than within the orbit. Vittamed, founded in 2013 and associated with U.S. based Boston Neurosciences, is currently developing instrumentation for measuring the OA blood flow velocity within the cranium and within the orbit using a dual-depth high-resolution transcranial Doppler insonation [80]. The approach necessitates extracranial orbit compression to equate blood flow velocities in both locations. The equilibrium pressure is then interpreted as ICP. Ragauskas reported results from a study of 62 patients where simultaneous recordings of OA based non-invasive ICP measurements were compared to direct measured ventricular pressure [81]. Results showed low systemic error of 1.6 mm H_2O with a precision of 30 mm H_2O. The authors suggested the OA method did not need calibration. However, in a 2016 review by Robba et. al. the clinical practicality of the new method was questioned due to the uncertainty in locating the intracranial and extracranial segments of the ophthalmic artery [20]. Robba suggested that even if clinicians were to overcome doubts of being able to find the ophthalmic artery, then the technique would require highly skilled transcranial Doppler specialist with fine anatomical knowledge.

Other non-invasive approaches to ICP have been proposed and researched within the literature. For instance, the delay of visually evoked N2 electrical potentials, as measured upon a patient's scalp, have been correlated to rises in ICP [82]. The challenge, however, is with the practicality of the clinical setup for

the measurement and interpretation of the delays, which may require neurophysiological expertise. Neonatal fontanelle compression is yet another ultrasound method whereby an infant's "soft spot" is compressed during Doppler sonography to examine the hemodynamic response. While qualitative in nature, the technique provides a method of assessing progressive or persistent elevations in ICP for neonates with hydrocephalus. Several literature reviews have categorized numerous non-invasive approaches into five categories consisting of fluid dynamics, ophthalmic, otic, electrophysiologic, and miscellaneous [18, 78]. Table 1 outlines the various techniques which have been researched and reviewed throughout the literature.

Overall, with respect to the most current non-invasive approaches to ICP, all authors reviewed concluded that ventricular catherization remains the gold standard. Furthermore, there was consensus that non-invasive ICP assessments were presently only qualitative and insufficiently accurate enough for routine clinical use to provide an alternative to invasive approaches [17, 18, 20, 48]. Nonetheless, Wiegand attributed non-invasive assessments as clinical signs, complimentary to diagnosis, such as clinical history, physical examination, and radiological methods for the assessment of elevated ICP. Altogether, non-invasive solutions are desperately needed and therefore continue to be the topic of much research.

Table 1 – Non-Invasive ICP Approaches

Non-Invasive ICP Method Category	Measurement Technique
Fluid Dynamics	Magnetic resonance imaging (MRI); transcranial doppler ultrasonography (TCD); cerebral blood flow velocity (CBFV); near-infrared spectroscopy (NIRS); transcranial time-of-flight;
Ophthalmic	Spontaneous venous pulsations (SVPs); venous ophthalmodynamometry (ODM); optical coherence tomography (OCT) of retina; optic nerve sheath diameter (ONSD); pupillometry;
Otic	Tympanic membrane displacement (TMD); otoacoustic emissions (OAE)/acoustic measure analysis; transcranial acoustic (TCA) signals;
Electrophysiologic	Visual-evoked potentials (VEP); electroencephalogram (EEG);
Miscellaneous	Skull vibrations; brain tissue resonance; jugular vein analysis;

ICP Telemetric Approaches

Transcutaneous communication with human implantable devices have been reported in the art comprising optical, inductive, or high frequency radio techniques as reviewed by Townsend [83]. An ICP transponder concept essentially encompasses wireless communications, and optionally power, to an implantable self-contained pressure sensor, which for ICP, could be deployed for either direct or indirect measurement. It was first proposed by R. Stuart MacKay in 1965 with initial prototypes developed by Atkinson et. al. in 1967 for one of the most troublesome diseases, hydrocephalus [84, 85]. Atkinson developed an entirely passive transponder, shown in Figure 7, consisting of an inductor and capacitive based absolute pressure sensor (i.e. LC tank circuit) that operated around 70 MHz.

The transponder's frequency would vary with ventricular pressure as one side of the capacitor consisted of a stainless-steel diaphragm 8mm in diameter. The Atkinson device was implanted in a 2-month-old infant. They described hesitation about deploying the sensor in either the epidural or subdural space as ICP may be dampened by scar tissue. Rather, they coupled the sensor to a ventricular catheter. The results were successful in that they detected changes in ventricular pressure, including variations with the patient's respiration, but not arterial pressure pulses. The system was reported to have 5 mm H_2O of telemetric noise. Atkinson reported of several problems including drift arising from stray capacitance, which reduced the sensitivity of the device, thought to be

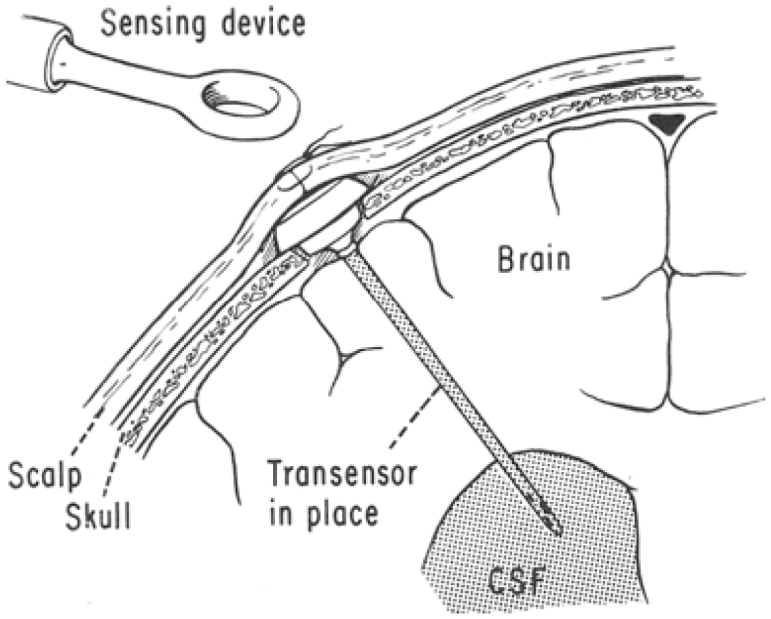


Figure 7 – Transponder described by Atkinson et. al. [84]

from water absorption. Furthermore, the absolute pressure sensor was subject to atmospheric pressure changes in which the authors described the “transensor” as an aneroid barometer or altimeter. They additionally cited diaphragm materials as presenting an issue. Nevertheless, development, testing, implantation, and operation of the device was a landmark for telemetric ICP sensing.

Differential pressure sensors were deployed during the 1970’s as an improved attempt to circumvent atmospheric pressure changes [86]. Cosman developed a differential sensor for measuring subdural pressure, which would potentially negate atmospheric pressure changes. The sensor was designed to provide accurate ICP by comparing to an external pressure palpated to the scalp above the sensor [87]. The transponder communicated by radio telemetry, similar to Atkinson, being based on an LC tank circuit. Cosman’s approach would simultaneously detect the zero-point of the sensor corresponding to a balance of pressures across it (i.e. ICP – pressure by palpation). This device was commercialized despite its 24% failure rate within the first week of implantation [44].

In 1988 a ten-year follow-up on the performance of an epidural telemetric sensor was reported by Gucer et. al [88]. Similar to prior work, it was also an LC tank circuit whereby a capacitor was the pressure sensitive element. The device was implanted into 127 patients. 13 of the patients retained the sensor for between 4 to 9 years. Gucer and team evaluated the sensor for accuracy, longevity, safety,

and stability. The sensor was found safe and enduring without even one infection. Sensitivity was sufficient enough to pick up ICP waveforms. However, drift was drastically unacceptable at 1.0 ±0.2 mm H_2O per day. The drift was responsible for patients telemetrically measuring 2,290 mm H_2O, when they actually had normal ICP. Biofluid intrusion was also an issue due to the packaging and diagraph fatigue.

Despite numerous efforts throughout the past fifty years, no telemetric biopressure sensor device has attained the commercial success like that of the CardioMEMS for arterial blood pressure. The transponder is altogether similar to that proposed by Atkinson, Cosman, and Gucer. It is a battery-less device, excited by ex-vivo radio frequency (RF) energy in which the transponder responds with a resonant frequency based on an LC tank circuit. Pressure is proportional to its capacitive sensor in parallel with an inductor. The device is entirely encapsulated in glass, minimizing frequently reported drift mechanisms associated with biofluid intrusion in capacitive sensors [89]. Power transfer for the device likely lies around 300 μW with DeHennis and Wise reporting inductive power consumption for a similar device at 340 μW and Brancato the same at 300 μW [90, 91]. The sensor is intended for at least a 3-year implant life, but drift data has not been made public or published, except for qualitative reports indicating it is low and acceptable for arterial pressure use [89]. However, such pressure ranges are approximately an order of magnitude larger than that necessary for ICP measurement.

Raumedic Neurovent-P-tel

Modern developments in implantable telemetric ICP sensors include two recently commercialized European models: the Raumedic NEUROVENT-P-tel and the Miethke Sensor Reservoir [92, 93]. Both models are reportedly based on microstrain transducers. The Raumedic device, shown in Figure 8, is a stand-alone remote intraparenchymal sensor, completely passive, with first clinical use in 2010. The device is currently approved in Europe for use up to 90-days. It consists of three main system components: the transponder, the ex-vivo active antenna unit, and the storage monitor. Pressure measurements can be taken at frequencies of 1 or 5 Hertz. Specifications indicate an operable pressure range of -20 to +400 mm Hg with an atmospheric limit of 1,500 mm Hg. Accuracy is specified at ±2 mm Hg with a sensitivity of 1 mm Hg [38].

Antes, et. al. with the Saarland University Medical Center in Homburg, Germany, reported use with the Neurovent P-tel device in 247 patients [37]. He describes the device as having a 3 cm long polyurethane sensor catheter with a diameter of 1.67 mm for intraparenchymal placement, which Welschehold indicates is silicone coated. Further he details that the sensor housing is made of ceramic at a diameter of 3.15 cm and a height of 4.3 mm. The P-tel device is inductively powered and provides data transfer via load modulation.

Out of 247 patients, only seven technical problems occurred with one being due to trauma. The P-tel had a mean time of implantation of 46.9 days with a range between 3 and 90 days. Antes reported the system was very easy to use and

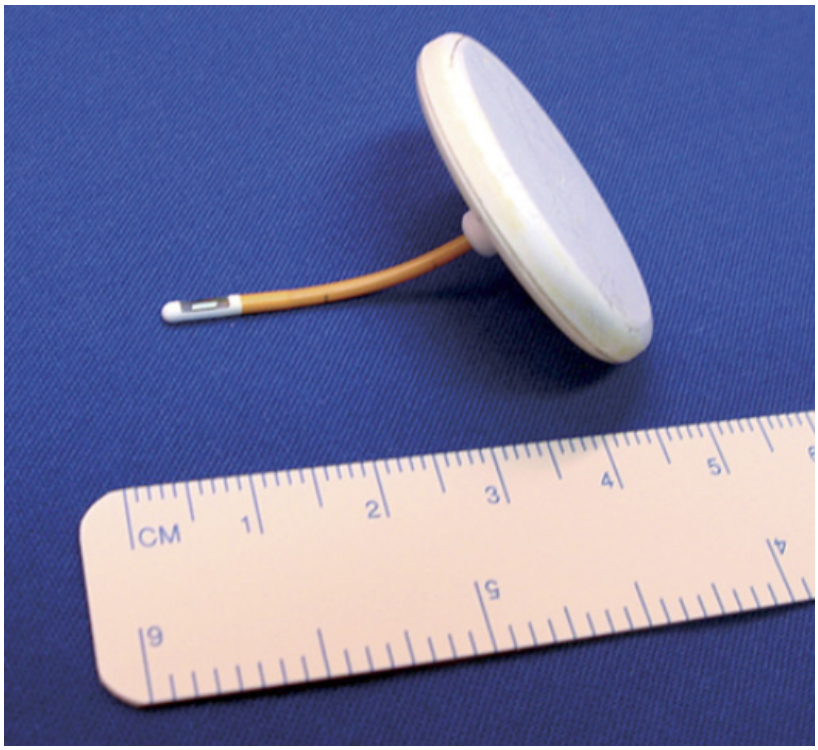


Figure 8 - Raumedic NEUROVENT-P-tel [38]

(Source: Welschehold, Schmalhausen, et. al.)

staff could be instructed within only a few minutes for operation. Disadvantages were noted related to incorrect alarm settings or insufficient fixation of the sensitive antenna, interrupting ongoing measurements, sometimes for days. He also described that the readout module's software was a weak point, lacking the ability to provide simple mathematical or statistical measurements (e.g. min, max, average, etc.).

Antes cited a negligible zero-drift of about ±2.5 mm Hg but neglected to describe the interval or whether the zero-drift was measured or taken from a specification. Stehlin cited Raumedic as specifying a drift of ±2 mm Hg per year with the ability of the Neurovent-P-tel to provide reliable pressure data up to 18 months in-vivo, albeit regulatory limited to 90 days [44]. However, Welschehold et. al. in first use of the device cited a drift of ±2 mm Hg per 29 days [38]. Reports for Raumedic's similar microstrain tethered monitor has measured a drift of 0.6 mm Hg after five days implantation into the parenchyma [49] and would more closely coincide with that reported by Welschehold. Lastly, Antes described that a major shortcoming of the device was the limited 90-day implant period whereby a second surgical procedure was required to remove the probe. He indicated the second surgical operation often deterred many potential candidates.

Meithke Sensor Reservoir

In 2015, Meithke similarly introduced a telemetric ICP sensor, shown in Figure 9, which integrates into a shunt's Rickham reservoir, named Sensor Reservoir. Unlike the Raumedic counterpart, the Miethke device communicates directly with

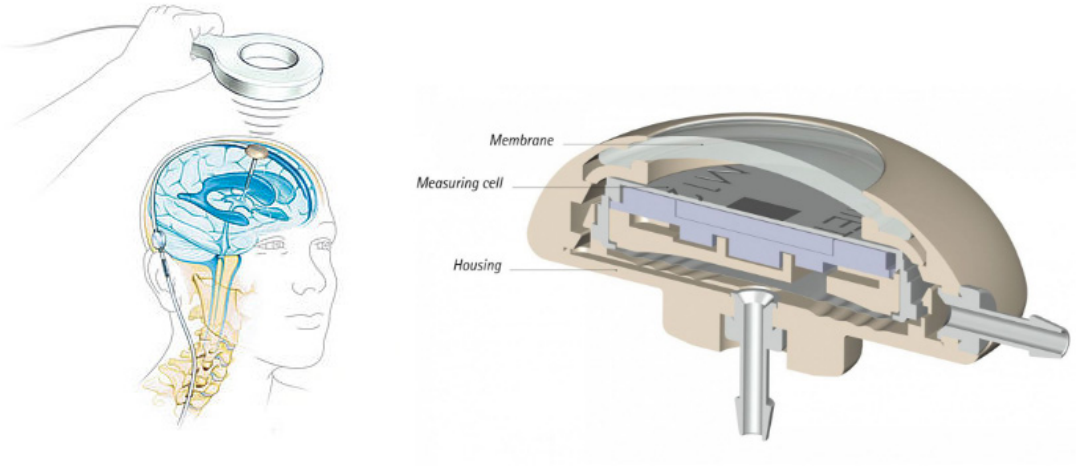


Figure 9 - The Miethke SENSOR RESERVOIR

(Source: Christoph Miethke GmbH & Co. KG)

CSF from the ventricle. It consists of three main system components: the passive sensor implant, an ex-vivo active antenna/exciter unit, and a tethered handheld reader/display unit which can store pressure data on an SD card. The manufacturer claims, that for the first time ever, the system is capable of assessing shunt function. Miethke describes uses of the sensor encompassing non-invasive ICP detection, localization, and evaluation of occlusion in a shunt as well as shunt mechanical malfunctions [94]. The sensor measures 23.8 mm in diameter and 7.6 mm in height.

Again, a team of neurosurgeons at the Saarland University Medical Center evaluated the implantable sensor in 25 patients over the course of a year. Antes describes the sensor being housed in a polyether ether ketone housing with a silicone dome, similar to a shunt reservoir [42]. However, he states that unlike a conventional reservoir, the device also contains a titanium-covered measuring cell for noninvasive transcutaneous ICP measurement. True to its name, the device can function as a reservoir and be tapped percutaneously for drug delivery or CSF withdrawal. Contrary to other reports citing microstrain sensing, including the latest publication in 2018 from Harary, Antes reports that the sensor unit contains an application specific integrated circuit (ASIC) with 64 capacitive sensors [43]. CSF envelops the measuring cell and pressure is directly transmitted directly through the housing via a 12.0 μm titanium plate. ICP values can be read out at a rate of 44 samples per second (i.e. Hertz). Antes indicates

the implantation period of the Sensor Reservoir is unlimited and explanation is unnecessary with respect to regulations.

Antes and team selectively deployed the Sensor Reservoir into 25 patients between December 2015 and November 2016 who were suffering from headaches. They categorized measurements as normal ICP, underdrainage, over-drainage, and imbalanced CSF drainage. A total of 183 telemetric measurements were taken during the period, which resulted in 85 valve adjustments. Antes reported that obtaining ICP measurements was quick. Such measurements and adjustments were reported to have positive clinical improvements in 18 of the 25 patients. Interestingly, Antes reported that contrary to expectations, ICP was not well correlated with shunt valve settings. Antes indicated this may be due to two possible reasons: 1.) short-term measurements may not represent average ICP, and 2.) valve setups utilizing both a differential pressure valve and a gravitational valve in series may influence drainage to an incalculable degree.

Shortcomings of the device were reported as the thickness at 8 mm, especially for patients with thin skin. Antes also described the desire to take continuous measurements over a one- to two-day periods to detect certain pressure leaks, pulse pressure, and pathological slow waves. He further cited that the ex-vivo antenna was too large and heavy to facilitate fixation to a patient's head. Out of 25 patients, two devices provided improbable ICP measurements. One patient presented with slit ventricles and no sufficient ICP pulse signal was detected,

with ICP very negative. The other patient's device, placed into dilated ventricles, showed disproportionately high ICP values soon after insertion. No comparisons to true ICP, measured by ventriculostomy, were presented. As such, there was no report on measurement drift, but Antes did state he did not believe the device could remain accurate beyond five years.

Research Gap and Limitations

As described in the Challenges of Intracranial Pressure Monitoring section, pressure sensor accuracy, especially in terms of drift, remains an unsolved and prominent issue. As a result, standard clinical practice necessitates the use of bedside tethered equipment which must be frequently recalibrated. Infection rates associated with tethered ICP monitors range up to 10% for gold standard ventriculostomy measurements. Avenues for eliminating tethered devices, and thereby reducing infection rates which increase over time, are restricted due to drift over the long-term (i.e. << months). Clearly shown within the same Challenges section is the immense need, however, for such telemetric pressure sensing devices.

Yu, in his review of the challenges and state of the field for chronically implantable pressure sensors, stated that sensors must possess a stable and consistent response over their lifetime [46] to be effective, of course. However, to date, the state of technology for biopressure sensing has not achieved such a response to enable the very low-pressure measurements of ICP over a several

year lifetime of implantation. Yu cited material aging and mechanical fatigue as primary contributors to both baseline (i.e. zero-drift or offset drift) and sensitivity (i.e. gain) shifts.

Drift mechanisms have been researched and reported throughout the various sensors developed and cited herein encompassing atmospheric pressure or altitude changes, electrolytic biofluid intrusion, temperature changes, gas leaks, static discharge effects, among others beyond those described by Yu. Efforts to mitigate these effects include Cosman's work in the 1970s utilizing differential pressure sensors, including the application of a known external pressure to calibrate the subcutaneous sensor. Additionally, development by Spiegelberg of their tethered monitor employing an air chamber transducer facilitates recalibration of external pressure sensors without removal of a catheter/transducer. However, research and development to date has not revealed any methods to mitigate drift to a clinically acceptable level, either by reduction or calibration, to enable long-term implantation of a telemetric ICP biopressure transponder. Both drift reduction and non-invasive in-vivo calibration for clinically acceptable ICP measurement is the pursuit of this research.

CHAPTER THREE

MATERIALS AND METHODS

Overview

This research investigates the current limiting factors preventing long-term implantable ICP measurement. Recognizing drift as the primary inhibitor, this work endeavors to minimize inherent pressure sensor drift and to mitigate both offset and gain shifts via a novel in-vivo calibration system. Achieving such an advancement could possibly facilitate the world's first ever accurate long-term (i.e. >>1 year) implantable ICP monitor. Such a sensor system with this capability would allow for post-implant non-invasive ICP monitoring to provide early warning or confirmation of dangerously elevated ICP levels. Furthermore, the capability to accurately measure ICP long-term would facilitate optimization of hydrocephalus shunt valves or even automated closed-loop systems.

A review of the literature, assessing prior clinical research, was reported within the Literature Review for assessing the physiological approaches and variables of ICP measurement. Additionally, a survey of sensing technology for ICP measurement was conducted and reported. Within this chapter, requirements and research objectives are established for building upon prior research for enabling long-term ICP sensing. Design considerations for a new novel biosensor are described in the following sections of the Approach. Finally, methods for simulation and laboratory verification of a new novel prototype

sensor are outlined.

Methods undertaken by this work include:

1. A review of prior clinical research assessing the physiological approaches and variables to ICP measurement.
2. A survey of sensing technology, including shortcomings or sufficiency for ICP measurement.
3. Establishment of requirements and research objectives for a long-term ICP biosensor.
4. Design of a novel custom sensing device and methodology for calibrated ICP measurement.
5. Simulation of key design characteristics and uncertainties.
6. Laboratory evaluation of selected sensing die technology for potential application in ICP sensing.
7. Development of a prototype sensor with laboratory verification of key performance metrics.

Requirements

General requirements for the sensor include the use of biocompatible material interfaces, geometrically acceptable for implantation. The sensor must further support non-invasive readout and ultimately provide clinically acceptable resolution and accuracy. Overall, the biopressure sensor transponder (i.e. the entire sensing and telecommunicating implant) should provide reliable long-term operation, durability and, preferably, battery-less operation. The sensor may

preferably utilize transcutaneous energy to eliminate the need for a transponder battery, which may present hazardous toxic materials, or necessitate replacement via revision surgery. The focus of this work is upon minimizing or mitigating sensor drift. Specific requirements for the sensor follow within this section.

The Association for Advancement of Medical Instrumentation (AAMI) provides a standard for intracranial pressure monitoring devices, with its latest revision in 2015 [95]. The scope of the standard encompasses percutaneous fluid and electrically coupled sensing devices, common in today's neuro-ICU wards, patient interfaces including sensor contact and display devices, and fully implantable type devices. Its purpose is to provide labeling, safety, performance requirements, and test methods for assuring the safety and effectiveness of ICP monitoring devices. The standard indicates its concepts are to be considered flexible and dynamic as advances are made in ICP monitoring technology. Relevant to the scope of this work, intended for initial research, development, and evaluation, the standard's recommendation for pressure range, accuracy, and zero-drift will be considered.

As previously revealed in a survey of the literature, Kimelberg and Ravi showed normal ICP to range from 0 to 136 mm H_2O in the supine position, which can also become negative in the upright position according to Sotelo. For shunted patients, negative pressures up to -440 mm H_2O have been described due to siphoning effects, which can result in CSF over drainage [96]. Koskinen showed

pathological ICP to average 249 mm H_2O with Lundberg showing extreme ICP's of 500 mm H_2O and beyond, particularly for head trauma patients. The AAMI standard requires monitoring of 0 to 1,400 mm H_2O. However, given the standard's broad scope and rationale, which includes bedside critical care acute monitoring for the critically ill, the upper end range of 1,400 mm H_2O may be excessive for long-term monitoring of hydrocephalus patients. Such long-term monitoring, as sought herein, is intended to provide ongoing ICP measurements to verify shunt functioning, optimization, and early warning levels prior to acute levels of intracranial hypertension. As reported by Lundberg, pressures beyond 500 mm H_2O are considered severe. Young's research additionally showed that levels of 1,000 mm H_2O or greater typically resulted in brain herniation and death within 24 hours. While pressure monitoring of levels beyond 1,000 mm H_2O would be desirably broad, such levels are associated with head trauma which necessitate acute care intervention and pressure monitoring. Unnecessarily increasing the pressure sensing range for a long-term implantable monitor would reduce sensitivity and accuracy due to the pressure diaphragm's configuration. Instead, given the variety of everyday patient positions, versus an acute care setting, it is important for long-term monitoring to allow for negative pressures range rather than an extended positive pressure only (i.e. 0 to 1,400). Therefore, for this work, a pressure range of -500 mm H_2O to +500 mm H_2O will be adopted.

Insight into clinically acceptable sensor resolution can be gained by examining hydrocephalus shunt valve resolutions. Lollis et. al. performed a review of the

most prevalent programmable hydrocephalus valves on the market in 2010 consisting of the Codman® Hakim® Programmable valve, the Medtronic® Strata® valve, and the Sophysa® Polaris® SPV valve [97]. The authors additionally reported on the Aesculap® ProGAV®. However, this is an anti-siphon auxiliary valve used only in-line with a primary valve. Out of all the valves Lollis reviewed, the Hakim Programmable valve had the best resolution of 10 mm H_2O. Upon further examining manufacturers' present offerings, as of the time of writing, no valve currently marketed provided a higher setting resolution than the Hakim Programmable valve. Medtronic's valves provide a range of pressure-flow characteristics in which the Delta programmable valve's Instructions for Use (IFU) indicates a setting tolerance range of ±40 mm H_2O [98]. Maximum pressure range encompassing all the primary valves examined by Lollis was 200 mm H_2O, consistent with normal pressure levels reported by Drake and Sotelo. Therefore, given the highest resolution valve in clinical use resolves to 10 mm H_2O, as of the time of writing, and given this would represent 1% of the sensor's overall span (i.e. ±500 mm H_2O), 10 mm H_2O will be selected as the minimum clinically acceptable resolution for the pressure sensor system researched herein.

In assessing the accuracy necessary for the sensor, it has been shown that adjustment of a valve's setting by only 20 mm H_2O or less can have clinical impact upon pediatric patients [99]. Therefore, to not introduce uncertainty beyond half this range, an accuracy of ±5 mm H_2O will be set as an objective for

the system. Likewise, the sensor's precision objective will be targeted for ±5 mm H_2O so as to not cumulatively extend beyond the 20 mm H_2O range for clinical effect. Combined, the sensor's accuracy and precision objectives of ±5 mm H_2O each results in a total possible error of ±10 mm H_2O, or a 20 mm H_2O range, which will be adopted over the span found by Lollis of 200 mm H_2O. This is within the AAMI standard's requirement of ±20 mm H_2O (40 mm H_2O range) over a 0 to 200 mm H_2O range. Thereafter, the standard calls for ±10% maximum error and will be adopted for this scope of work as well.

With respect to the sensor's pressure drift, service life of the implantable sensor comes into question. Prospective studies have shown the failure rate of CSF shunts is approximately 50% by year two and between 70% to 88% by year ten [31, 32, 33, 34]. Therefore, to serve the majority of patients with a diagnostic device complementing shunt treatment for both shunt optimization and as a diagnostic for shunt failure, the sensor will be planned for an expected 10-year service life. The sensor serves two functions: First, pressure monitoring for valve setting optimization, maintenance, and research; Secondly, as a non-invasive indicator of shunt failure to distinguish alarming ICP values (e.g. >200 mm H_2O) prior to escalating and dangerous ICP levels. To distinguish alarming ICP, the sensor error should be less than ±50 mm H_2O such that a measurement of 250 mm H_2O, for example, would confidently signal clinical intervention without potentially posing a false alarm (i.e. 200 mm H_2O or less where a valve's setpoint may be set). At the same time, a 250 mm H_2O measurement would not

erroneously allow drift error in excess of 300 mm H_2O true pressure, well within the range of clinical intervention and management. Therefore, over a 10-year service life, the sensor must not encounter drift, on average, of more than 5 mm H_2O per year incrementally and successively over the service period (i.e. +50 mm H_2O or -50 mm H_2O), which cannot otherwise be corrected by sensor calibration. This performance metric will be considered separate from the sensor system's accuracy at time of manufacture. Drift specifications with the AAMI standard relate specifically to zero, or offset drift, and testing occurs over a minimum of 10-days at 0 mm H_2O. There is no specification within the standard related to drift other than the accuracy cited.

Table 2 outlines the key requirements and research objectives developed as goals for this work. The objectives are aimed at satisfying the key requirements, in part, as related to the scope of the sensor research herein. Each objective is keyed and will be cited within Chapter Four's Results and Discussion.

Approach

Sensor Technology

Based on the literature review, among the various techniques and methods of measuring ICP, there are two dominant transduction means that have clinically demonstrated sufficient sensitivity for measuring the very low pressures of CSF. Both methods are based upon diaphragm translation, including microstrain sensing and fiber optic interferometry. Results from Koskinen and Olivecrona

Table 2 – Key Requirements and Research Objectives Summary

Top Level Requirements		Key Requirements for Sensor Element(s)		Research Objectives	
R1.0	The sensor must provide biocompatible interfaces.	R1.1	The sensor must present a biocompatible silicon pressure diaphragm and may optionally include a long-term compatible parylene coated membrane or silicone gel coupling for pressure transduction. Any other direct contacting materials, such as sealants and adjoining enclosure, must be biocompatible.	O1.1	Justification of sensor to present a bottom-side bulk micromachined monocrystalline die surface for the pressure diaphragm to meet biocompatibility. Die must be capable of bonding to suitably hermetic biocompatible materials. Sensor must withstand sterilization method(s).
		R1.2	Surfaces must be capable of being cleaned and undergo sterilization.	O1.2	Device must be capable of sustaining a compatible wash and autoclaving, ethylene oxide, or gamma radiation sterilization without damage.
			→	O1.3	Surfaces must be capable of hermeticity to meet the intended service life of the implant.

Table 2 (continued)

Top Level Requirements		Key Requirements for Sensor Element(s)		Research Objectives	
R2.0	The overall sensor transponder must be geometrically acceptable for implantation.		→	O2.1	The sensor's transponder components must be capable of being contained within a typical CSF reservoir's volume (34 mm diameter and 7.2mm height) for suitable implantation below the scalp, yet above the skull, with pressure communication through a cranial burr hole.
R3.0	The sensor must provide clinically acceptable ICP resolution and accuracy.		→	O3.1	Sensor must provide a pressure range from -500 mm H_2O to +500 mm H_2O.
			→	O3.2	Sensor must provide a 10 mm H_2O resolution, or less, up to 200 mm H_2O and within a 10% maximum beyond.
			→	O3.3	Sensor must provide a maximum accuracy (or trueness) of ±5 mm H_2O.
			→	O3.4	Sensor must provide a maximum precision of ±5 mm H_2O.

Table 2 (continued)

Top Level Requirements		Key Requirements for Sensor Element(s)		Research Objectives	
			→	O3.5	The sensor must overall provide a combined maximum accuracy (incl. precision) of ±10 mm H_2O.over a ±200 mm H_2O range and 10% maximum beyond.
R4.0	The sensing mechanism must support non-invasive readout.	R4.1	The sensor and/or supporting electronics must provide a compatible electrical signal for non-invasive transcutaneous transmission.	O4.1	Buffered sensor output must be capable of providing a signal within a 0 - 3.3 volt range for interfacing to the Texas Instruments CC2541 ADC and Bluetooth LE system-on-chip.
		R4.2	The sensor and associated transponder electronics must not exceed a power consumption limit necessary to operate over a ten-year service life or that exceeds a safe level for transcutaneous powering.	O4.2	The estimated power consumption of the sensor's transponder must be less than that which can be transcutaneously transmitted safely per IEEE Standard for Safety Levels with Respect to Human Exposure to Radio Frequency Electromagnetic Fields, C95.1.

Table 2 (continued)

Top Level Requirements		Key Requirements for Sensor Element(s)		Research Objectives	
		R4.3	The sensor must be capable of non-invasive post-implant calibration (or otherwise maintain acceptable accuracy and precision as specified).	O4.3	The sensor must be capable of gain and offset calibration to meet the specified accuracy.
R5.0	The sensor must support a ten-year service life.	R5.1	Drift performance must be sufficient for indicating shunt failure or for distinguishing dangerous ICP values.	O5.1	Expected drift over the device's intended service life must be less than ±50 mm H_2O.

demonstrated that ICP microstrain sensing resulted in the lowest drift measurements over time and temperature, notwithstanding the manometer, compared to fiber optic and capacitive means. Distal fiber optic transduction lacks temperature compensation methods, and when calibrated ex-vivo without temperature-based zeroing, the technique easily results in thermally related pressure shifts in-vivo. Capacitive based sensors for low pressure liquid media sensing have shown low sensitivity, such as that by George et. al. Sensitivity levels have been reported to demonstrate atto-farads per mm H_2O, which necessitates on-chip processing electronics to minimize parasitic capacitance. Further, the literature reports capacitive based sensing is subject to drift resulting from biomatter adsorption onto the sensor's plates and non-condensing moisture intrusion [72, 88, 100]. Microstrain sensing, however, has a proven history of acceptable clinical use for ICP, short of long-term drift, providing a proven biocompatible interface for CSF and brain tissue. Barlian et al. found that piezoresistive sensing provided distinct advantages over capacitive sensing including ease of differential configurations and freedom from film stress related errors and surface micromachining yield challenges [101]. In consideration toward accomplishing the goal of this work, microstrain sensing will be chosen as a potential solution.

Metallic Strain Sensing

Microstrain pressure sensors are based upon measuring the strain incurred by the deflection of a pressure diaphragm. The shape of the diaphragm is arbitrary,

but usually takes the form of a circle or square. Metal diaphragms were originally employed, continuing into the 1970's, with strain gauges bonded thereupon by epoxies, phenolics, or eutectics [102]. Popular to early applications, and prior to piezoresistive sensors, strain was quantified by measuring the conductivity of a resistive metallic foil pattern joined to the diaphragm substrate. Figure 10 illustrates an example resistive pattern in which two electrical terminals are provided to the left of the figure, which are connected to an interwoven conductive design. The resistivity of the segments is given by Ohm's law:

$$R = \rho \frac{l}{A}$$

where ρ is the specific electrical resistance of the metal, l is the length, and A is the conductor's cross-sectional area. When lateral forces (i.e. horizontal to the page) extend the design, the interwoven conductive lines become elongated, increasing the length of each resistive segment and correspondingly decreasing the cross-sectional area, which altogether increases resistance. Alternatively, when lateral forces compress the design, the resistive lines broaden and shorten, thereby decreasing resistance [103]. The serpentine layout serves to increase the gain of the sensor since stress applied to the sensor not only affects one resistive segment, but multiple parallel segments in series over a relatively small sensing area.

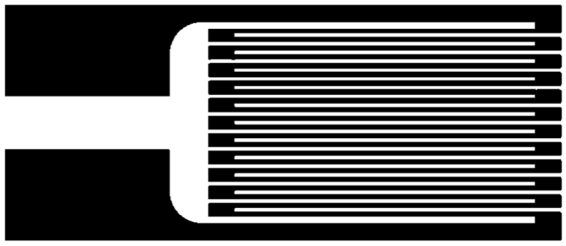


Figure 10 – Conventional metallic micro-strain resistive pattern.

The gauge factor is essentially the gain of the device providing the change in resistance for an applied stress resulting in strain. The gauge factor is defined as:

$$GF = \frac{\frac{\partial \rho}{\rho}}{\varepsilon}$$

where ε is the applied strain to the device.

Piezoresistive Strain Sensing

In 1954, Charles Smith observed and described the piezoresistive effect in silicon and germanium semiconductors, providing a change in resistance upon applied stress [104]. The piezoresistive effect for n-type silicon was thereafter further described by Herring's theory of the many-valley conduction/valence-band model [105].The model explained that crystal lattice strain disperses carriers across several valleys (up to six in silicon aligned with three <100> directions), which perturbs the longitudinal and transverse average mass. Compared to the unstressed lattice, this leads to an isotropic overall *effective mass*, m*. Strain is theorized to alter the energy band curves to effectively change the mass and, hence, the conductivity. Depending upon whether carriers are dispersed to lower or higher conduction states, changes in effective mass will result in either a decrease or increase in resistivity. The mechanism of the p-type piezoresistive effect has largely remained uncertain, until recently, due to the complexity of its valence band structure. However, recent theoretical approaches attribute the effect to a similar mass change from band warping and splitting [101].

The piezoresistive coefficient relates the fractional change in resistance to the applied stress. The coefficients, π, necessitate four subscripts since they relate two second-rank tensors, stress and resistivity. The first subscript refers to the direction of voltage measurement, the second to current flow, and the third and fourth to orthogonal stress components. However, in the most common case, where the direction of current flow and applied stress may be parallel or perpendicular to each other, and oriented in the <100> or <110> crystalline lattice directions, the net change in resistivity may be written as the sum of the parallel and perpendicular effects. As such, a diffused resistor subjected to parallel and perpendicular stress components $\sigma_{\parallel}$ and $\sigma_{\perp}$, respectively, the resistance change is given by:

$$\frac{\Delta R}{R} = \pi_{\parallel}\sigma_{\parallel} + \pi_{\perp}\sigma_{\perp}$$

where $\pi_{\parallel}$ and $\pi_{\perp}$ are the piezoresistive coefficients parallel and perpendicular to the resistor length. It can be shown that the piezoresistive coefficients $\pi_{\parallel}$ and $\pi_{\perp}$ can be derived for any arbitrary crystalline direction from the π_{11} (typical of n-type), π_{12}, or π_{44} (typical of p-type) [101, 106]. The advantage of piezoresistors over conventional metallic strain sensors, other than direct implantation, is that the gauge factor can be 50 – 100 times larger, or more [107, 108]. The magnitude of the piezoresistive effect varies with crystal orientation of the resistor. In order to maximize sensitivity piezoresistors are typically oriented in

the <100> direction for n-type doping and <110> direction for p-type doping [106, 107].

The first commercial devices were introduced in 1958 with early applications primarily targeted toward biomedical and aerospace applications [102]. The development of silicon and germanium piezoresistive strain sensors facilitated pressure sensors with either strain sensors applied upon a sensing diaphragm or within the diaphragm itself. Pressure sensing diaphragms with strain sensing elements applied thereupon suffered from poor stability arising from factors such as thermal mismatch and adhesive creep [102]. Single crystalline diaphragms with diffused piezoresistors quickly disrupted the former market providing superior diaphragm properties negating hysteresis and creep formerly found in metal diaphragms. For thin silicon or germanium diaphragms with small defections, the resistance change is linear with applied pressure, being perfectly elastic at temperatures less than 500°C. Higher volume, lower cost applications thereafter quickly followed.

Pressure Transduction

Pressure transducers utilizing a diaphragm with strain gauges typically employ four strain sensors forming a Wheatstone bridge [109]. The Wheatstone bridge configuration has been shown to be the optimal configuration for minimal detectable pressure signals in a diaphragm [110]. The diaphragm is usually designed such that two strain sensors increase in resistance upon incident

pressure, while the other two sensors decrease in resistance, thereby increasing the gain of the overall transducer.

Figure 11 illustrates an electrical schematic of a pressure transducer's resistive strain sensors arrangement into a Wheatstone bridge. Strain sensors designated by R1 and R3 decrease resistance upon positive incident pressure to the transducer's diaphragm. R2 and R4, however, increase resistance and therefore, in combination with R1 and R3, improve the sensitivity of the transducer. In this configuration, the optimal piezoresistive diaphragm would be one that produces relatively high stress levels in response to incident pressure, a large delta between longitudinal and transverse stress, and relatively small spatial stress gradients over the piezoresistor implant locations [106]. From Figure 11, by letting Vo = +Vo – (-Vo) and a supply voltage of Vs = +V – (-V), it can be formulated from the schematic that:

$$V_o = V_S \left(\frac{R_2}{R_1 + R_2} - \frac{R_3}{R_3 + R_4} \right)$$

The output voltage is zero when the bridge is in balance according to the condition:

$$\frac{R_1}{R_2} = \frac{R_3}{R_4}$$

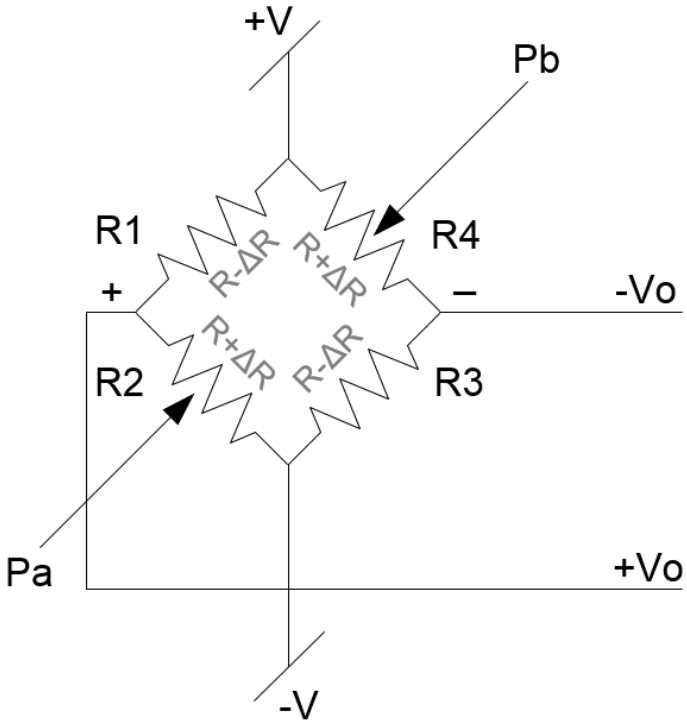


Figure 11 – Wheatstone pressure transducer comprising strain sensors.

A change in resistance for each of the four strain sensors results in:

$$V_o = V_S\left(\frac{R_2 + \Delta R_2}{R_1 + \Delta R_1 + R_2 + \Delta R_2} - \frac{R_3 + \Delta R_3}{R_3 + \Delta R_3 + R_4 + \Delta R_4}\right)$$

If $R_1 = R_2$ and $R_3 = R_4$ then expanding the equation above and substituting provides:

$$V_o = V_S\left(\frac{R_1(\Delta R_3 + \Delta R_4) - R_3(\Delta R_1 + \Delta R_2) + 2R_3\Delta R_1 - 2R_1\Delta R_4}{4R_1R_3 + 2R_1\Delta R_3 + 2R_1\Delta R_4 + 2R_3\Delta R_1 + 2R_3\Delta R_2}\right)$$

By making an assumption that $\Delta R/R << 1$ and that $R_x \bullet \Delta R_y << R_x \bullet R_y$, then the expression above can be shown [111], with corrections, to simplify to:

$$\frac{V_o}{V_S} = \frac{1}{4}\left(\frac{\Delta R_1}{R_1} - \frac{\Delta R_2}{R_2} + \frac{\Delta R_3}{R_3} - \frac{\Delta R_4}{R_4}\right)$$

and by utilizing the gauge factor, GF, the expression further simplifies to:

$$\frac{V_o}{V_S} = \frac{GF}{4}(\varepsilon_1 - \varepsilon_2 + \varepsilon_3 - \varepsilon_4)$$

Therefore, this simplified derivation relies upon two important points: that the two bridge leg resistances are equal, and that R is quite large such that ΔR/R is very small. Furthermore, in order to negate offset and temperature effects, it is preferable that all four bridge resistances be equal [103].

Modern micro-electro-mechanical systems (MEMS) commonly provide monolithic piezoresistive implanted pressure diaphragms fabricated using micromachining etchants. Prevalent pressure sensor types include both *bulk micromachined* monocrystalline silicon as well as *surface micromachined* polysilicon employing thin-film depositions. There are additionally some pressure sensors which are fabricated from bonded metal foil. Monocrystalline silicon material possesses excellent mechanical qualities described by Petersen encompassing high strength, high stiffness, high reliability, high Q, high precision, and with low mechanical hysteresis [112, 113]. Surface micromachined materials, however, do not possess the same high-quality properties. They are usually comprised of polycrystalline or amorphous thin films with existing material stress or unfavorable energies [102]. Nonetheless, the advantage of thin-film deposition lies within the opportunity for CMOS integration using a two-step process first

leveraging mainstream CMOS fabrication with subsequent MEMS specific processing [113]. Contemporary MEMS technologies employ a variety of silicon including bulk silicon (Si), silicon on insulator (SOI), silicon on sapphire (SOS), and silicon carbide (SiC), as well as additional materials such as steel, carbon nanotubes (CNT), and even diamond for critical rugged environments [114]. Common MEMS pressure sensor fabrication techniques encompass isotropic and anisotropic etching, diffused or ion implanted resistors, and various forms of bonding ranging from anodic to direct.

TE Connectivity (previously Measurement Specialties) produces a range of MEMS pressure sensors, formerly offered in bare die, in both absolute and differential configurations. The closest pressure range devices offered by TE Connectivity sought by this work are the 1620 and 1630, which utilizes piezoresistors, providing a -50 to 300 mmHg (-680 to 4,079 mm H_2O) range. Figure 12 shows the 1630 and its cross-sectional diagram.

Sensitivity of the devices are specified at 368 nV/V/mm H_2O. The 1630 device is marketed for use as a biocompatible and temporarily implantable pressure sensor, favorably offering connections on one side of its ceramic substrate. The sensor utilizes film resistors on the printed circuit board (PCB) substrate allowing laser trimmed temperature compensation. Input resistance is specified between 1.2kΩ and 3.2kΩ with output resistance between 270Ω and 330Ω. For liquid media compatibility, a dielectric silicone gel is provided over the topside of the die for fluid isolation. The life of the device is limited to 72 hours. The company also

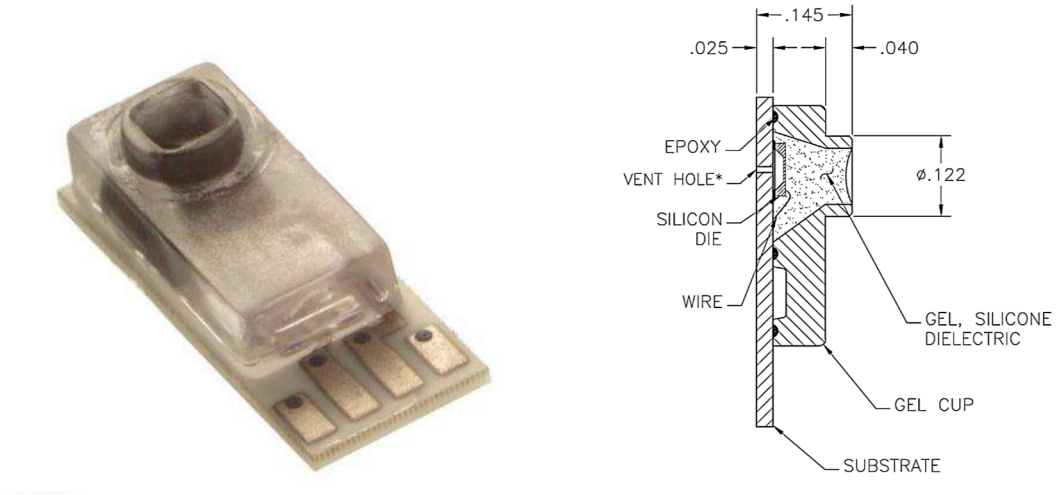


Figure 12 - TE Connectivity 1630

(Source: TE Connectivity)

offers several 0 – 1 PSI sensors. However, TE Connectivity does not offer any matched die configurations, which will later be shown imperative, nor bipolar devices in the desired pressure ranges. The operating pressure range of the 16** series is greater than 8x the desired range of this work's goals, thereby likely diminishing desired resolution.

The Sensor Technology Group of Amphenol produces biocompatible pressure transducers based upon bulk micromachined monocrystalline piezoresistive sensors. The sensors are marketed for low drift performance utilizing what the manufacturer markets as trade secret construction that alleviates long term mechanical creep. Very important to this research, as will be explained hereafter, is that Amphenol produces matched die configurations. Their All Sensors millivolt series, being passive only, allows for customized voltage bias, which is desirable for low voltage operation to reduce quiescent power conditions in the transponder design as well as ease requirements of telemetry power transfer.

Various ranges are offered by Amphenol within the span of several inches of water pressure. The 30 INCH-D-MV operates within the ±30 inches H_2O (i.e. 762 mm H_2O) and has a corresponding full-scale output signal between 19 and 21 mV with 20 mV typical at 12V bias (i.e. 2.19 μV/V/mm H_2O). The sensor module is marketed for use with non-condensing gases, likely due to both top-side and bottom-side die fluid contact. However, for this research, only bottom-side die will be used for liquid media contact. Amphenol specifies the sensor for long

term drift of ±100μV over a one-year time period. Translated over the full-scale range of the device, this figure suggests an expected drift of ±3.8 mm H_2O per year. The device is temperature compensated with laser trimmed resistors and can be parylene coated, offering an additional and optional biocompatible interface with excellent moisture and chemical barrier properties [115]. Specifications indicate the bridge resistance (i.e. input) for its combined dual sensor configuration is 4.5kΩ with an output of 1.5kΩ, which as shown later, results in an average of 1.5kΩ per piezoresistor. Compared to TE Connectivity, this sensor utilizes a higher strain resistance, which improves linearity as shown within the bridge derivation above whereby a $\Delta R/R << 1$ results in the output essentially becoming a product of the strain, ϵ, and gauge factor, GF. Further, when compared with TE Connectivity, the 30 INCH-D-MV provides larger gain at 2.19 μV/V/mm H_2O since the sensor's span is 762 mm H_2O versus the unnecessary large range of the TE Connectivity 1620/30 (4,079 mm H_2O) at 0.368 μV/V/mm H_2O, resulting in a 6x improvement. The 30 INCH-D-MV provides a sufficient proof pressure of 5,080 mm H_2O, which is well beyond physiological ICP pressures or normal atmospheric variations. Burst pressure is specified at greater than 20,000 mm H_2O. Finally, Amphenol is the only manufacturer to specify low pressure long-term drift values in which the values may be acceptable for ICP monitoring if indeed proven with liquid media.Figure 13 shows a microphotograph of one of the 30 INCH-D-MV Amphenol dies. The silicon die is a monocrystalline bulk micromachined pressure sensor utilizing

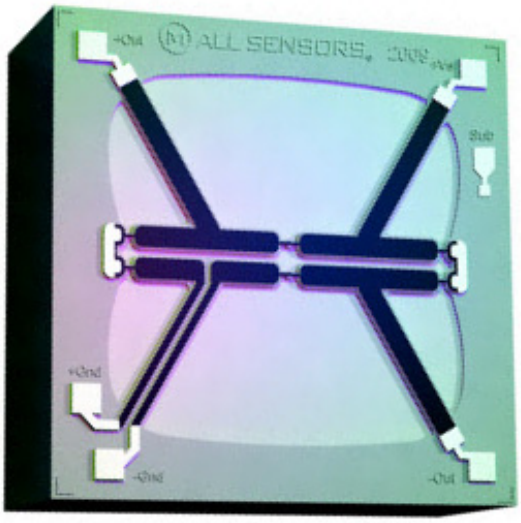


Figure 13 – Amphenol All Sensors 30 INCH-D-MV pressure sensor die, approximately 2 mm^2.

(Source: All Sensors Corporation)

a square diaphragm. The diaphragm is specialized in that it consists of two monocrystalline monolithic layers, being etched top-side and bottom-side to result in a sensitive stress concentrated design. The process is proprietary and partially described in Sensym's U.S. Patent 5,178,016 as a sculptured diaphragm [116].

Piezoresistors are implanted in locations of the thick upper relief shelf, forming a Wheatstone bridge. The custom diaphragm increases bending moment at the location of its shear sensing elements through the load of its thin portion of the diaphragm, which is suspended by the periphery and thicker relief elements. Thinner diaphragms enhance sensitivity whereas thicker diaphragms improve linearity due to lower deflections, consistent with small deflection theory [114]. Unlike other silicon piezoresistive sensors, the Amphenol device does not utilize a surrounding boss structure. Bossed structures increasingly suffer from position sensitivity arising from the acceleration of gravity's influence upon the very sensitive diaphragm's mass necessary for low pressure sensing.

The Amphenol die employs six implanted resistors within its upper relief. As shown in Figure 13, the center horizontal thick relief pair (dark color) contains two resistors beginning at the left edge of the diaphragm, which are connected in series. In the center, are two more piezoresistors, which are additionally connected to another set of series resistors at the right edge, forming a Wheatstone bridge. Note, in Figure 13 the lower-left arm of the thicker relief is a split circuit for ground, or negative connections to the die. This split circuit

divides the Wheatstone bridge into two, allowing better balancing and zeroing of the device. Figure 14 shows a microphotograph side view of the 30 INCH-D-MV sensor. The sensor's silicon support structure, which contains a bottom-side machined cylindrical orifice, is bonded to its ceramic PCB substrate with a white adhesive. The adhesive is likely comprised of a low-stress silicone acting as a buffer against thermal mismatches between the two materials. Other biopressure sensors in the literature have used Corning RTV 3140 silicone, for example, which has demonstrated minimal thermal mismatch stresses with silicon [117].

Thereupon the silicon support structure is the pressure sensor's monocrystalline silicon die with an upper single crystal epitaxial layer. The intermediate diffused marking is a tooling artifact and not present on all sides of the die. The fabrication process is described by Dauenhauer (the manufacturer's co-founder and co-inventor of CoBeam2 technology) and Reimann in U.S. Patent 5,178,016 Figure 8, in which the sensor's diaphragm thickness is approximately that of the epitaxial layer [116]. Further described within the patent is the sculptured diaphragm's upper relief containing a 3,000 Angstrom thick chromium metal layer formed by sputter deposition. Figure 15 shows the wire bonded die mounted on its ceramic PCB substrate secured and sealed by the white flexible adhesive. The bottom of the PCB provides an orifice for fluid communication to the die's opposite/bottom side diaphragm. Figure 16 shows nearby film resistors, having been laser trimmed (horizontal score mark) for precise balancing of the bridge.

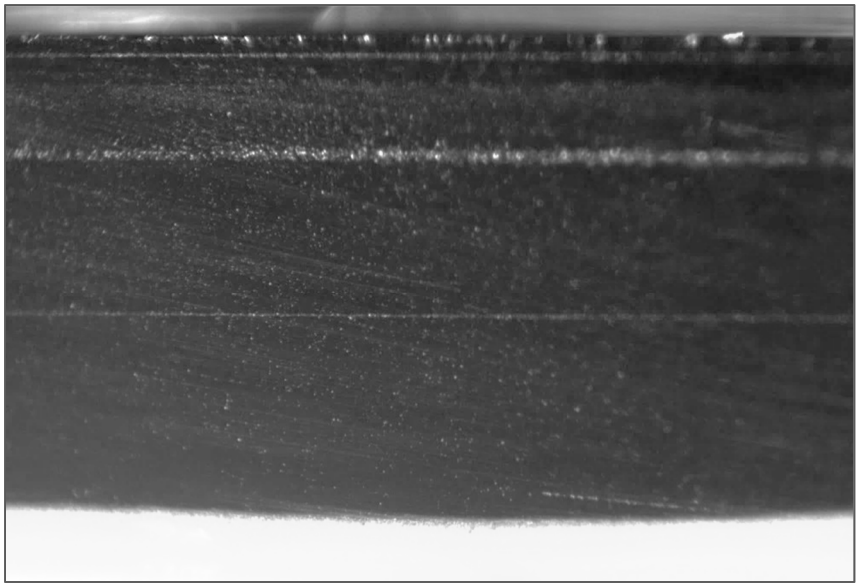


Figure 14 – 30 INCH-D-MV side view at 40X (photo border provided for clarity).

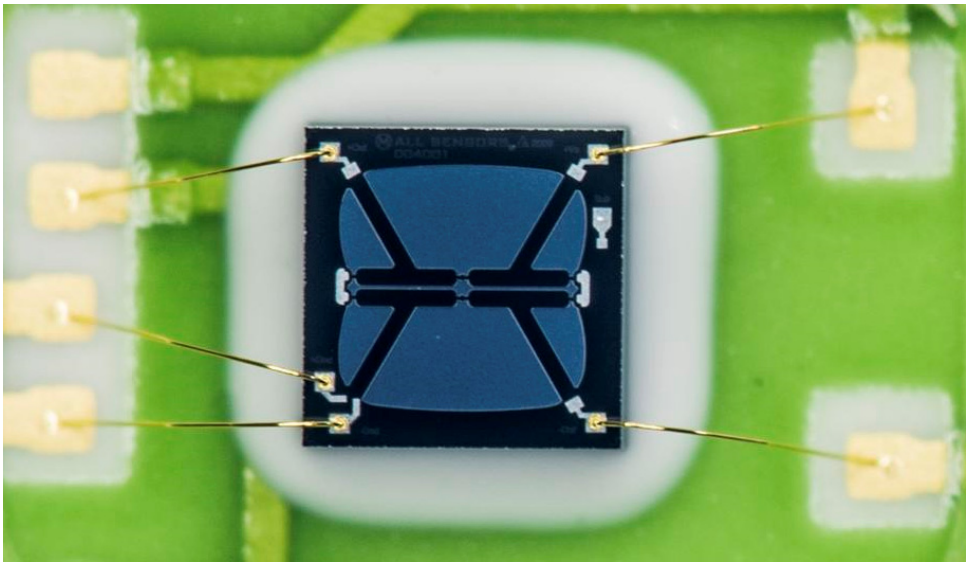


Figure 15 - Amphenol sensor die deployment upon ceramic PCB with soldermask.

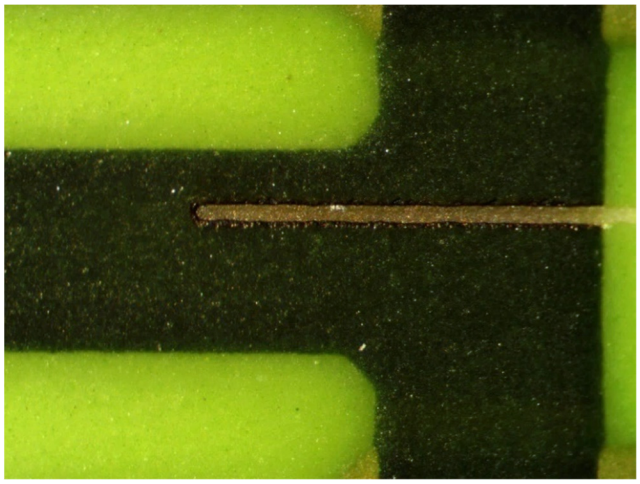


Figure 16 – Laser trimmed film compensation resistors.

As shown in Figure 13 and Figure 15, the Amphenol die is anisotropically etched to produce a square diaphragm. Clark and Wise derived the governing electromechanical equations for *rectangular* thin diaphragm silicon pressure sensors using finite difference numerical methods [106]. The analysis revealed a 50% improved sensitivity for square diaphragms over circular implementations of the same dimensions (i.e. square length equal to circular diameter).

Piezoresistive characteristics are key for maximizing sensitivity, including location, physical size, conductivity and type, orientation, doping levels, and temperature [101, 106, 118]. Under load, stress is highest along the periphery of the diaphragm, both for rectangular and circular diaphragms. Stress, as a function of position from center-to-edge, begins to gradually increase at the point approximately two-thirds radial distance from the center. Beyond two-thirds distance from the center, stress rapidly increases to a maximum at the edge, where resistor placement is most sensitive [106]. Implanted piezoresistors average stress over their geometry and for the Wheatstone bridge, maximum pressure sensitivity is achieved using two parallel and two perpendicular resistors in the <110> direction [68]. Accordingly, the diaphragm is oriented in the <110> direction.

The physical size of piezoresistors presents a trade-off between reproducibility, which increases with size, and pressure sensitivity as resistor size decreases. From Figure 13 it can be seen that the Amphenol edge resistors, implanted within the upper relief's moment arm, are physically placed parallel to each other,

yet in series by virtue of the adjoining edge metal. This arrangement maximizes sensitivity of the edge piezoresistors to capitalize on the stress presented by the diaphragm's edge by implanting dual short resistors. The two resistors increase resistance in series and, hence, maximize the gauge factor and gain of the sensor.

The sensor manufacturer specifies an input impedance of 4.5kΩ and an output impedance of 1.5kΩ for the sensor module, which incorporates two identical dies connected in parallel. Therefore, the equivalent individual die input resistance can be deduced to 9 kΩ with an output resistance 3 kΩ for each die. It can be derived that for a balanced bridge circuit, with equal bridge resistors and equal span resistors, the input resistance is given by any bridge leg piezoresistor plus twice the resistance of either span resistor [119]. The output resistance is simply the value of any bridge leg piezoresistor.

Amphenol provides a schematic representation of the bridge circuit with span resistors for temperature and offset compensation on the power supply inputs. These resistors are actually located on a separate printed circuit board located in close proximity to the sensor die. Taking into account the series connected edge piezoresistors, the actual die effectively consists of four overall bridge resistors.

The Amphenol sensor specifications indicate a typical settling time of 100 μsec or less for 10 to 90% signal. Consequently, a delayed sampling, either during testing/evaluation or in actual deployment, will be necessary to prevent an ADC

conversion from occurring while the sensor is still yet settling from power up. In an effort to minimize any error induced by sampling the sensor's output signal, it is desirable to understand the settling time of the sensor to less than 1% error. The 10 to 90% rise time of a single time constant circuit is approximately:

$$t_{rise} \cong 2.2\tau$$

Since the sensor manufacturer specifies a 100 μsec 10 to 90% rise time, a single time constant estimation was calculated. Substituting into the equation results in a τ of 45 μsec. For less than a 1% settling, more than four exponential time constants are required and therefore, five was chosen in order to arrive at a metric necessary for a delay circuit. Five-time constants results in a delay of 227 μsec.

Since a single-time constant circuit can be configured from an equivalent resistor and capacitor network, a capacitor value can be derived from the single time constant equation of 100 μsec = 2.2•1.5kΩ•C, where C equates to 30.3 nF. Decoupling the dies from parallel to independent sensors, the equivalent capacitance for each die is 15.15 nF with an output resistance of 3kΩ. Therefore, the single-pole bandwidth of each sensor die is approximately 3.5 kHz. The manufacturer's model of the sensor is shown in Figure 17, while the actual individual die's bridge model is shown in Figure 18.

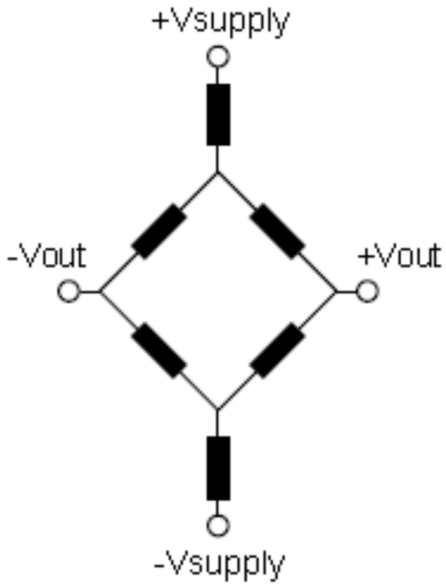


Figure 17 – Amphenol published equivalent circuit.

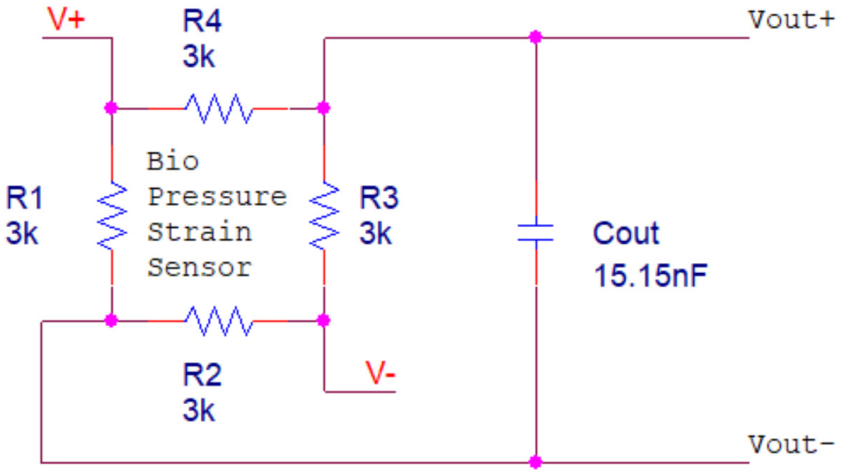


Figure 18 – Derived Wheatstone bridge pressure sensor model.

All considered, the Amphenol 30 INCH-D-MV die was selected for further research and development within this work given the die possesses a sensitivity of 2.19 μV/V/mm H_2O, a span of ±762 mmH_2O, variable low voltage operation, and parylene biocompatibility in an area of approximately 2 mm^2. Very importantly, Amphenol can produce matched die components. With regard to resolution, the sensor is specified with a linearity and/or hysteresis error of 0.05% FSS, which equates to 0.38 mm H_2O. Complete specifications of the device are provided within the Appendix.

Sensor System Design

Koskinen's research found that the Codman microstrain device demonstrated low pressure drift, deemed clinically acceptable, whereas Piper concluded the opposite regarding the Camino fiber optic system. Although microstrain devices are indeed sensitive to thermal effects, silicon based microstrain devices offer the opportunity for bandgap temperature compensation techniques or compensation via resistors with offsetting thermal coefficients which may further be precisely trimmed. Considering the sensor system altogether, the consensus from the literature review is that microstrain devices present less drift in clinical deployments. Therefore, this research will seek to advance upon these findings for microstrain devices by further developing and evaluating means for minimizing and/or mitigating residual inaccuracies within the sensing mechanism.

Cross-Coupled Dual-Die Single-Reference Pressure Sensor

One such means for potentially reducing drift is by employing two piezoresistive pressure sensors on a common substrate, such as ceramic. In such a configuration, two pressure sensors may be arranged to encounter mechanical stresses in common-mode and therefore negate, or offset, erroneous sensor read-out effects. Such a system is described by Dauenhauer et. al. in U.S. Patent 6,023,978 as a pressure transducer with mechanically cross-coupled fluidic pressures stimulating two alternating sensor die faces with error compensation further comprising electrically cross-coupled outputs of the two sensors [120]. In this system, conceptually shown in Figure 19, one pressure acts as a reference pressure (e.g. atmospheric) and another is the unknown pressure under test.

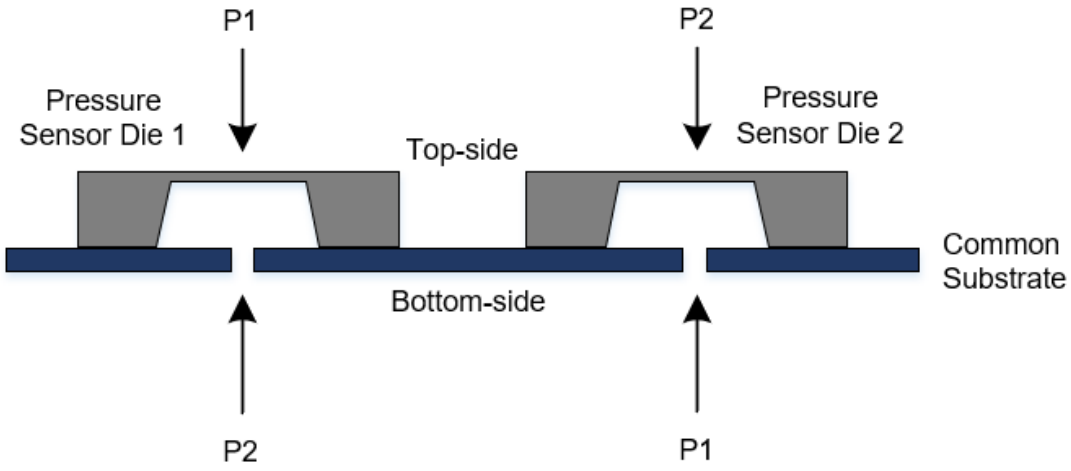


Figure 19 – Illustrative cross-section concept of dual pressure sensors with each P1 and P2 cross-coupled to top-side and bottom-side dies.

In the dual sensor configuration shown in Figure 19, the sensor dies are co-located upon a common mounting substrate whereby stresses become common mode. By virtue of the sensors' cross coupled outputs, as shown in Figure 20, the total output signal becomes the superposition of the two sensors, subtracting out the common stress. In order to do so, each sensor's transfer function must be substantially identical to the other and therefore necessitates matched silicon dies.

Performance matched sensors use die taken from the same silicon wafer, since error characteristics are predominately process related [120]. Sensor dies located within the same area of a wafer tend to have even further similar performance characteristics. For matched sensor dies, two die are often selected which are adjacent to each other during wafer dicing. Such dies typically share the same effects of equipment registration (or misregistration as the case may be), such as orientation for ion implantation and other localized effects, including etch rate characteristics (evaporation rates, temperature gradients, impurities, etch area exposure distribution, or loading, etc.). Adjacent pressure sensor dies also typically possess substantially similar zero and gain coefficients with temperature, being largely controlled by impurity concentration of doped regions [121]. Selected dies are thereafter measured, and further sorted if necessary, to verify equivalent transfer functions, including gain, offset, and linearity over operating parameter ranges (e.g. pressure, temperature, bias, etc.).

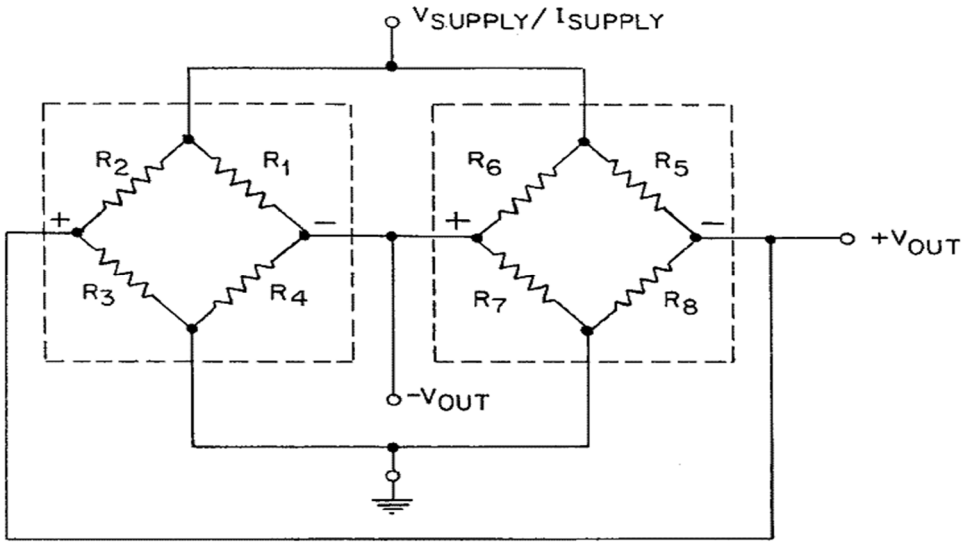


Figure 20 – Cross coupled dual sensor configuration for error compensation.

Matched sensors are of importance in large systems necessitating differential pressure measurements where sensors may not be co-located, otherwise allowing one differential sensor. Additionally, matched sensors are important for systems, such as that described herein, designed to eliminate common mode interference.

In the Dauenhauer dual sensor configuration the pressure sensors are deployed in differential pressure mode in which one sensor serves as a reference sensor (e.g. atmospheric) to the second, which receives the pressure to be measured. The technology was licensed by All Sensors Inc. from Honeywell Data Instruments and thereafter commercialized under the CoBeam2 brand, which was later acquired by Amphenol. For implantable use, the device would require an absolute reference or reliable means of atmospheric sensing. Providing either of these are challenging. One potential method may consist of a gas chamber to

pressurize the reference port. However, this essentially becomes an absolute pressure sensor, leaving the overall sensor configuration vulnerable to drift by gaseous diffusion and leakage. An alternative option may integrate a large broad subcutaneous liquid bladder connected to the sensor's reference port in order to normalize any parasitic pressure from localized tissue growth yet communicate atmospheric pressure on average. However, for ICP measurements, CSF pressure is position dependent. Therefore, such a reference bladder would produce one differential pressure in one position and yet another differential pressure in a second position due to a changing reference, rendering the true CSF pressure elusive.

Independent Dual-Die Dual-Reference BioPressure Sensor

One solution for obtaining the benefits of a matched dual-die pressure sensor configuration is to actually decouple the two sensors and provide a *common* absolute reference as shown in Figure 21. In this configuration, the sensor system provides two matched pressure sensor dies with a common pressure reference, yet two independent sensors, as shown in Figure 22, for measuring a reference pressure and, separately and independently, cerebrospinal fluid.

The specifications and deployment of the dual biopressure sensor are described in U.S. Patent 9,668,663 as a result of this research, with other patents pending. The design may utilize a ventricular catheter, or alternatively a parenchymal pressure bladder, for fluid communication with a brain's ventricles as illustrated in Figure 23 [47].

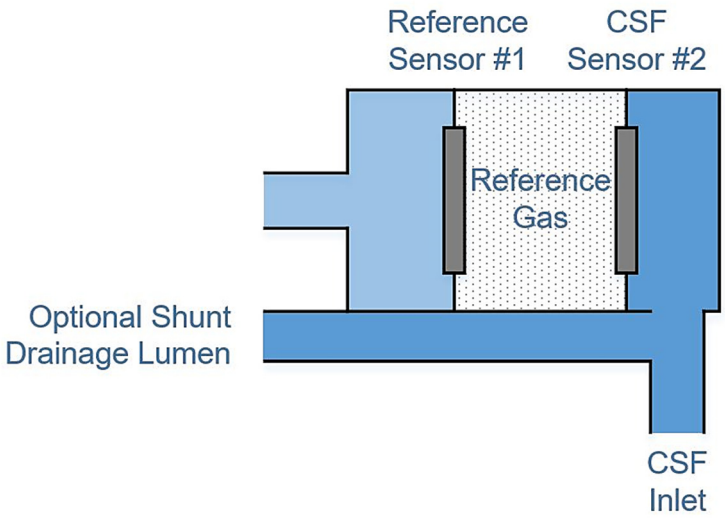


Figure 21 - Independent dual sensor with absolute reference configuration for error compensation.

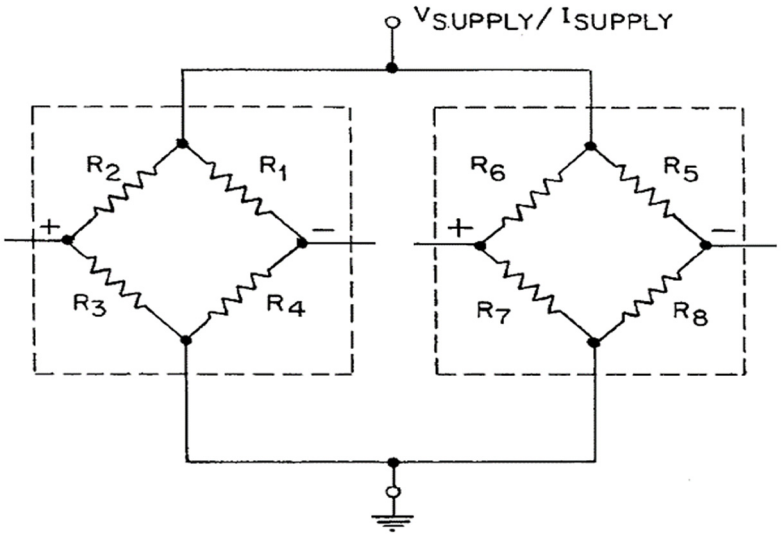


Figure 22 – Independent output dual sensors with common power/bias rails.

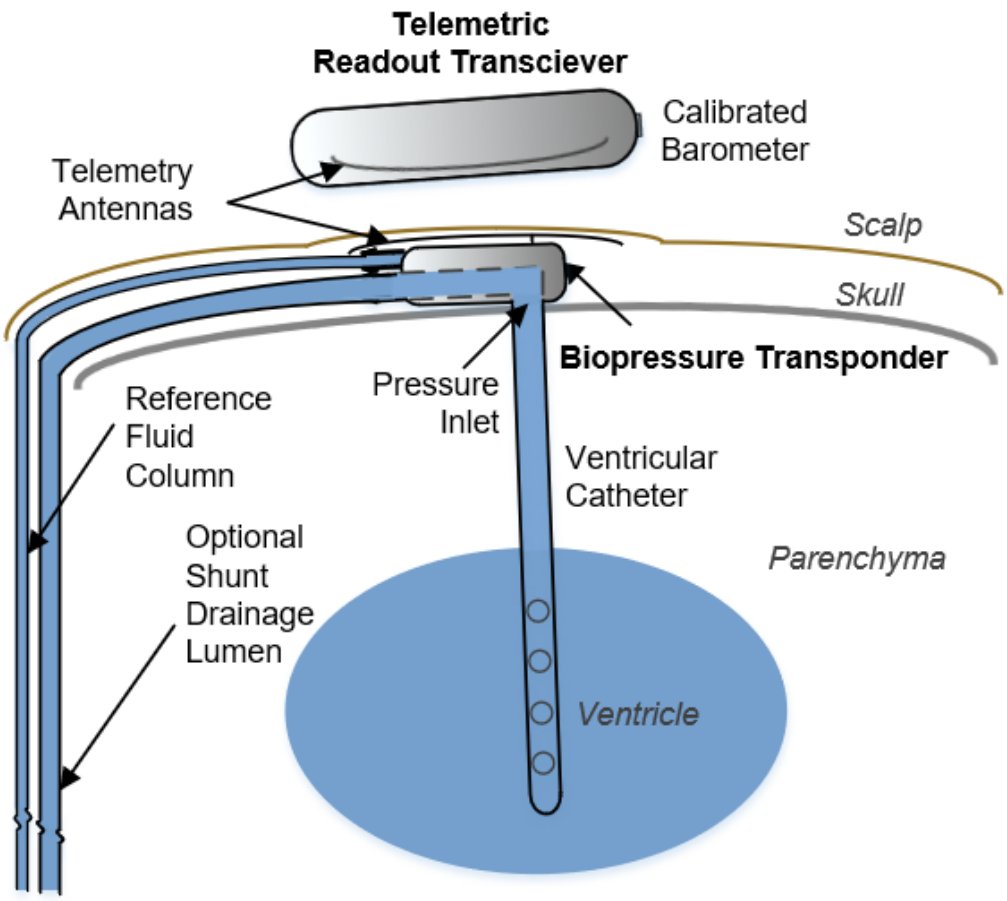


Figure 23 – Biopressure transponder deployment with ventricular catheter.

Figure 24 illustrates the alternative fluid bladder pressure transducer for parenchymal measurements, which may reduce dependency on flow or slit ventricle complications in sensing pressure. The reference port would employ a peritoneal catheter, providing an a-priori saline column serving as a known position dependent pressure reference. The peritoneal catheter's ability to provide such a position dependent pressure reference, being a function of fluid density and length, has been well characterized. Since the 1960's, when ventriculoperitoneal shunting became standard practice in the U.S., siphoning began to be researched as a result of its undesirable impact for inadvertently activating shunt valves, resulting in dangerous CSF over drainage effects [96, 122]. Ironically, this siphoning effect may be advantageously utilized as a predictable in-vivo pressure reference source. Complications of peritoneal catheters are rather rare with the most common issues reported being abdominal pseudocyst or hepatic pseudocyst formation. The incidence of these complications ranges in the literature from 1 – 4.5%. However, these complications are thought to be associated with CSF shunt infections or from multiple abdominal surgeries [123]. In the case of the biopressure sensor's use of the peritoneal catheter, specifically as a pressure reference, no CSF will be discharged, notwithstanding a separate peritoneal catheter for CSF shunting purposes. The distal end of the sensor's reference catheter is intended to be open, terminating into the peritoneum, subject to atmospheric pressure. Alternatively, the catheter may simply be implanted in the subcutaneous plane since no fluid drainage is intended to occur.

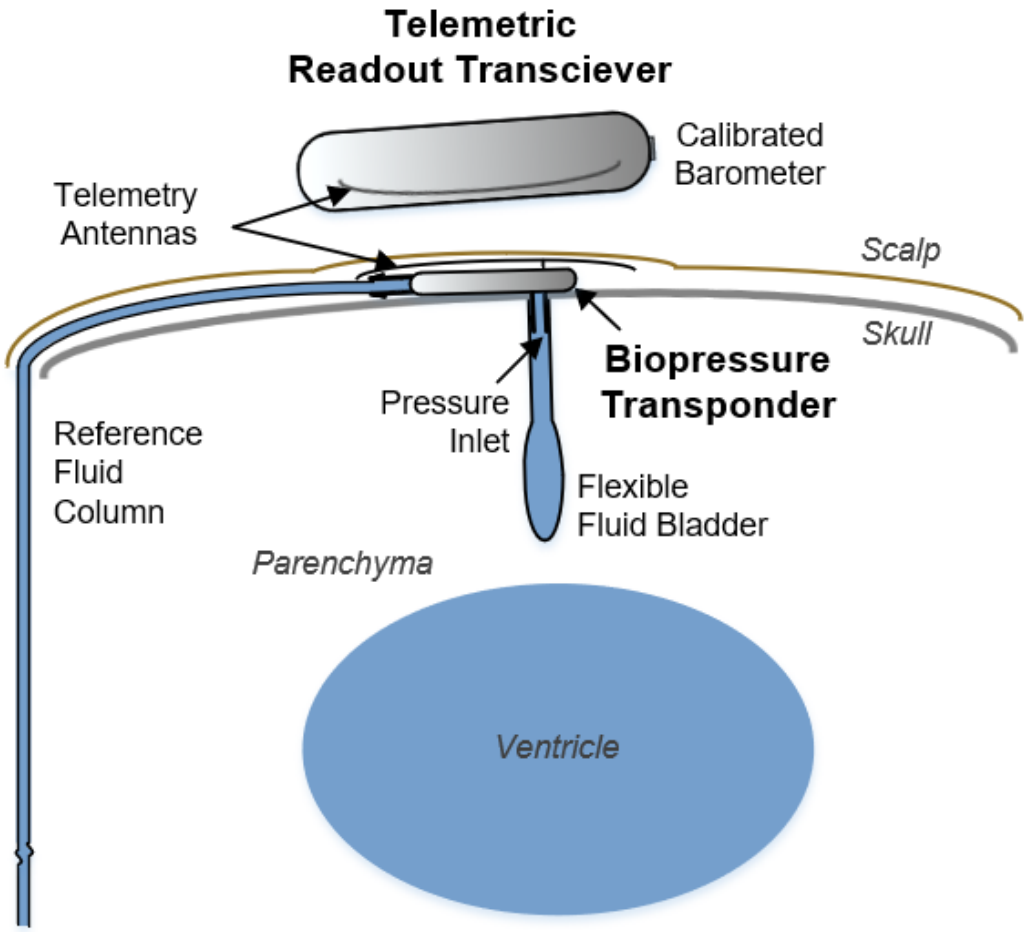


Figure 24 – Alternative transponder deployment with fluid bladder as a parenchyma pressure transducer.

Walker and Criddle's research on the pathophysiology of abdominal compartment syndrome [124] found that the peritoneal cavity normally resides at atmospheric pressure, which was also reported by Drake [3]. The route of the peritoneal catheter, just subcutaneous, from head to abdomen, is also generally at atmospheric pressure, particularly when taken as the average over the catheter's length. In this configuration, as shown in Figure 25, the reference port pressure will be equal to atmospheric, or at a prescribed pressure near atmospheric depending upon routing, in a patient's supine position and approximately -ρgh in the upright position.

In considering each sensor independently and as an absolute pressure sensor with a common reference gas, physiological pressures would be in addition to a full range of possible barometric conditions. Extreme ranges can span from 0.86 atmospheres up to 1.06 atmospheres [125, 126, 127]. These pressures correlate to an absolute pressure sensor capable of 8,872 mm H_2O on the low end up to 11,472 mm H_2O for the highest recorded atmospheric pressure including 500 mm H_2O. However, as will be later shown, appropriate configuration of the dual pressure sensor's common absolute reference under typical conditions (e.g. the mean) results in an acceptable response.

Given the sensor outputs are independent, the gain of the reference sensor can be determined by reading the absolute pressure of the reference column in two patient positions (e.g. supine, or 0°, and upright, or 90°) as follows:

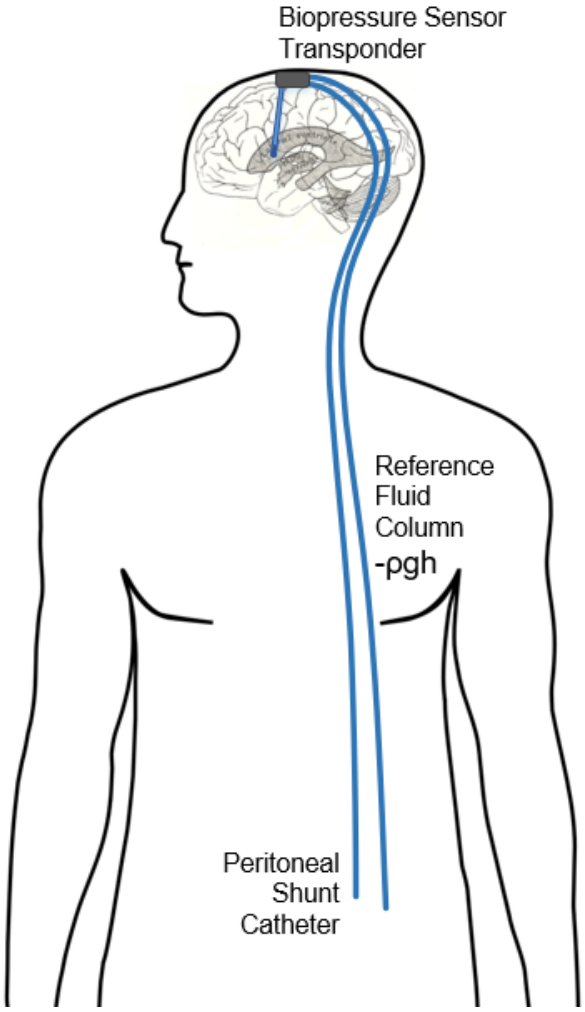


Figure 25 – System deployment of biopressure sensor with reference fluid column and shunt integration (shunt peritoneal catheter shown).

$$m = \frac{v_1(90^\circ) - v_1(0^\circ)}{\left(P_{atm} + P_{col}(90^\circ) - (P_{atm} + P_{col}(0^\circ)\right)}$$

Next, for offset correction, since the reference port is subject to atmospheric pressure and the sensor is read-out in absolute mode, the output will equal the barometric pressure with the patient in the supine position (or barometric less ρgh•cos(θ) in any other position). With a known input pressure (i.e. barometric) being accurately measured ex-vivo via a calibrated barometer, a sensor offset can be derived as follows:

$$b = v_{P_{atm}} - \left(P_{atm} + P_{col}(\theta)\right) \cdot m$$

* where P_{atm} is measured ex-vivo via a calibrated barometer.

Utilizing matched sensor dies enables the corresponding CSF sensor's gain and offset values to be determined via the reference sensor. Therefore, once the system undergoes calibration by means of its reference sensor and peritoneal catheter reference, accurate CSF measurements may be obtained which are compensated for gain and offset drift by:

$$P_{csf}(\theta) = \frac{v_2 - b}{m} - P_{atm}$$

Deployment and Implantation

Figure 23 illustrates the general approach of the transponder and its sensors for human implantation, which in the embodiment shown, an integrated shunt is

provided. As indicated within the literature, ventricular cannulation remains the "gold standard" of ICP measurement. Hydrocephalus patients who undergo ventriculoperitoneal shunting possess ventricular catheters often infection free for years. Therefore, this design will incorporate a subcutaneous pressure transducer implanted just underneath the scalp, connected to a ventricular catheter, or alternatively a parenchymal bladder.

Figure 23 shows a right-angle connection to the ventricular catheter which also facilitates shunt flow of CSF to its terminal site (e.g. the peritoneum, pleura, or atrium). These types of catheters are typically of one-millimeter inner diameter Silastic® (i.e. silicone) with a hardness commonly around 65 Shore A. Due to the soft material, they may remain compliant, even when occluded, and, in a closed pressure system, may partially transmit ICP to the transponder. Ventricular cannulation also allows for the transponder's implant site to be remote, just under the subcutaneous plane of the scalp, for improved telemetry coupling compared to a deep implant.

Additionally, shown in Figure 23 is the transponder's reference fluid column comprising a saline solution. The reference lumen connects to the transponder's Reference Sensor #1, as shown in Figure 21, to provide a position dependent pre-known pressure reference. The transponder is anticipated to be titanium construction utilizing glass-to-metal seals for integrating the telemetry antennas, which are external to the transponder housing, yet subcutaneous. The transponder's signal antenna will carry the pressure signal while a second

antenna will facilitate inductive power coupling. Although the design, given its subcutaneous placement, could possibly utilize optical coupling, hair upon the scalp could significantly impede such an approach. Therefore, this design will be slated for electromagnetic telemetry for both power, via inductive coupling, and high-frequency near-field pressure readout communications. The transponder may therefore be entirely passive without any internal power source.

Supporting non-invasive readout of pressure, the transponder may utilize Bluetooth LE for low-power digital communications. Bluetooth LE is compatible with modern smartphones and thereby facilitates easy readout on readily available multipurpose devices. Several smartphones, including the iPhone 6 or later, include a barometric sensor, which may be utilized for offset correction.

Figure 26 provides a block diagram of the transponder's electronics whereby the pressure sensor is amplified by a low power instrumentation amplifier (IA). The IA output is fed into a Texas Instruments microcontroller's analog input. The CC2541 integrates a Bluetooth LE transceiver and Bluetooth software stack. Separately, the Texas Instruments BQ500210 and ST Microelectronics STWLC04 chipset provides a telemetry control unit and receiver for transcutaneous inductive powering of the transponder. The ST Microelectronics STWLC04 is optimized for 1W power transfer providing an approximate 60% efficiency, thereby lowering the required transcutaneous energy transfer versus other receivers.

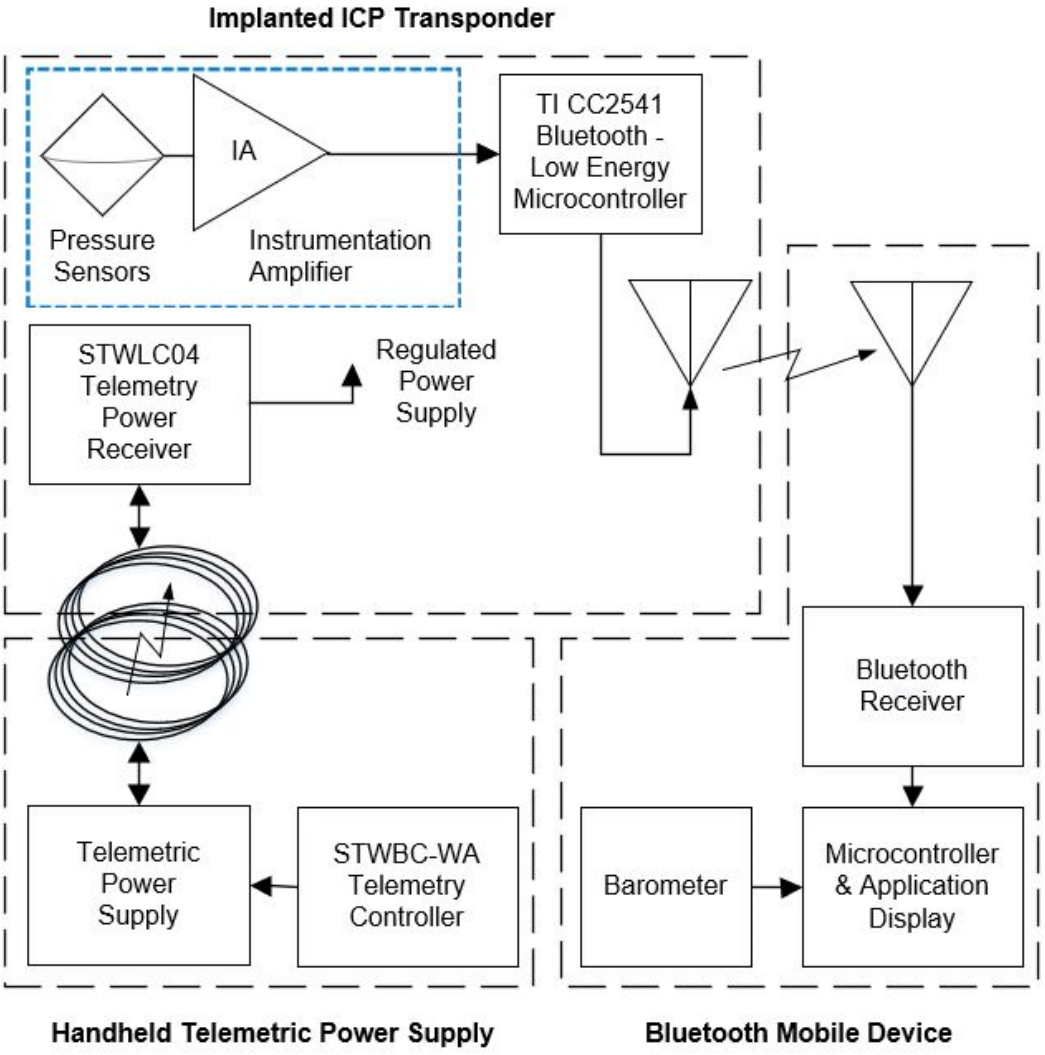


Figure 26 – Transponder and readout deployment block diagram.

(research focus outlined in blue dotted line)

Electronics Readout Overview

Readout of the ICP pressure sensors, described in prior sections, is comprised of a two-part assembly. The first encompasses the ex-vivo powering and demodulating unit for physician or patient use and interpretation. This functionality may take advantage of smartphone integration utilizing a Bluetooth LE enabled device to provide communication and a user interface while a second module transcutaneously powers the transponder. The second part of the system consists of the implantable pressure transponder, which contains the dual biopressure sensor and receives power from the first system, responding with a Bluetooth LE encoded pressure signal. The transponder's pressure sensor(s), and specifically its limitations of accuracy, are the object of research within this work.

Figure 26 lays out the general approach of the pressure transponder and readout mechanism. The front-end analog electronics consists of an instrumentation amplifier which then supplies an amplified analog representation of pressure to the analog-to-digital converter (ADC) of the microcontroller. Amplification of the sensor's low voltage signal is necessary to produce an adequate signal-to-noise ratio with a low output impedance voltage driver for the ADC.

Each sensor's output is a differential signal generated by the Wheatstone bridge strain gauge supplying an amplifier with a very high input impedance which minimizes input loading effects. Since the sensor's output signal is 2.19 μV/V/mm H_2O, a high gain is needed very close to the sensor in order to boost

an unadulterated sensor signal above the noise floor present within the remainder of the transponder's circuit. Since the pressure sensor is intended to operate within a relatively stable pressure environment and with a sample and read approach, a low bandwidth analog channel is all that is required, which helps reduce power and noise. With these considerations in mind, an operational amplifier topology was evaluated in a differential mode. Figure 27 shows the topology of an operational amplifier differential configuration. The gain of the amplifier, for $R_f = R_g$ and $R_1 = R_2$, is given by:

$$\frac{v_o}{v_1 - v_2} = -\frac{R_f}{R_1}$$

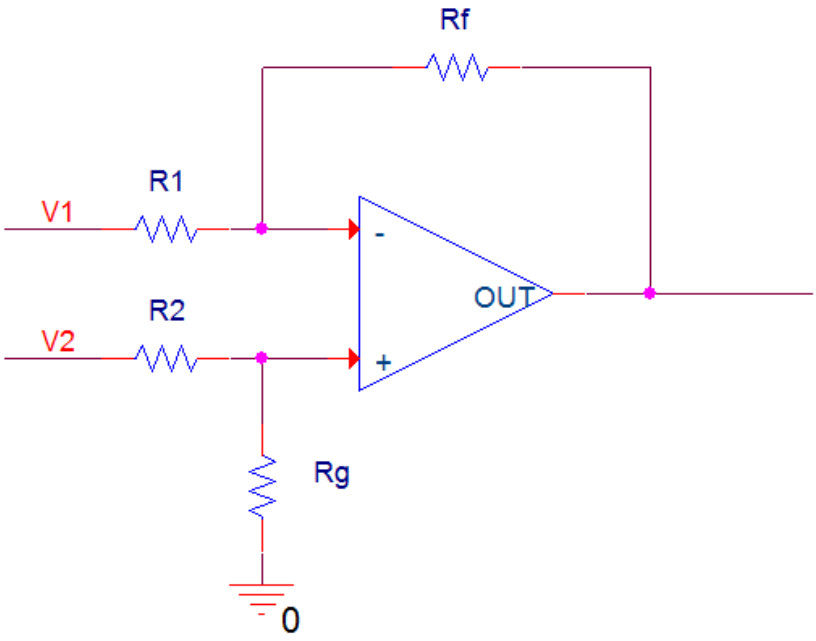


Figure 27 – Operational amplifier differential configuration.

and the input impedance is:

$$R_{diff} = R_1 + R_2$$

Since this design is seeking a very high input impedance, as well as a high gain, it can be seen that in order to have a high gain with a high input impedance, R_f would quickly become extraordinarily large. A large resistance can be challenging to control and in the deployment of an implantable transponder, such a large resistance determining the gain could become detrimental when considering any possible moisture intrusion that may affect its value.

An alternative approach to buffering the sensor's differential signal is the use of an instrumentation amplifier as shown in Figure 28. For a CMOS or JFET instrumentation amplifier, the input impedance looking into the non-inverting inputs are nearly infinite with extremely low bias currents and therefore the gain of the amplification stage is independent of the input signal's impedance. The second stage of the instrumentation amplifier is simply the differential amplifier of Figure 27. The gain of the instrumentation amplifier can be shown [103] to be:

$$\frac{v_{out}}{v_1 - v_2} = -\frac{R_3}{R_2}\left(1 + \frac{2R_1}{R_{gain}}\right)$$

Therefore, the gain of the amplifier can be adjusted by one resistor, which is typically external for instrumentation amplifier integrated circuits (IC). In addition to very high input impedances and a topology allowing high gains, it can also be

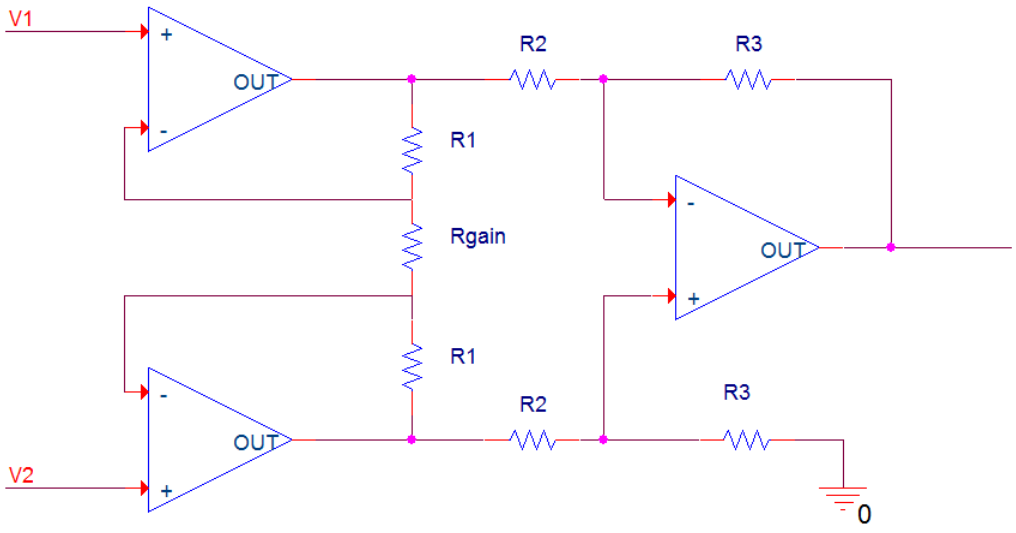


Figure 28 – Instrumentation amplifier.

shown [103] that the instrumentation amplifier possesses very high common-mode rejection (i.e. ≥ 100 dB typically) in cases where the amplifiers gain resistors are very well matched, as is typically the case in modern ICs. An additional benefit of the instrumentation amplifier is the node presented by R3, whereby a ground connection can be substituted with an offsetting reference. This feature is attractive for allowing low voltage operation of the transponder whereby bipolar operation of the pressure sensor can be achieved using only a positive power supply by establishing an offset ground/common node (e.g. at 2.5V). The downside of the instrumentation amplifier is that it can be more power consuming and potentially more expensive.

A search was conducted for a low power, low offset voltage instrumentation amplifier with a high gain potential to mitigate the transponder's typical noise floor. Table 3 shows a narrowed selection of instrumentation amplifiers from Texas Instruments (TI) and Analog Devices (AD). The selection was narrowed based upon low power and then evaluated for other requirements. Although the INA-126 offers the lowest quiescent current of all considered, it also presents highest noise figure and least immunity. The INA-141 was used in prior biopressure sensor research due to its low noise figure, high CMRR, and very low offset voltage and was further used in long-term testing later described [128]. However, the AD8222 was discovered to further offer higher performance in each of these categories, only sacrificing maximum power supply at 18V versus 36V

Table 3 - Low power instrumentation amplifiers.

	TI INA126	TI INA141	TI INA129-EP	AD 8222	
Vcc (max)	36	36	36	18	V
Vcc (min)	2.7	4.5	4.5	2.3	V
Input Bias Current	25	5	5	1	nA
Input Offset	3.0	0.5	0.5	0.3	µV/°C
Noise @ 1kHz	35	8	8	8	nV/rt(Hz)
CMRR	83	117	120	126	dB
Non-Linearity (max)	0.002	0.002	0.002	0.002	%
Bandwidth @A=100	9	200	200	140	kHz
Quiescent Current, Iq	0.175	0.750	0.700	1.000	mA

and bandwidth at 140 kHz versus 200 kHz, of which neither parameter was unacceptable for the sensor application.

Methods

This section describes the methods for simulation and evaluation of the new sensor design described within the Approach. Of key interest is the evaluation of drift mechanisms and any mitigating results of the new sensor and its calibration method. This section outlines the methods for verifying the requirements and objectives given by Table 2.

Simulation

As referenced in the Sensor Technology section of the Approach, in order to negate the sensor's offset and piezoresistor temperature response, all four bridge piezoresistors must be near equal. While ratio matching of diffused piezoresistors is quite good relative to absolute tolerancing, it is nevertheless imperfect. Based on the literature review, regional brain temperature gradients of 0.4°C were found extending from the brain's surface to the ventricles. Additionally, temperature variations of 0.2°C were measured over the circadian cycle. Although small, the effect of these variations must be evaluated with respect to the sensor's pressure transduction. To examine any potential impact upon offset or from temperature swings, the resistance of several piezoresistors will be measured to assess the typical extent of possible mismatch. Additionally, the piezoresistors' thermal coefficient will be determined by temperature testing

in the laboratory. With these values, PSPICE circuit simulations will be conducted to assess the extent of any impact upon pressure transduction. Additionally, thermal simulations will be conducted using COMSOL to evaluate any concern from potential Joule heating of the sensor itself upon CSF or surrounding tissues.

Sensor Evaluation

Sensor testing will entail two primary methods. First, the specified Amphenol matched silicon dies with input cross-coupling and output summing (as produced by the manufacturer), shown in Figure 20, will be evaluated uncorrected, to examine long-term inherent drift performance (hereinafter referred to as Uncorrected Sensor Drift Assessment). Secondly, a custom sensor will be developed using two matched dies independently configured as sensors sharing a common absolute gas reference and substrate as described within the Sensor Design section and as illustrated in Figure 22 and Figure 23. The system will be laboratory evaluated as next described (referred to as System Calibrated Sensor Assessment) and in accordance with the operational methods described in the Sensor Design section and in U.S. Patent 9,668,663.

Uncorrected Sensor Drift Assessment

The native sensor drift of matched dies in a cross-coupled and output summed configuration will be evaluated over an extended period of time using the setup shown in Figure 29. The Amphenol BLVR-L30D-B1NS will be selected for most

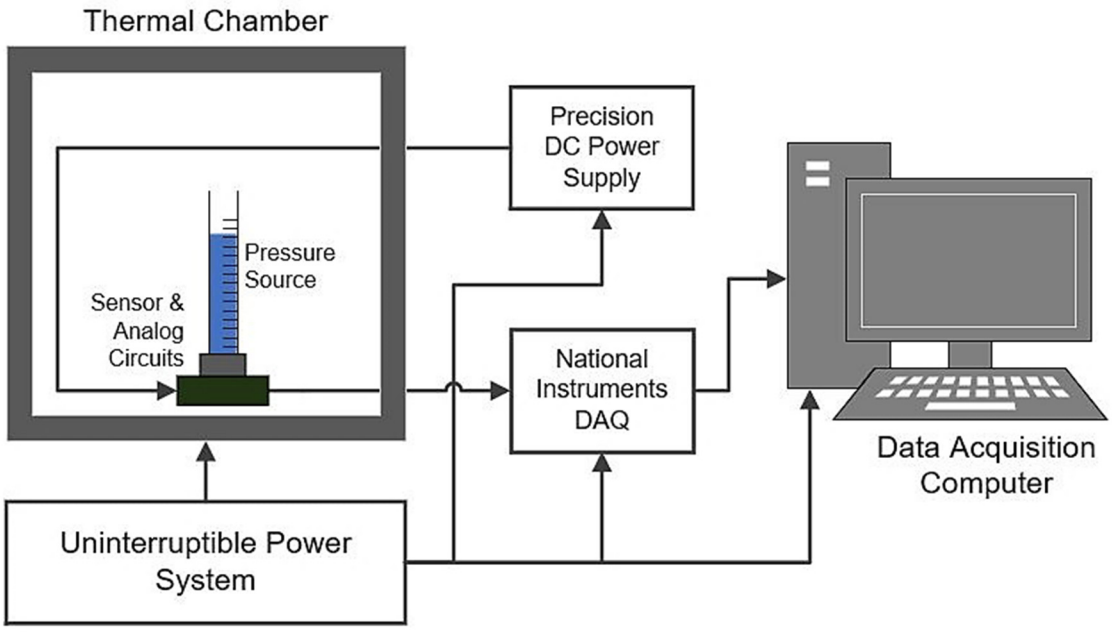


Figure 29 – Long term drift chamber with external and local power supply regulation and thermal stability with data acquisition system under UPS.

closely matching the desired pressure range of -500 mm H_2O to +500 mm H_2O and to represent state-of-the-art driftless sensing. The laboratory setup will employ a temperature chamber to maintain a stable operating environment throughout the evaluation. The temperature will be set to 37°C, simulating human in-vivo temperature. Liquid media input pressure will be provided via a glass cylinder of water. Figure 30 is a schematic of the front-end analog electronics to be used for amplifying the sensor signal. The circuit will utilize precision linear voltage regulators in addition to an external precision power supply. As provided in the schematic, the Amphenol dual matched-die utilizes cross-coupling of the input pressures to opposite sides of the two dies.

Furthermore, the outputs of the two separate dies are summed prior to amplification. This design and configuration currently represents the most advanced commercial device for actively reducing drift. Periodic measurements will be obtained via a data acquisition system (DAQ) as well as periodic manual measurements. The entire system will be sustained via an uninterruptable power system (UPS).

System Calibrated Sensor Assessment

The setup for evaluating the new custom sensor system's ability to mitigate offset and gain drift will entail emulating in-vivo pressure sources by utilizing a reference fluid column (e.g. simulating a peritoneal catheter) and a CSF pressure source. The two dies of the sensor system will be hydraulically connected with pressure sources comparable to those in-vivo. Figure 31 illustrates a benchtop

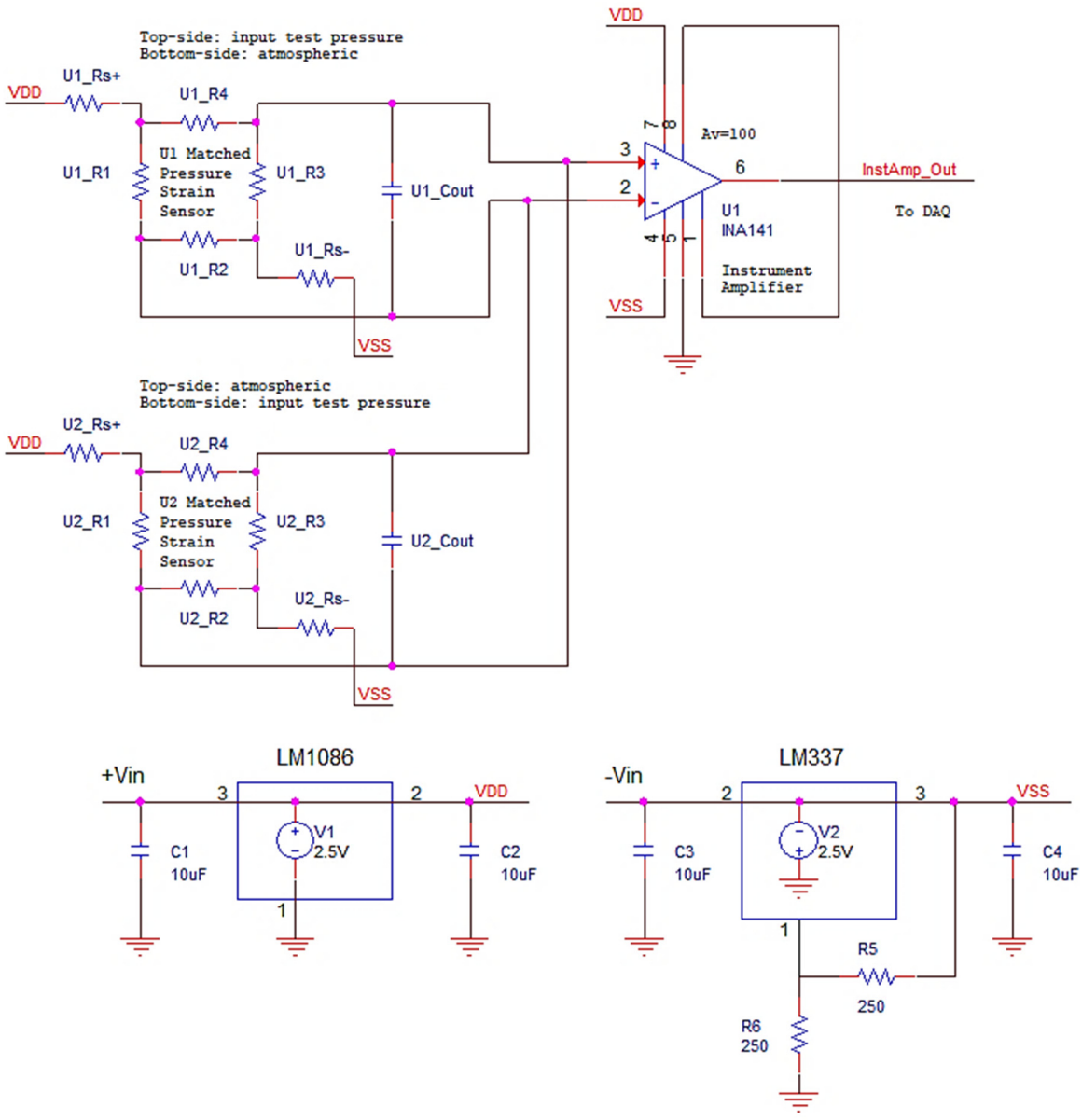


Figure 30 – Front-end circuit for long-term cross-coupled sensor assessment.

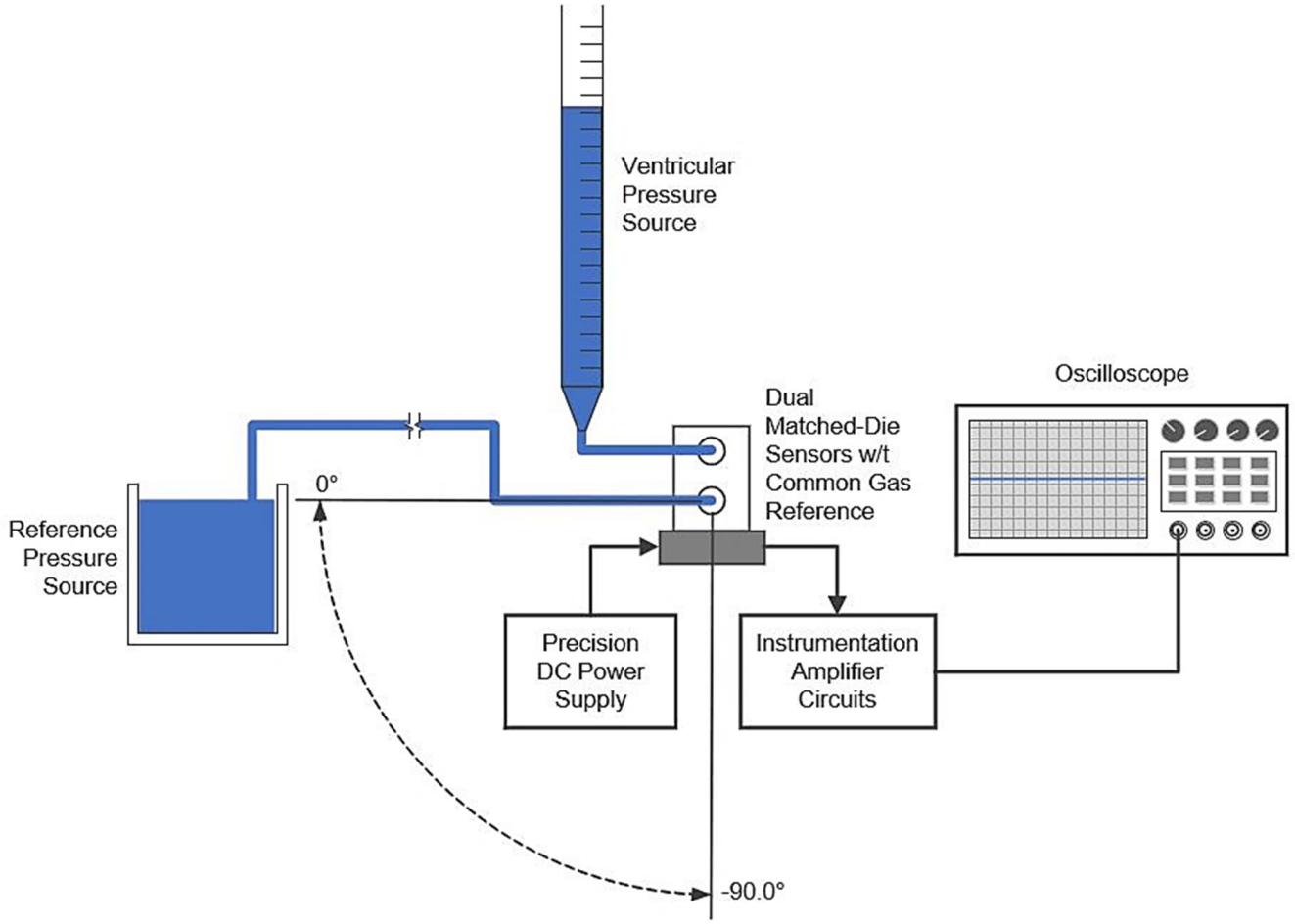


Figure 31 – Dual biopressure sensor test bench with pressure source, precision power supply, instrumentation amplifier, and oscilloscope measurement.

test system incorporating a burette pressure source which will connect to the CSF inlet port of the biosensor. On the biosensor's reference inlet will be tubing of liquid of a prescribed length terminating into a 2L water reservoir. The water reservoir will simulate a large fluid mass representative of the peritoneum or simply the subcutaneous plane. Gain drift will be induced by modulating the sensors' bridge voltage bias.

The overall sensor system, including the input pressure sources, will also be enclosed within a vacuum chamber, as shown in Figure 32. This will allow modulation of the environmental pressure, simulating either atmospheric pressure changes common to the system or a drift of the sensor's absolute reference chamber, necessitating offset correction.

Figure 33 shows the schematic of the front-end analog circuit to be used for the System Calibrated Sensor Assessment. Compared to the Amphenol configuration shown in Figure 30, the two matched dies are decoupled electrically and also distinctively share a common top-side absolute gas reference. In this configuration, mathematical signal processing is performed post amplification, which allows the sensors to be sampled individually over different orientations/positions. For benchtop testing, precision power supplies in close proximity to the system will be used for powering the sensor and test circuits.

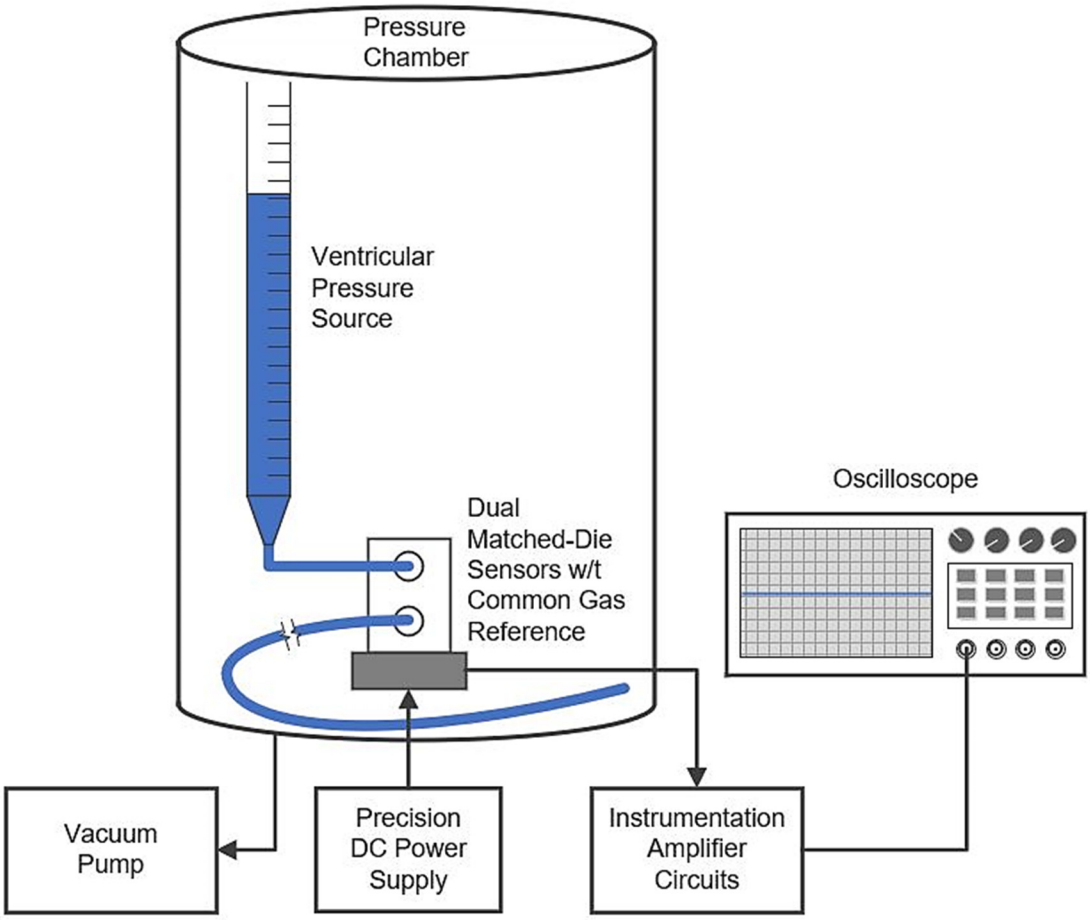


Figure 32 – Isolation chamber with self-contained pressure source for offset testing.

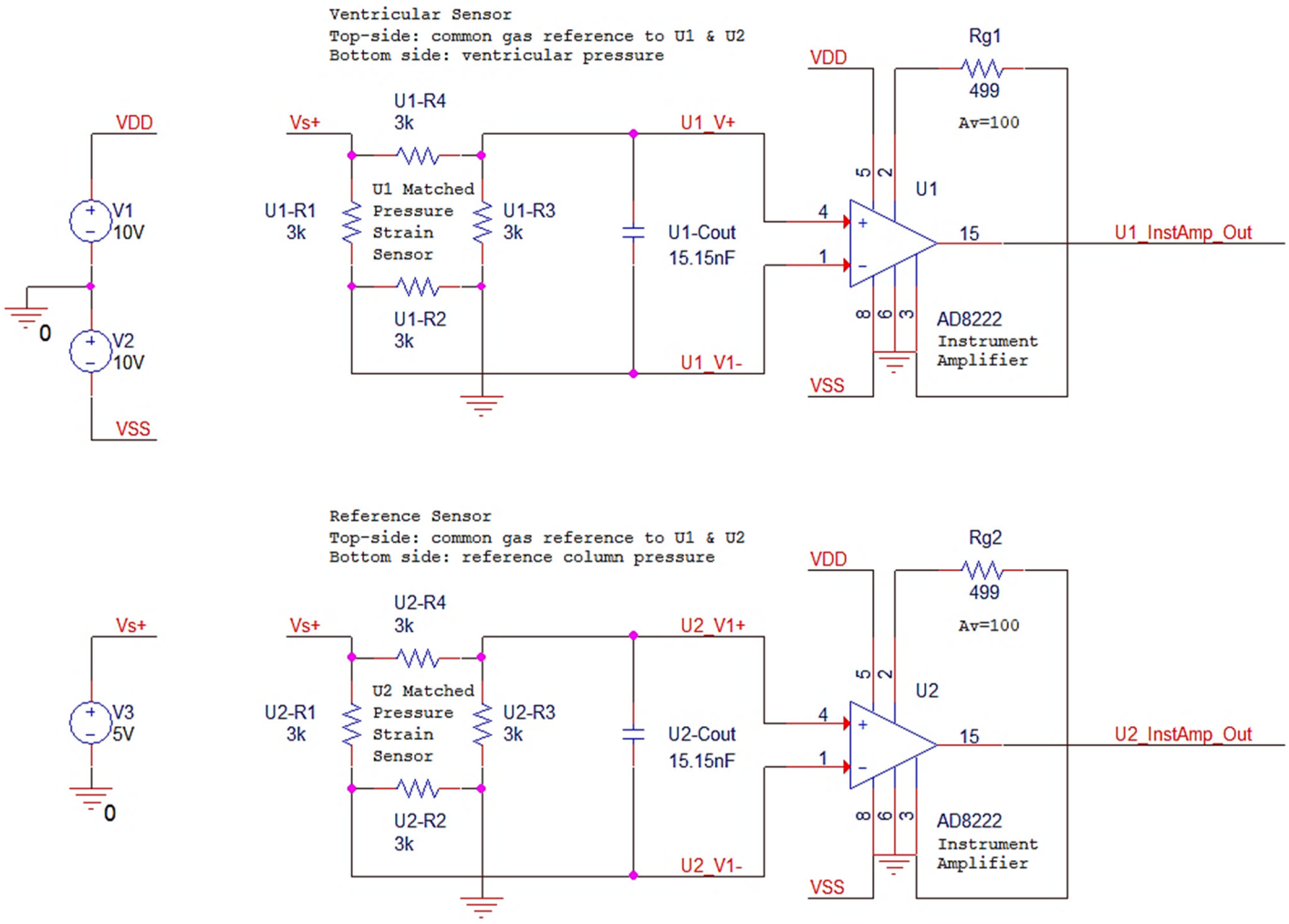


Figure 33 – Front-end circuit for benchtop testing of system calibrated sensor.

The evaluation protocol for the System Calibrated Sensor Assessment will be as follows:

1. Bias the sensor: either to the nominal operating voltage (i.e. ±5.000 VDC) or to an offset voltage (e.g. ±4.000 VDC or ±6.000 VDC), to induce a known gain drift.
2. Measure the reference sensor and CSF pressure sensor's amplified root mean squared (RMS) output voltage with the reference pressure line and water reservoir in the 0° position (i.e. zero pressure above atmospheric).
3. Measure the reference sensor's amplified output voltage with the reference pressure line in the -90° downward position (i.e. a pressure of $P_{atm} – \rho gh$). Record the height, h, in addition to the output voltage.
4. Calculate the gain of the reference sensor using the known reference line's pressure, by virtue of knowing its length/height, liquid density, and barometric pressure for the two positions.
5. With a calibrated barometer reading the station pressure (e.g. located either within the vacuum chamber or deduced by a vacuum gauge and barometer), measure the biosensor's environmental pressure. A vacuum pressure may be used to simulate a known pressure sensor offset.
6. Using the reference sensor's RMS output signal from its reference pressure line in the 0° position, along with the calculated gain, calculate the sensor's offset, b, by equating the signal measurement to the known environmental pressure based on the calibrated barometer.

7. Using the reference sensor’s gain and offset, calculate the CSF sensor’s input pressure.
8. Compare the measured and corrected CSF inlet pressure to the known true CSF input pressure (i.e. liquid level in burette or other source).

CHAPTER FOUR

RESULTS AND DISCUSSION

In the prior chapter, sensor requirements and research objectives were developed based upon research of the literature related to ICP monitoring for hydrocephalus and other intracranial hypertension high risk patients. Fundamental limitations in current pressure sensing technology for long-term monitoring were identified and discussed. A new novel approach, patented as an outcome of this research, was described and developed thereupon. Methods for assessing the latest state-of-the-art driftless sensing technology and the new novel approach described herein were developed. In this chapter, results of the methods will be presented along with discussion related to the results and challenges thereof. Chapter Five will assess the results overall with respect to potential clinical impact and future steps.

This chapter is organized into: 1.) Sensor Simulations 2.) Uncorrected Sensor Drift Results 3.) System Calibrated Sensor Results, and 4.) Non-Ideal Effects and Challenges. The Sensor Simulations section provides results of PSPICE and COMSOL thermal simulations. The Uncorrected Sensor Drift Results provides an assessment of the latest drift-less sensing technology commercially available. The System Calibrated Sensor Results section provides results of the new dual sensor approach allowing self-calibration of the system to mitigate drift. This section will provide results correlating to the objectives outlined in Table 2, including pressure range, resolution, etc. Finally, the section on Non-Ideal

Effects and Challenges will share several of the predominant challenges encountered by this research and how they were overcome.

Sensor Simulations

Simulations of the sensor's bridge circuit was performed using Cadence® PSPICE. To properly model the bridge circuit, several unmatched sensor die measurements were taken under controlled temperature to measure bridge resistance. Table 4 shows the resistance of three different unmatched bridge circuits whereby each bridge piezoresistor was measured at 22.1°C.

As can be seen from the table, the three different unmatched sensor dies produced a large range of resistance compared die to die. This is due to the inherent large parameter drift of diffused resistors in integrated circuit (IC) processing which results in poor absolute accuracy [129]. However, the ability to ratio match resistors in IC processing is much better, which can be seen by the small deviation within each unmatched sensor die's piezoresistor set. The overall average piezoresistance among all resistors sampled was 2.602 kΩ. Amphenol All Sensors modules utilize a second printed circuit board to provide additional circuit resistance to produce consistent input and output resistance and to trim sensor span. Furthermore, the additional printed circuit board provides twin ground resistors which can be laser trimmed to balance the two sides of the bridge and "zero" the output. These resistors connect to the split ground as shown in Figure 13.

Table 4 – Sensor bridge piezoresistance at 22.1°C.

	Unmatched Sensor Bridge		
	A	B	C
R1	3,268 Ω	2,472 Ω	2,020 Ω
R2	3,345 Ω	2,496 Ω	1,998 Ω
R3	3,351 Ω	2,497 Ω	2,020 Ω
R4	3,273 Ω	2,466 Ω	2,023 Ω
AVG.	3,309 Ω	2,483 Ω	2,015 Ω
% DEV.	1.26%	0.57%	0.38%

To more fully model the characteristics of the sensor bridge, piezoresistance measurements were taken over temperature. Figure 34 plots the acquired data for a piezoresistor of 3.096 kΩ at room temperature with a temperature response of 8.49Ω/°C, or 2,940 parts per million (ppm) per degree centigrade. The temperature coefficient and measured resistance mismatch of the bridge's piezoresistors were used for simulating potential temperature and offset inaccuracies of the pressure sensor. Figure 35 provides the schematic used for PSPICE simulation using the worst deviation in bridge resistance given in Table 4. Piezoresistor temperature coefficients of 2,940 ppm were loaded for R1 – R4. A simulation of temperatures ranging from 20°C to 40°C were ran. Figure 36 shows the resulting piezoresistance variation for R1 ranging from 3.276 kΩ to 3.473 kΩ. Figure 37 shows the resulting differential output voltage of the bridge over the same temperature range.

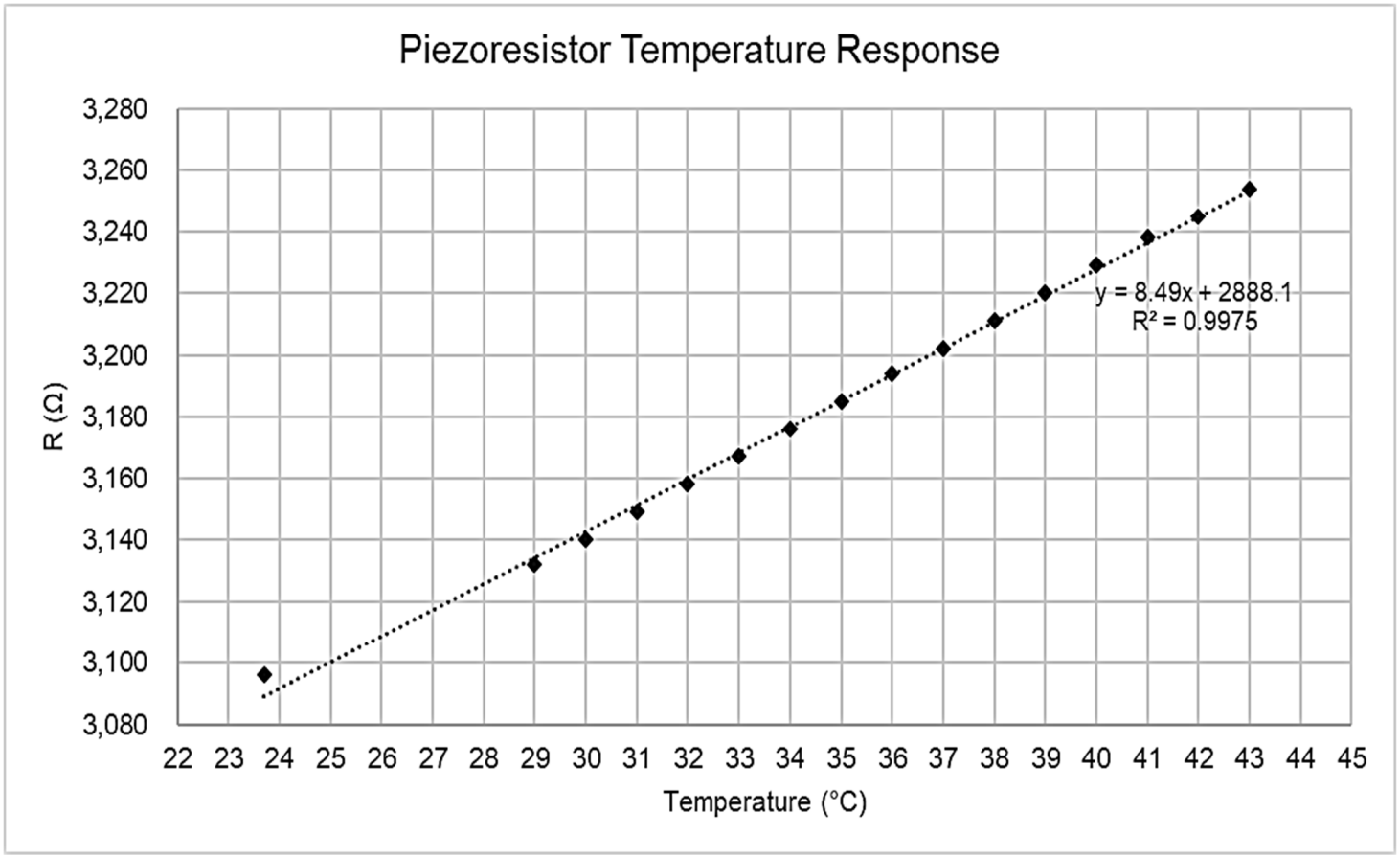


Figure 34 – Piezoresistor temperature response

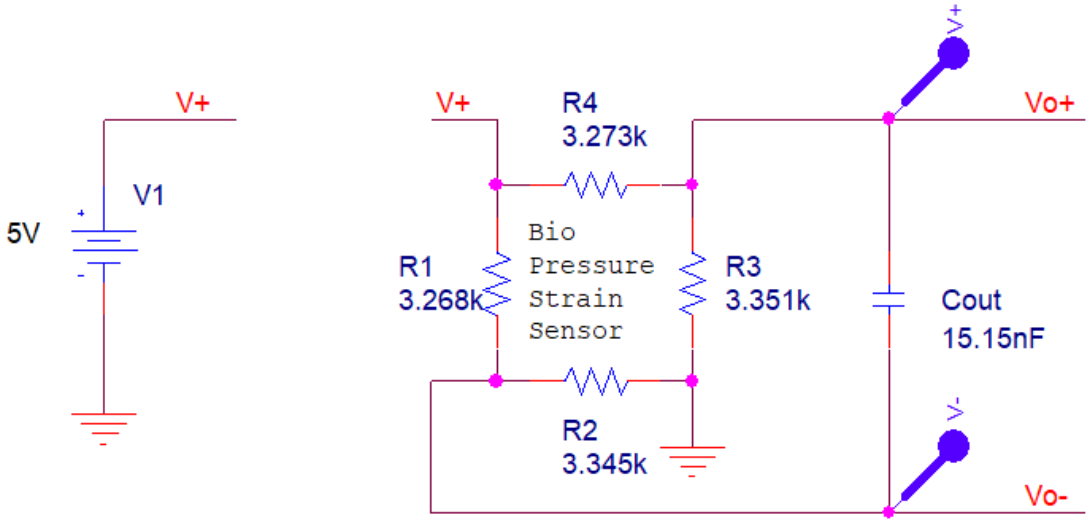


Figure 35 – Sensor bridge PSPICE simulation circuit for piezoresistor mismatch and temperature sweep.

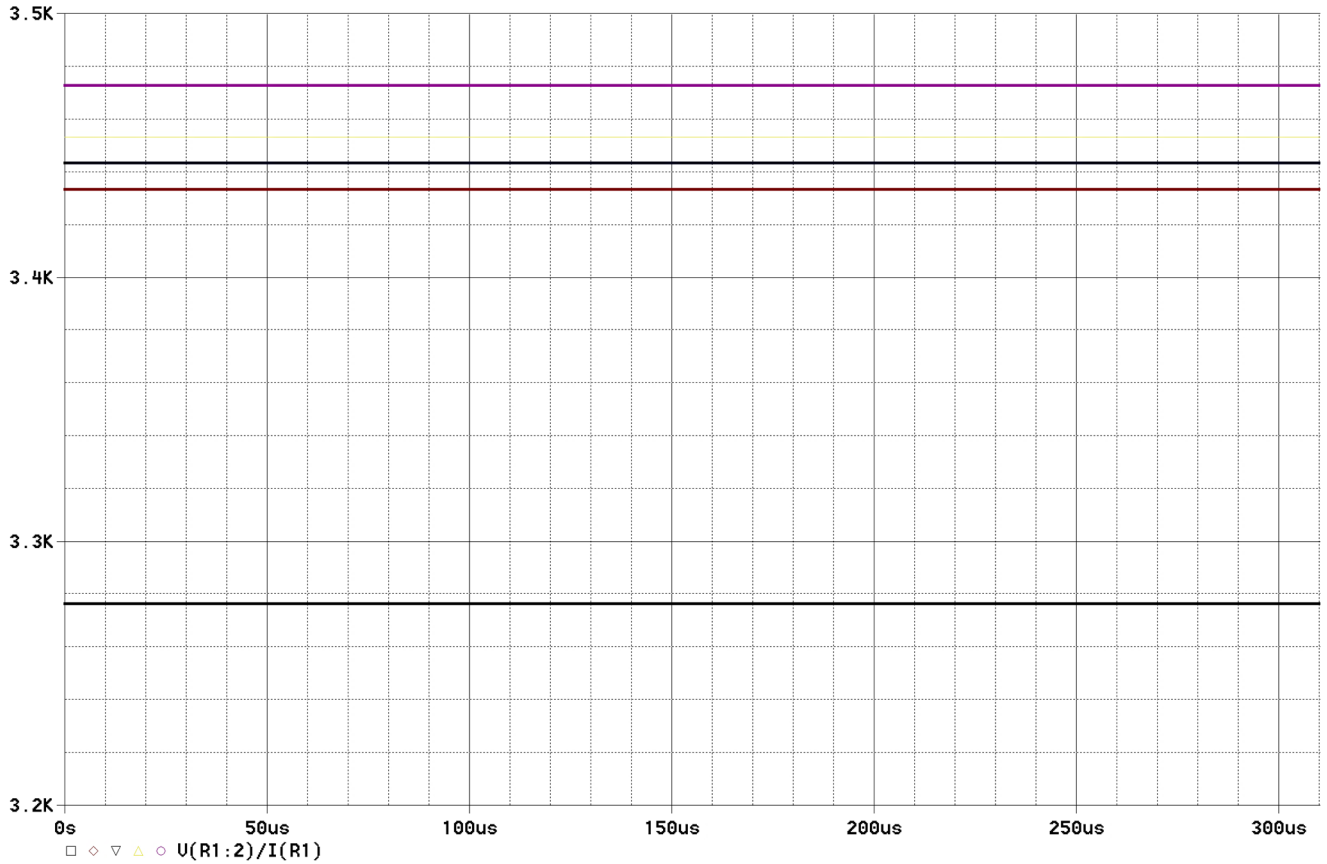


Figure 36 – PSPICE simulation showing piezoresistance for R1 at 20°C, 36°C, 37°C, 38°C, and 40°C.

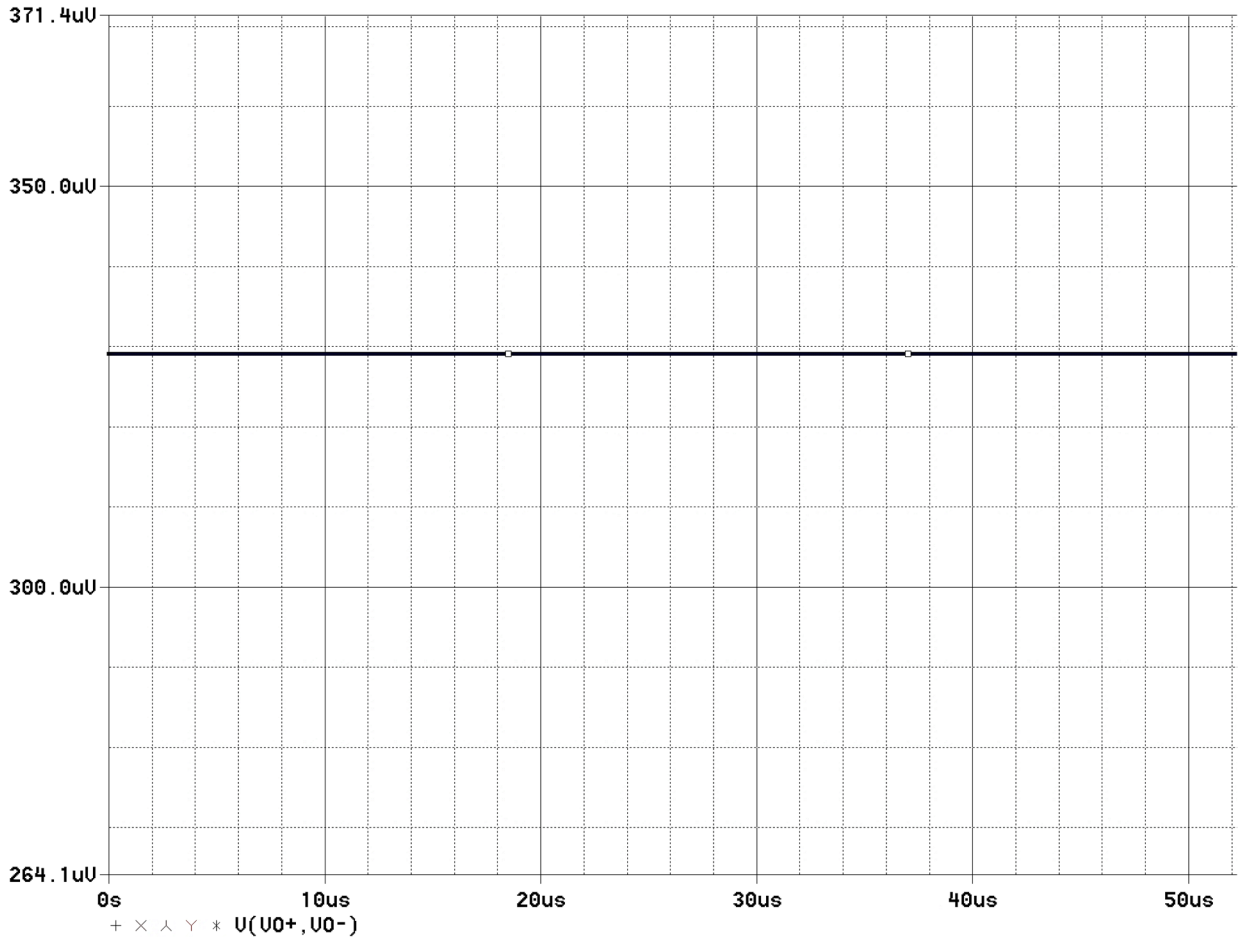


Figure 37 - PSPICE simulation showing bridge output of 329.076 µV for all temperatures 20°C - 40°C.

A noticeable offset voltage of 329 μV exists at the output, which is due to the piezoresistors' mismatch. Temperature variations, however, are almost entirely negated by the full-bridge circuit, resulting in only several femtovolts over the 20°C range. Provided the nominal resistance of each piezoresistor is close, the percent resistance change from nominal is negligible. Only in the presence of temperature gradients does the bridge become unbalanced due to temperature. However, temperature imbalances across the face of the die are unlikely due to the heat capacity of the contacting liquid media and the small cross-sectional area of the sensor.

A COMSOL simulation was created using the die and ceramic substrate geometry to evaluate temperature gradients within the sensor body and any impact upon the temperature of CSF. The simulation was constructed using 37°C water (99% CSF constituent) stimulating the bottom-side surface of the die. Joule heating resulting from the piezoresistors at 5V bias was simulated. Figure 38 shows the resulting temperature gradient in which the surface of the die and the contacting liquid is uniform at 37.248°C. At the chip's ceramic substrate, where the port meets the liquid column (or CSF), the temperature was found to be 37.018°C. Therefore, from both the PSPICE and COMSOL simulation, the device is both temperature stable and safe in-vivo with near zero heating impact to CSF.

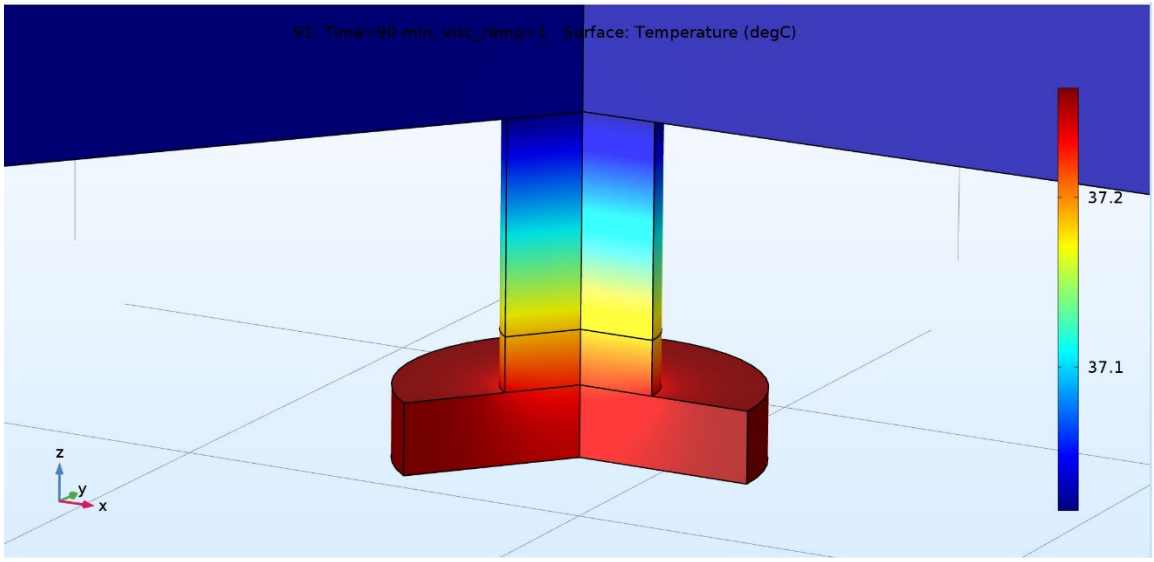


Figure 38 – Temperature gradient from sensor's Joule heating upon 37°C CSF.

Uncorrected Sensor Drift Results

The latest commercial technology available for drift-less pressure sensing was found offered by Amphenol/All Sensors employing dual matched-die cross-coupled sensors. The BLVR-L30D-B1NS sensor was selected for evaluation to assess the sensor's drift performance. Although the sensor module incorporates drift correction through the use of both cross-coupled fluid and cross-coupled electrical signals, the sensor is otherwise *un*corrected relative to this work's self-calibrating sensor system. By sharing input fluid under test with both sensors and electrically cross-coupling the outputs, the two sensors module can subtract out common-mode induced stress that could otherwise result in measurement drift. Amphenol is the only manufacturer identified by this research to specify long-term drift metrics, which for the BLVR in gaseous media is specified at 1.45 mm H_2O at year one. The sensor drift was evaluated for over two years using

the methods previously described in Chapter Three and with the laboratory setup shown in Figure 39. The laboratory setup utilized a Test Equity TEC1 temperature chamber set to 37°C. Measurements for room temperature, chamber temperature, and output voltage corresponding to pressure were logged with a one-minute period using National Instruments' LabView and the NI USB-6211 16-bit 250 kS/s data acquisition system.

The pressure sensor was amplified by a Texas Instruments INA-141 instrumentation amplifier, which was locally regulated by LM1086 and LM337 linear regulators. The sensor's readout circuit is shown in Figure 30. Local precision power regulation was utilized to minimize any bridge bias voltage effect upon drift. Power supply voltages and input fluid were routinely monitored to ensure stability for negligible to zero impact upon drift measurements. The entire system was further powered by an external Hewlett Packard E3620A precision power supply and an uninterruptable power system (UPS). The sensor module was configured with a glass cylinder epoxied to its ceramic printed circuit board (PCB) for backside die pressure stimulation as shown in Figure 40. Epoxy Technology EPO-TEK 730-110 was selected due to its use in other implantable devices. An initial transfer function was taken prior to long-term testing and is shown in Figure 41 revealing an amplified gain of 12.7 mV per mm H_2O (or 127 μV unamplified) and with an offset of 0.7 mm H_2O with excellent linearity of 0.60% full scale span (FSS).

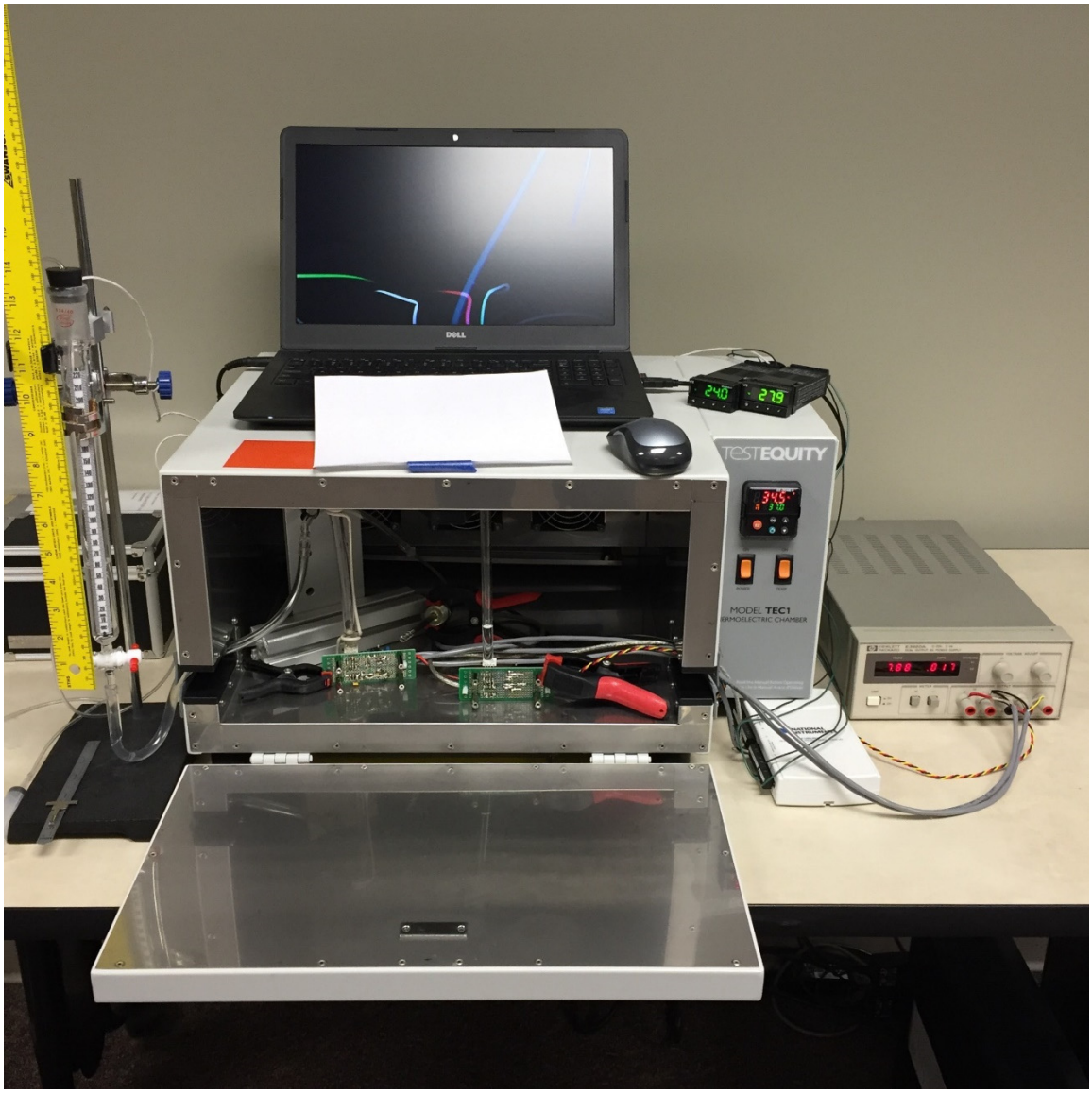


Figure 39 – Laboratory setup for uncorrected long-term drift measurement of cross-coupled sensor.

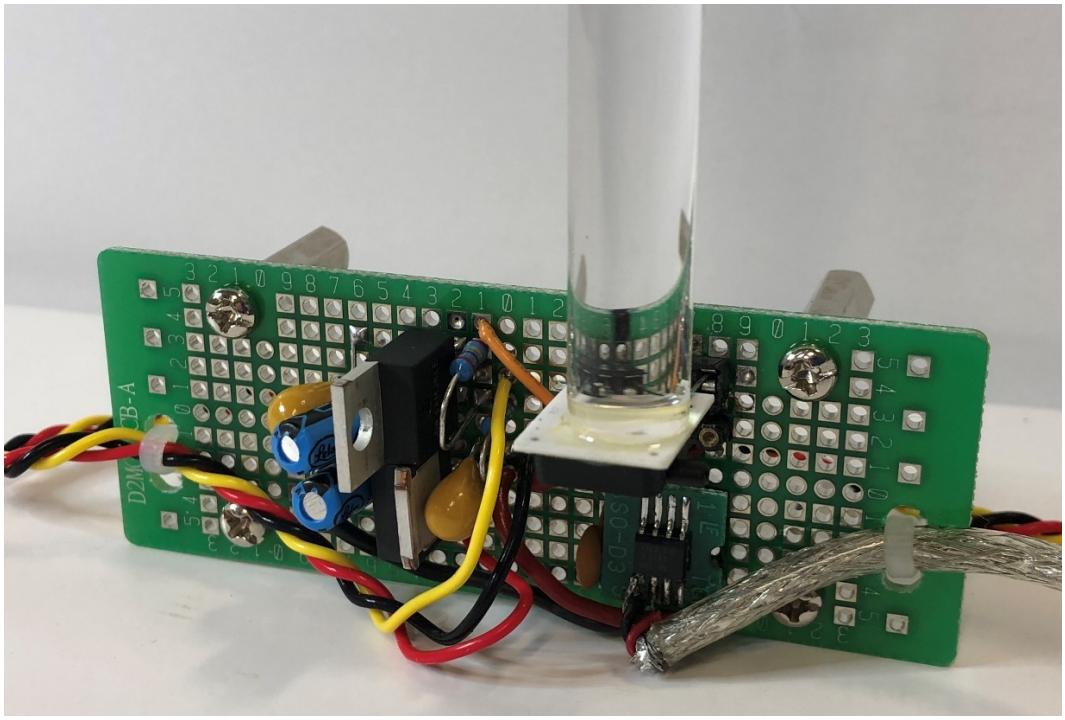


Figure 40 – Long-term test sensor with pressure cylinder and read-out circuit.

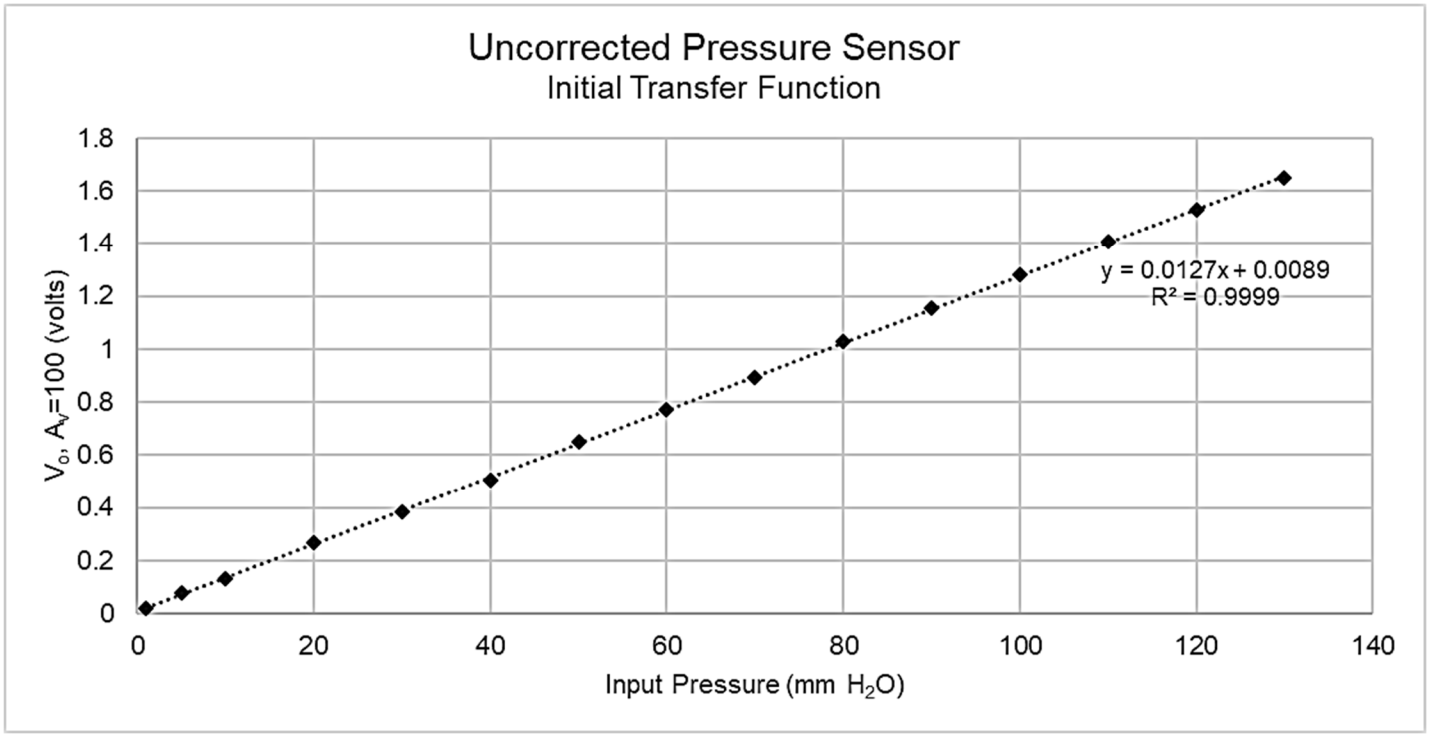


Figure 41 – Uncorrected pressure sensor initial transfer function.

Approximately 31 mm of water was used for pressurizing the system for long-term drift testing with a small top layer of mineral oil to mitigate evaporative effects within the thermal chamber. 31 mm H_2O was chosen as a moderate pressure, relative to the overall pressure range of the device, to challenge the sensor's signal-to-noise performance while yet minimizing any small parasitic pressure effects upon assessing true drift. Figure 42 graphs the average daily pressure output for 862 days of testing (i.e. 2.4 years).

By day 27, the pressure sensor's gauge factor lost 10% of its gain. A maximum occurred at day 841 with a loss of 19.4% gain. A slight anomaly at day 628 represents when the thermal chamber was re-setup due to a facility move. The liquid's top layer of mineral oil was slightly tilted wetting the upper surfaces of the cylinder's interior. A drop of liquid was added to compensate. However, the mineral oil slowly returned from the inner circumference of the cylinder settling upon the top of the water, overall resulting in a 0.9 mm H_2O increase in daily average pressure. The sensor's signal thereafter stabilized. However, over the next five months the sensor's output increased slightly before encountering another significant gain loss, returning to the approximate gain prior to the equipment move.

A linear fit overlaid on Figure 42 approximates a gross gain loss of 18.0% at day 862. A transfer function acquired shortly thereafter, at 2.5 years at 31 mm H_2O pressure stimulation, reveals a more precise 22% gain loss as shown in Figure 43. Nevertheless, linearity in the transfer function is nearly perfectly preserved at

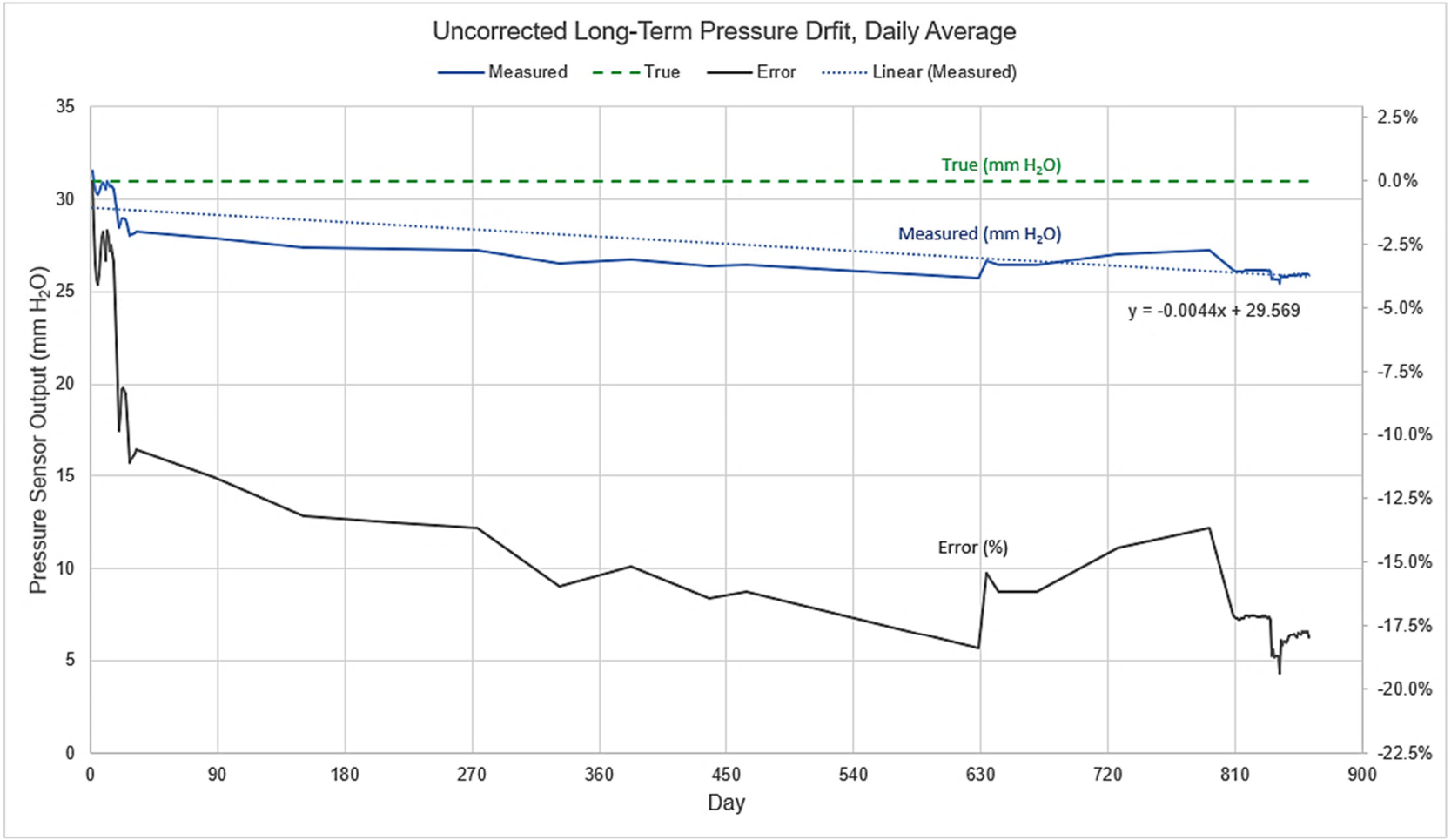


Figure 42 – Long-term uncorrected pressure sensor drift for 31 mm H_2O liquid (BLVR-L30D-B1NS).

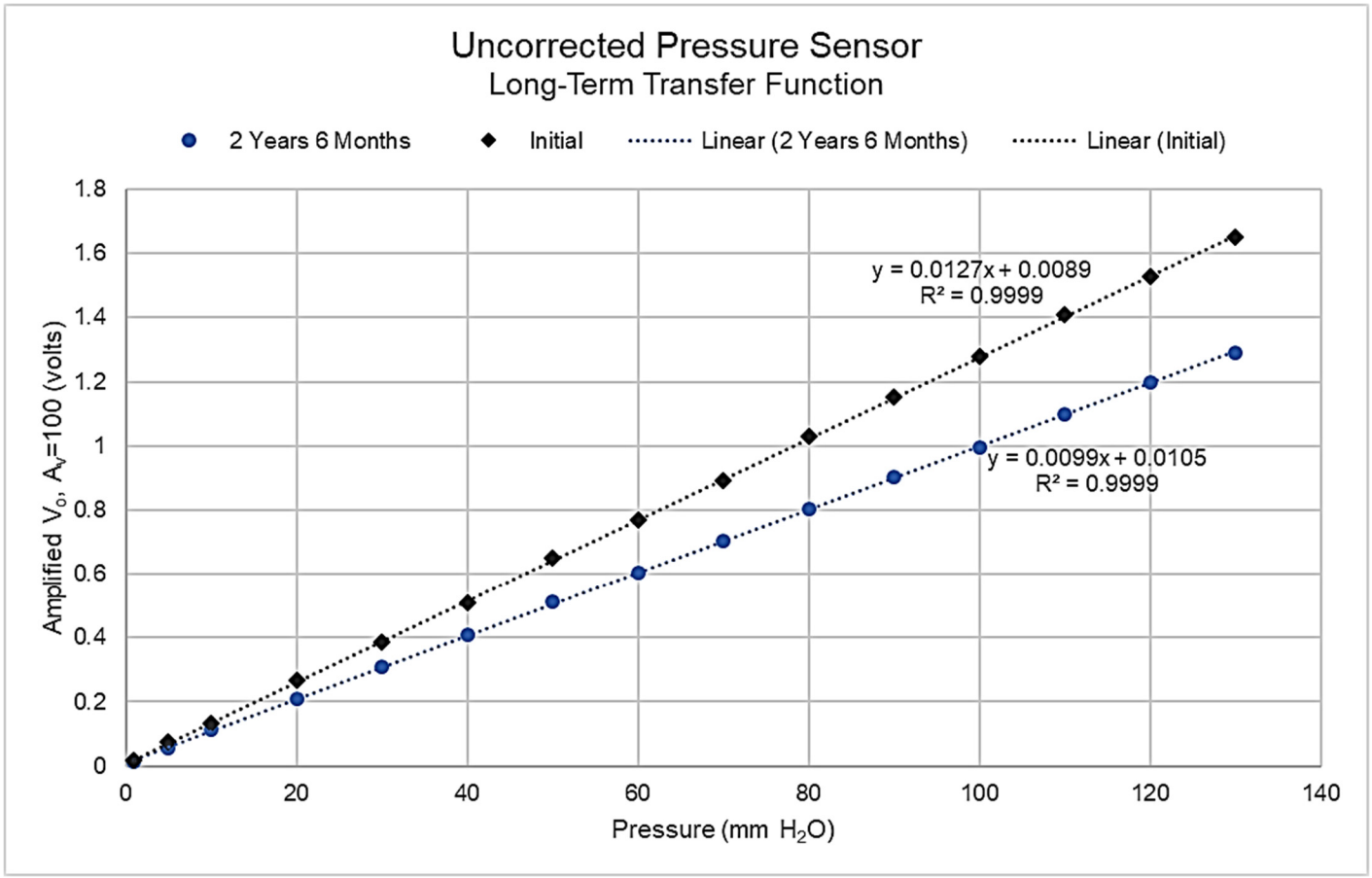


Figure 43 - Uncorrected pressure sensor initial and 2.5-year transfer function.

0.63% FSS (versus 0.60% originally) and with negligible zero shift with less than 1 mm H_2O. Figure 44 shows the transfer function for two additional matched sensor dies, which were used in fabricating a custom device. The figure shows an uncorrected transfer function after six months at room temperature. The data reveals an average decline in gain of 2.75% ±0.97%, with the difference *between* the two dies totaling 0.65%. Offset drift was negligible. Extrapolated to 2.5 years, the estimated gain drift, should it remain constant, would equate to about 14%. In this different set of dies, the linearity is again preserved despite the loss of gain. Linearity after six months was 0.74% FSS and 0.55% FSS for U1 and U2, respectively.

Three-month baseline and sensitivity studies performed by the University of Auckland, New Zealand, for a piezoresistive diaphragm pressure sensor, found thermal bonding damage as a prime suspect for die level drift. Additionally, the study identified diaphragm oxidation growth and the deterioration of its photo-resistive layer as a contributor to changes in gauge factor, or gain [130]. Other contributors included inelastic deformation of the diaphragm, effusion of the absolute reference cavity, power-cycling thermal effects, as well as drift mechanisms arising from DC bias. The preliminary study concluded that sensor drift was found to be bilateral and unpredictable, making a priori design compensation challenging. Esashi et. al. also studied specific drift factors in custom fabricated piezoresistive pressure sensors [117]. Their findings identified electrical leakage currents and thermal mismatch, particularly between the

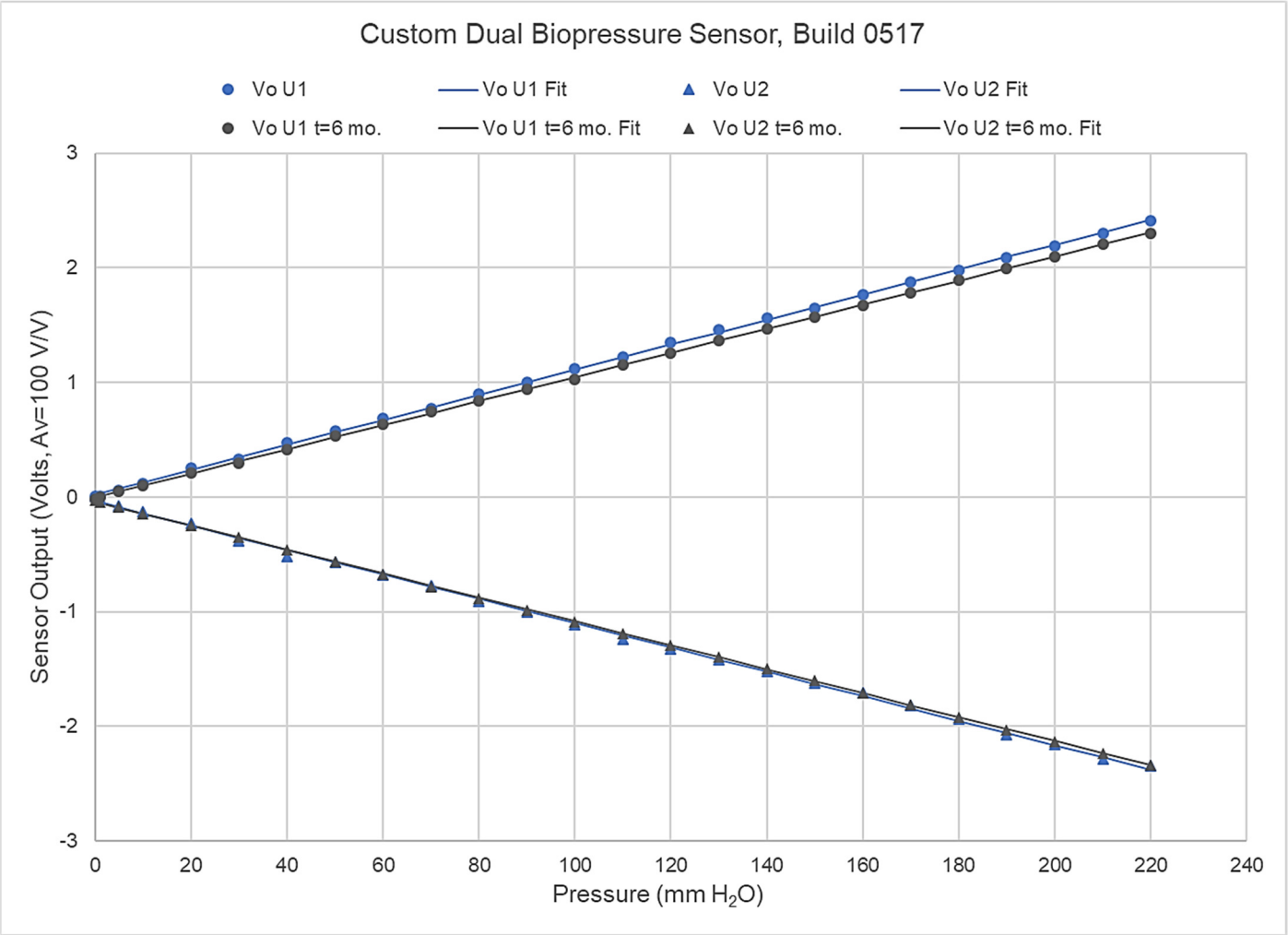


Figure 44 – Six-month drift results for dual pressure sensor build 0517

sensor and its support or substrate, to cause drift. The study stated most of the instabilities presented resulted from thermally induced stress upon packaging.

System Calibrated Sensor Results

Distinct from the Amphenol cross-coupled pressure inputs and summed electrical outputs, this research evaluated decoupled inputs and outputs utilizing a common absolute reference chamber with a second hydraulic reference and novel calibration approach intended for in-vivo operation. The approach utilizes matched silicon dies, as described in Chapter Three's Independent Dual-Die Dual-Reference BioPressure Sensor section, to evaluate gain and offset of one sensor to predict the characteristics of the other matched sensor. A custom pressure sensor module was constructed utilizing Amphenol's 30 INCH-D-MV matched pressure sensor dies. Figure 45 illustrates an exploded view of the custom sensor where on the left-hand side of the illustration is the absolute pressure chamber on top, which encapsulates the two top-side dies. At the top right-hand side of the figure is shown independent pressure port chambers for bottom-side stimulation of each die. The substrate in the middle upon which the pressure sensor dies are mounted is a 1 mm thick ceramic PCB. As compared to Figure 21, both dies share a top-side absolute pressure chamber source while each die's bottom-side diaphragms are interpedently stimulated.

The 30 INCH-D-MV dies are monocrystalline bulk micromachined silicon sensors of approximately 2 mm x 2 mm area with a mating silicon support structure. The

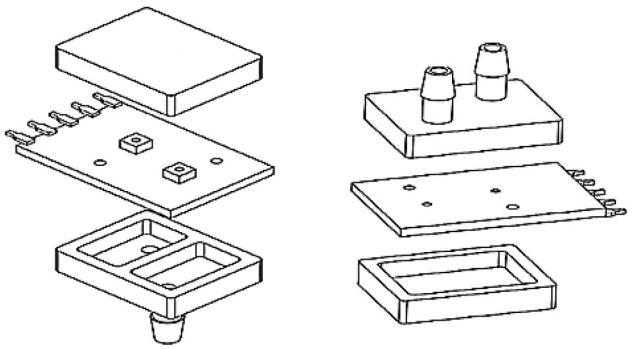


Figure 45 – Custom dual biopressure sensor exploded illustration.

dies are mounted bottom-side to their ceramic chip carrier via a low stress deep, yet thin, layer of silicone. Single crystal silicon is the most commonly used substrate for micromachined MEMS and has a long history of use in implantable devices, including ICP monitors, such as the Codman Microsensor®, as well as the NEUROVENT P-tel® and the Sensor Reservoir®. Kotzar at. al. examined the biocompatibility of silicon MEMS, along with commonly associated materials, such as titanium, over a range of ISO 10993 tests [131]. Titanium has long been used in pacemakers providing hermetic enclosures incorporating glass-to-metal seals [132]. Hermetic anodic bonding of bulk micromachined silicon pressure sensors to glass has additionally been reported and demonstrated [91]. Corning 7740 (Pyrex®), Corning 7070, Corning 1729, Corning 9626, Schott 8330 (Tempax®) and SD-2 (HOYA) are all among the most prominent glass materials given their close thermal coefficients to silicon [133]. Glass to metal seals' biocompatibility has been examined to be robust [134]. Kotzar examined both aqueous and non-aqueous physiochemical tests, cytotoxicity, extractables, and

histopathology for explanted silicon and associated MEMS materials as well as titanium materials. Kotzar further examined the test materials both post-sterilization and explantation for in-vivo damage or alteration under scanning electron microscopy (SEM). All tests results indicated safe biocompatibility, including compatibility with prevailing sterilization techniques, such as gamma and autoclaving, without damage to the materials. Silicone elastomer materials have additionally proven a long history of biocompatibility, particularly in the brain, where its first recorded CNS use dates back to the 1950's by Robert Pudenz and Richard Ames for use as long-term shunt catheters [135]. All considered, the selection of the 30 INCH-D-MV die and associated materials, or the additional choice of mating materials which may be used in the fabrication of the finished implant, represent biocompatible materials with hermetic capabilities, meeting the requirements of R1.0 and following objectives.

The 30 INCH-D-MV dies provide ±762 mm H_2O of linear pressure range with a proof pressure (i.e. maximum applied pressure without permanently changing performance) of ±5,080 mm H_2O (i.e. ±one-half atmosphere). Burst pressure of the 30 INCH-D-MV die occurs at ±2.0 atmospheres. The 30 INCH-D-MV sensor die outputs were mounted upon a ceramic substrate and independently bonded and pinned out to a secondary printed circuit board, as shown in Figure 46.

Custom pressure sensor chambers were fabricated, as shown in Figure 45, from Polymethyl Methacrylate (PMMA) for laboratory evaluation purposes. The top-

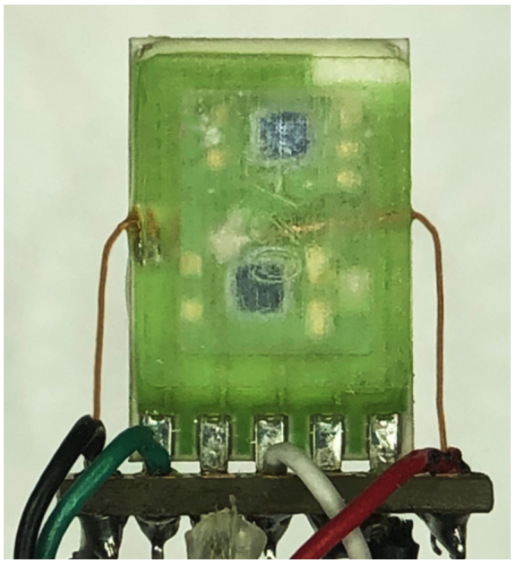


Figure 46 – Custom dual matched die biopressure sensor prototype showing absolute reference chamber and top-side dies therein.

side chamber, as shown in Figure 46, provides a rigid absolute pressure chamber, common to both dies, while another set of separate chambers provide independent pressure ports for each bottom-side die, consistent with Figure 21. Figure 47 shows one of the finished custom pressure sensors configured for laboratory evaluation, identified as Build 0517, with an absolute pressure chamber of approximately 28.92” Hg (9,987 mm H_2O).

For operation, both of the sensors were biased at +5 VDC producing a nominal zero pressure output of +2.5V. The output signals were amplified using an Analog Devices AD8222 instrumentation amplifier for reasons described in the Electronics Readout Overview section. The AD8222 was biased at ±10 VDC whereby the nominal output voltage was zero for zero input pressure. Backside die pressure produced a negative going signal in each sensor. However, the U1 output was measured positively with respect to the common mode point and U2 was measured negatively. Figure 48 shows a schematic of the front-end readout circuitry used in laboratory measurements. Figure 49 shows the recorded transfer function for the custom dual sensor build resulting from independent backside die stimulation. Gain of U1, determined from the best-fit straight line, was 10.92 mV/mm H_2O while U2 was 10.64 mV/mm H_2O. Linearity was found to be 1.03% and 2.36% FSS, respectively. Zero offset for U1 was 1.65 mm H_2O and 3.41 mm H_2O for U2.

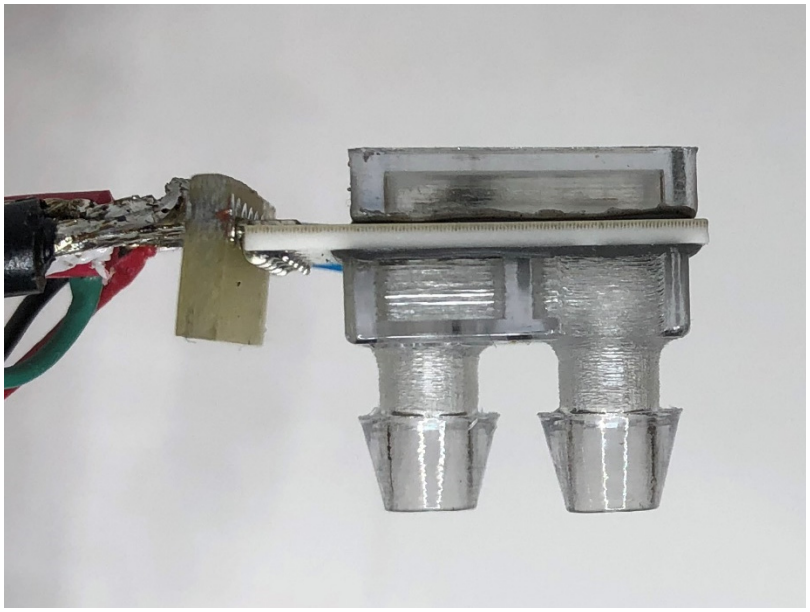


Figure 47 - Custom dual matched die biopressure sensor prototype showing both independent chambers and top-side reference chamber.

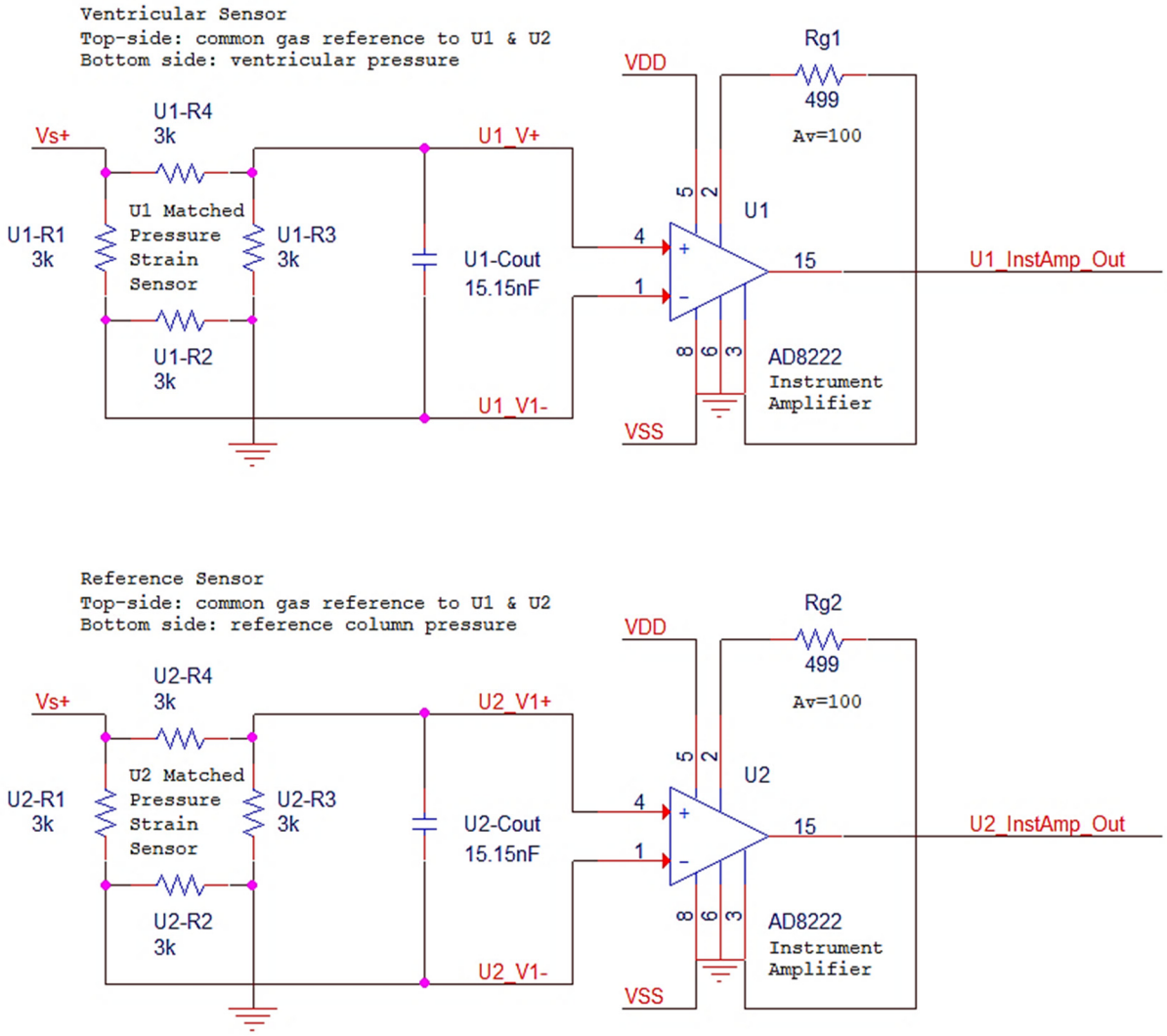


Figure 48 – Custom dual matched-die sensor readout circuit.

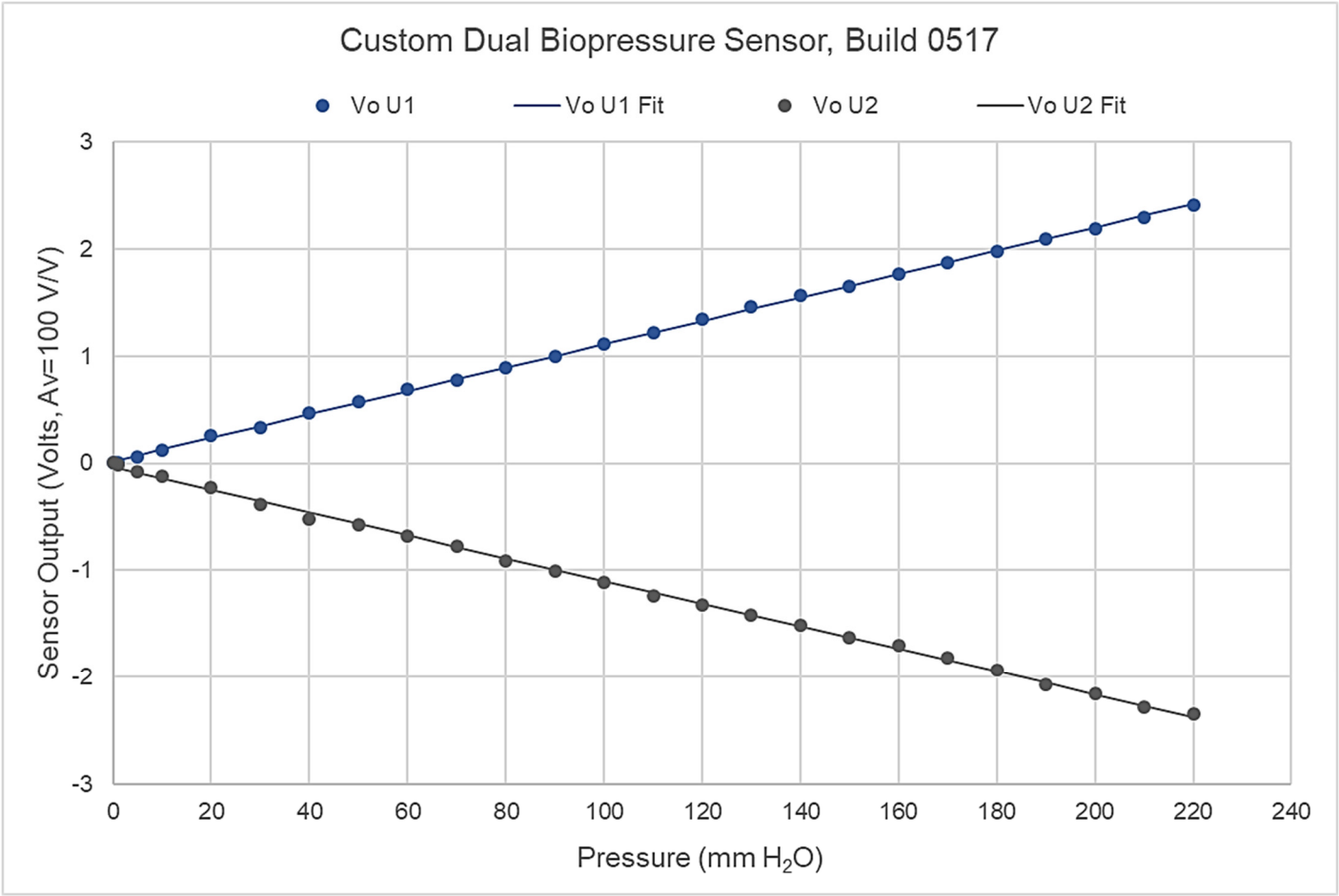


Figure 49 – Custom dual biopressure sensor transfer function (Build 0517).

The sensor die's pressure range of ±500 mm H_2O was confirmed in the custom module, as shown in Table 5, with an absolute error of less than 1%. Figure 50 shows the acquired signal for +502 mm H_2O revealing a standard deviation from mean level for n=100 samples of 0.69 mm H_2O. Likewise, Figure 51 shows the acquired signal for -499 mm H_2O with a similar standard deviation of only 0.72 mm H_2O. Overall, the measured pressure range satisfies objective O3.1.

Table 6 tabulates resolution measurements for both dies given 3σ noise levels. Noise levels were observed to increase with pressure until a plateau occurred around 150 mm H_2O. Overall, the 3σ resolution was 3.0 mm H_2O for U1 and 3.4 mm H_2O for U2, meeting the objective set forth in O3.2 of less than 10 mm H_2O. The limit of detection (LOD) was found from the noise at 0 mm H_2O to be 2.3 mm H_2O for U1 and 3.3 mm H_2O for U2. For levels above 200 mm H_2O, the data, including that from full range testing and Table 6, reveals resolutions of approximately one percent or better.

For repeated accuracy measurements, including the measurement of both trueness and precision, 150 mm H_2O was selected for assessment since it produced the worst noise figures over the sensor's range (see Table 6). Table 7 provides accuracy statistics for n=100 samples while Figure 52 and Figure 53 show samples of measured signals. A maximum mean error of -3.73 mm H_2O between the two sensors was measured with U1. However, the error measured was within the objectives of O3.3, or ±5 mmH_2O.

Table 5 – Sensor Pressure Range Verification

	Vrms	Vrms Offset	Gain mV/ mm H_2O	Measured Pressure mm H_2O	Actual Pressure mm H_2O	Error mm H_2O	Error %
+500 mm H_2O	5.37	-0.0221	10.64	506.78	502	4.78	0.95%
-500 mm H_2O	-5.38	-0.0221	10.64	-503.56	-499	-4.56	0.91%

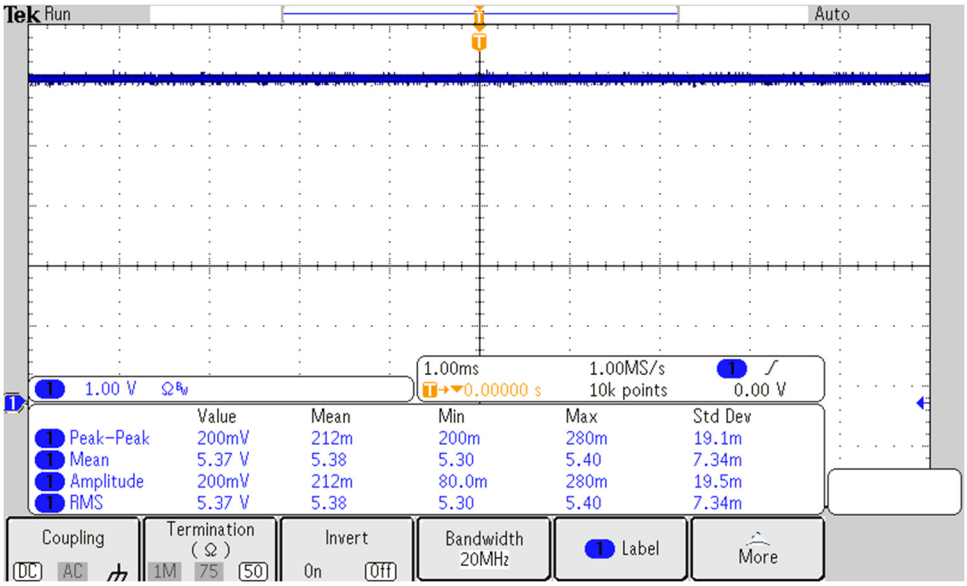


Figure 50 - +502 mm H_2O signal

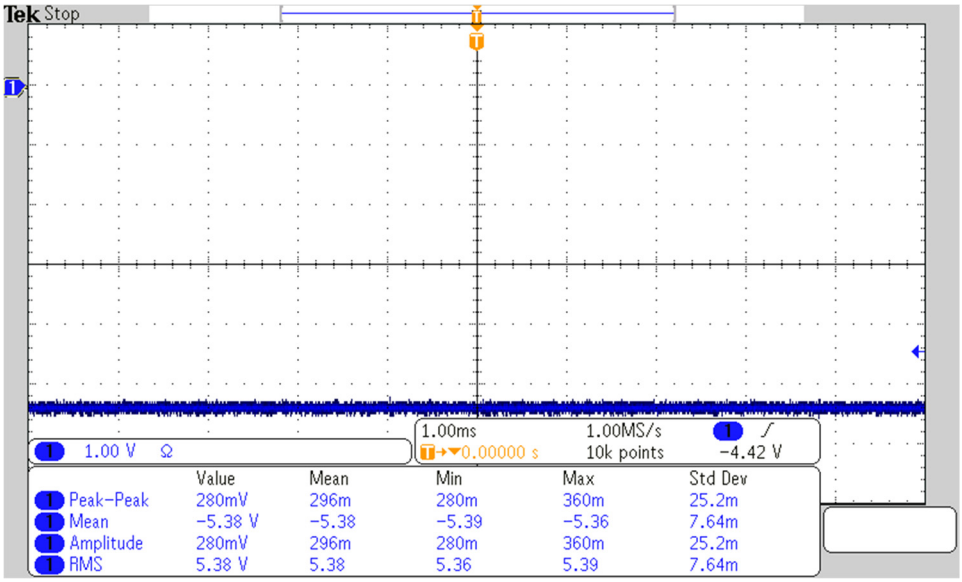


Figure 51 - -499 mm H_2O signal

Table 6 – Sensor resolution summary

	Pressure mm H_2O	Noise, σ mV	3σ mV	3σ mm H_2O	Average Resolution mm H_2O
U1	0	8.1	24.3	2.3	3.0
	100	7.7	23.2	2.2	
	150	13.5	40.5	3.9	
	300	13.2	39.7	3.8	
U2	0	11.5	34.5	3.3	3.4
	100	8.1	24.3	2.3	
	150	16.3	48.9	4.7	
	300	12.0	36.1	3.5	

Table 7 – Accuracy measurements for sensors U1 and U2, n=100

	Vrms	Vrms Offset	Gain mV/ mm H_2O	Measured Pressure mm H_2O	Actual Pressure mm H_2O	Error mm H_2O	Error %	σ Vrms	3σ mm H_2O
U1 150 mm H_2O	1.59	-0.008	0.010925	146.27	150	-3.73	-2.48%	0.00105	0.29
U2 150 mm H_2O	-1.57	-0.005	-0.01064	147.10	150	-2.90	-1.93%	0.00365	-1.03

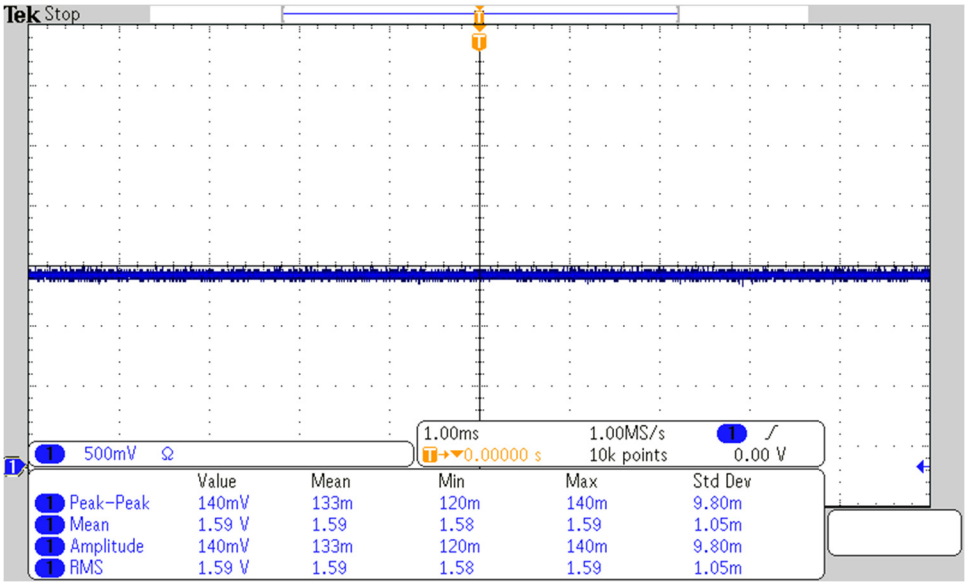


Figure 52 – Accuracy measurement for sensor U1, 150 mm H2O, n=100 samples

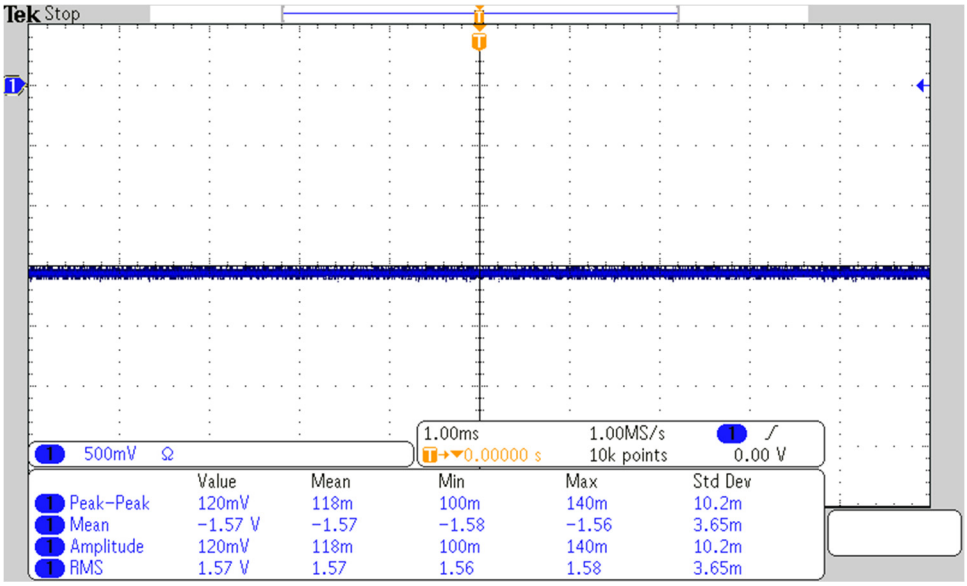


Figure 53 - Accuracy measurement for sensor U2, 150 mm H_2O, n=100 samples

Manual power cycle tests were performed for 150 mm H_2O to measure reproducibility, or precision. Figure 54 shows the resulting histogram of 100 samples revealing a mean pressure of 151.29 mm H_2O. The standard deviation was 0.387 mm H_2O with 3σ equaling 1.16 mm H_2O. The range was 1.8 mm H_2O and the mean absolute error was 1.29 mm H_2O. The reproducibility assessment meets the precision objective of ±5 mm H_2O of O3.4. Given the maximum error for the worst noise figures measured over the range, the combined trueness and 3σ reproducibility results in an accuracy of 4.89 mm H_2O. For pressures beyond 200 mm H_2O, including 500 mm H_2O, a maximum error of 3.8 mm H_2O was found with U1 at 300 mm H_2O, or 1.26%, well within the objective of O3.5.

To explore the dual matched dies' capability to mitigate gain and offset drift with the system calibration described in Chapter Three, the sensors' bridge bias and common mode pressure was modulated. Bridge bias was adjusted from 80% to 100% (5 VDC) to 120% to induce sensor gain shifts of ±20%.

Figure 55 shows the resulting pressure-voltage transfer functions for the new custom dual-die pressure sensor module. Both of the sensors' gain response was measured with a maximum gain difference between the two matched sensors of +0.65% and -0.3% over the full range of 80% to 120% gain shift.

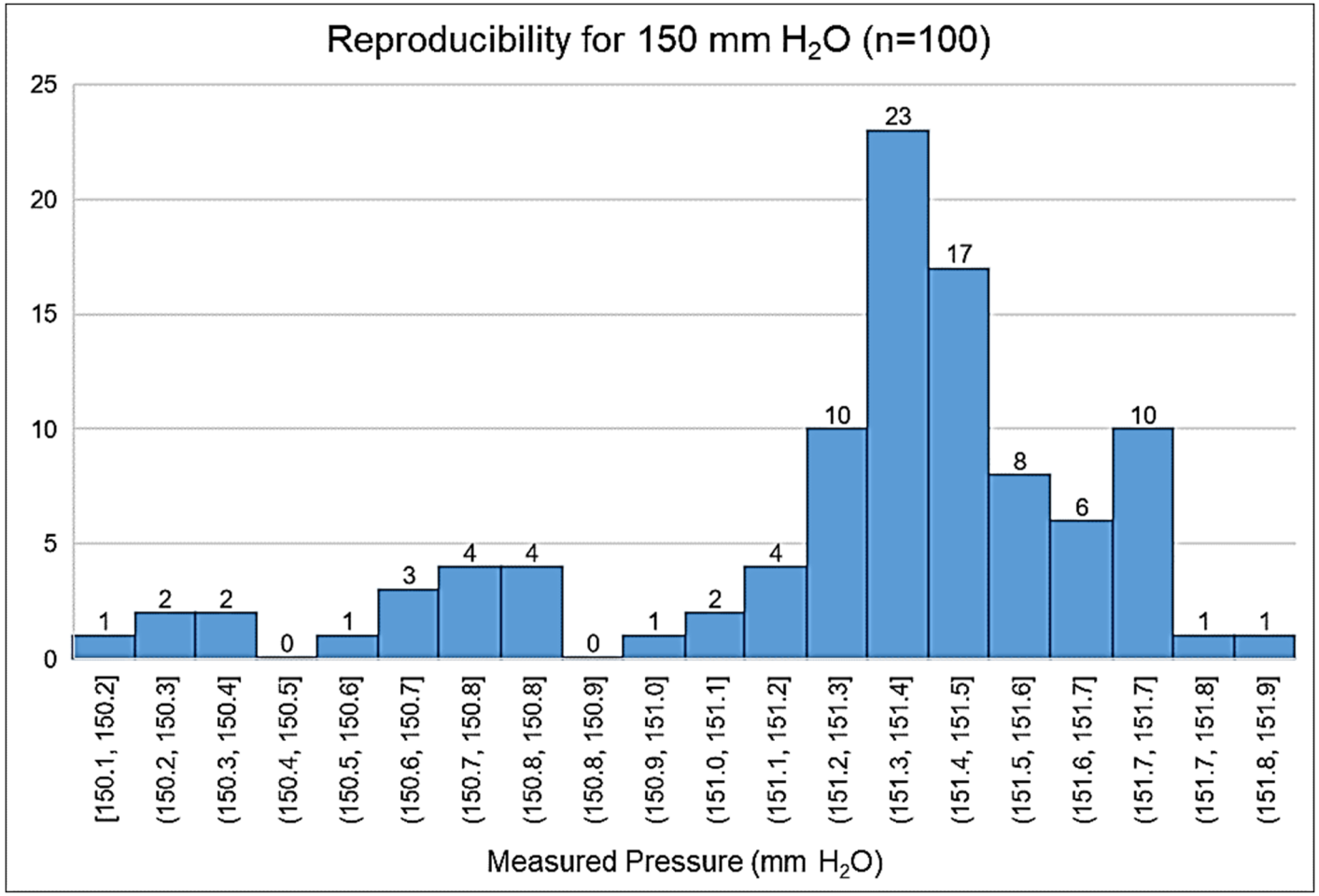


Figure 54 – Precision measurement histogram for 150 mm H_2O and n = 100

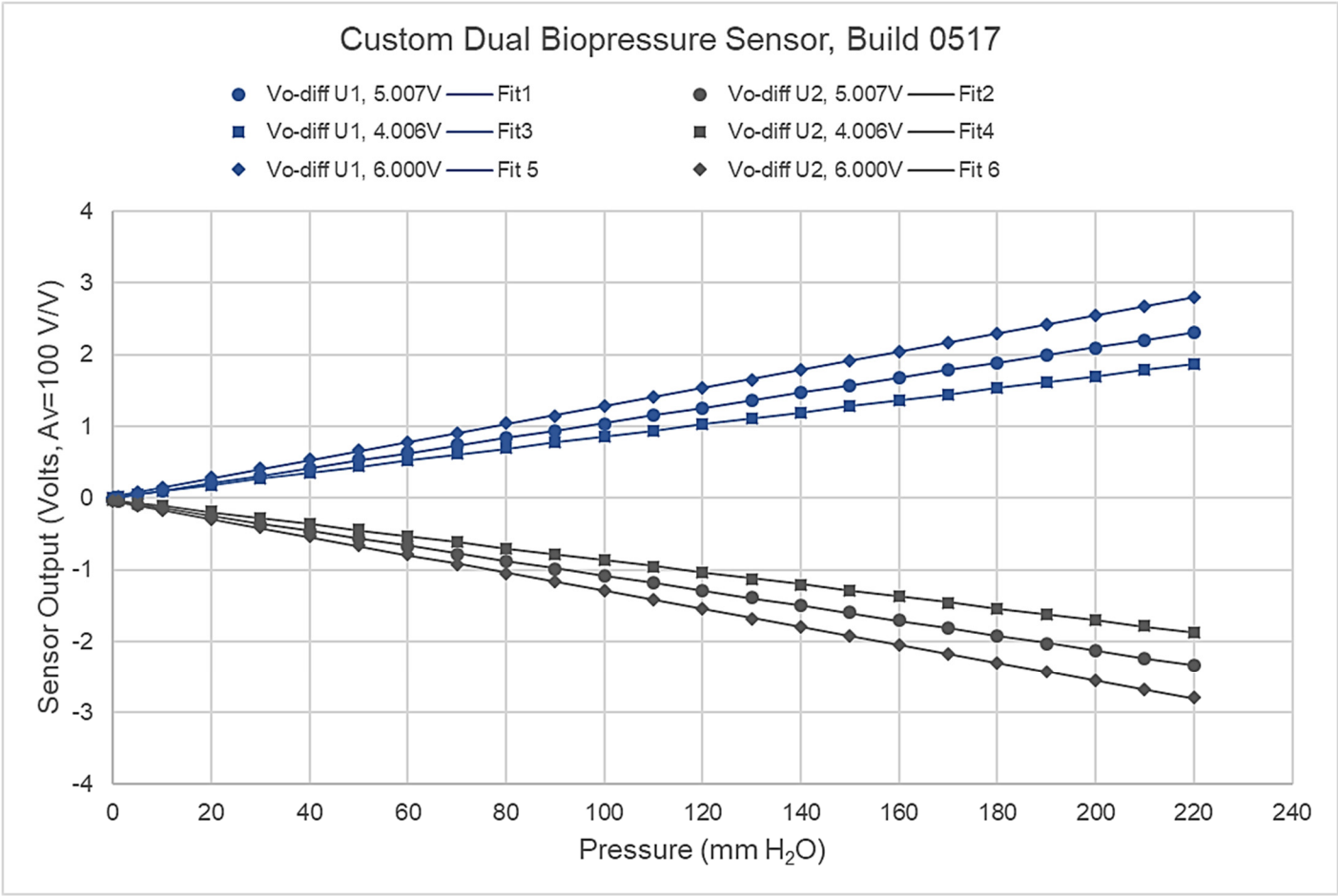


Figure 55 - Dual sensor die comparison for 80%, 100%, and 120% gain.

A hydraulic and pneumatic test system was setup according to that described in Chapter Three. The laboratory setup is shown in Figure 56, Figure 57, and Figure 58. The test system was designed to assess the custom dual matched die system's performance under induced gain and offset shift. Figure 56 shows the test and measurement system, including a graduated burette simulating a ventricular pressure source. Figure 57 shows the reference fluid column and 2L water reservoir simulating the peritoneum. Figure 58 is the test setup's vacuum pressure chamber used for inducing an offset pressure relative to the sensor's integrated absolute pressure chamber. An enclosed input pressure source consisting of a drying tube simulated ventricular pressure.

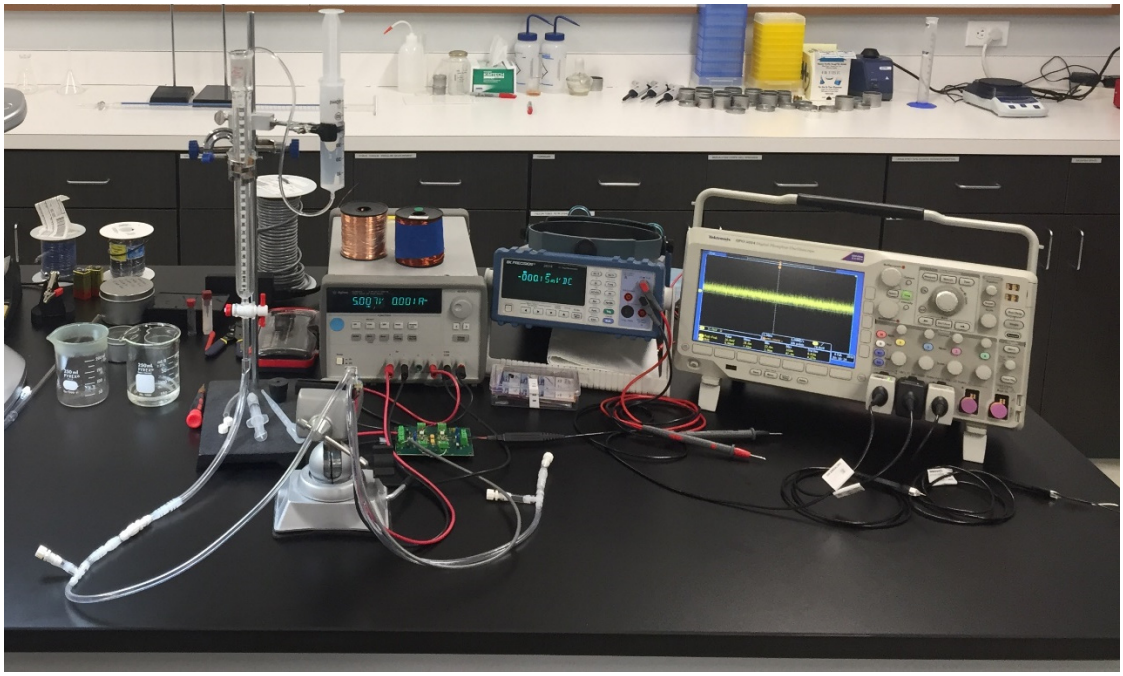


Figure 56 – Custom dual biopressure sensor system test bench.

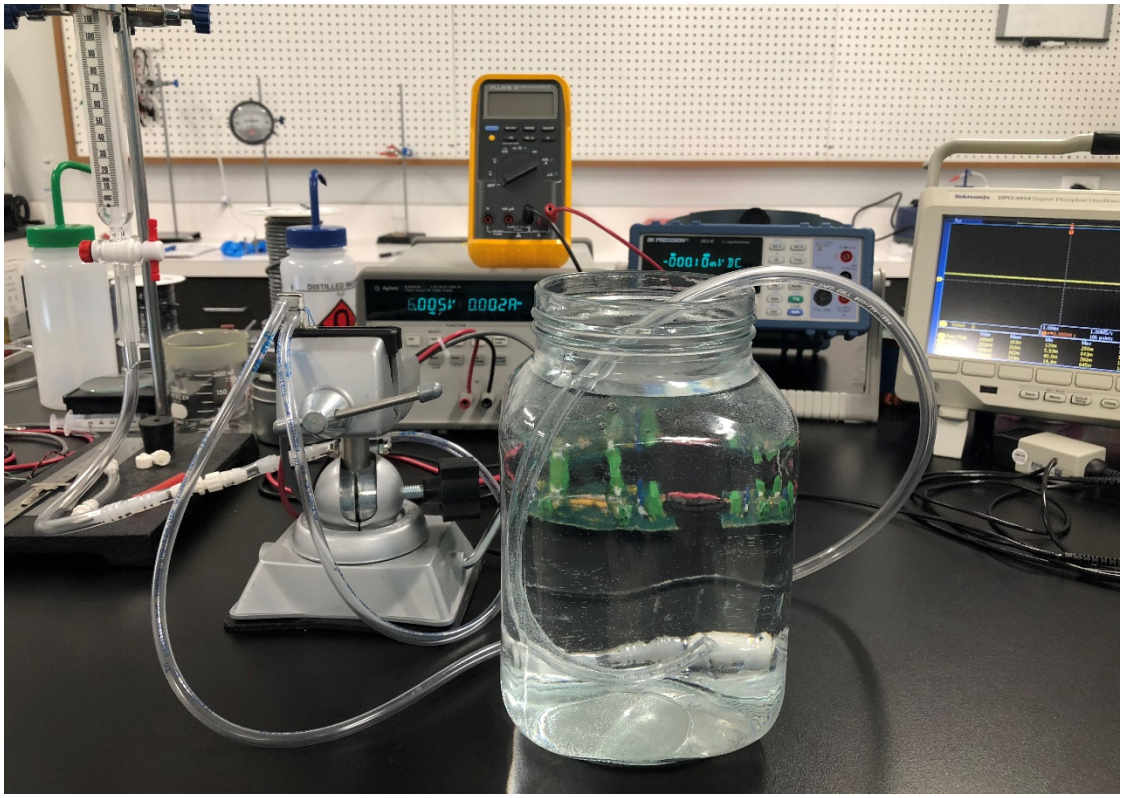


Figure 57 – Reference reservoir for liquid fluid column.

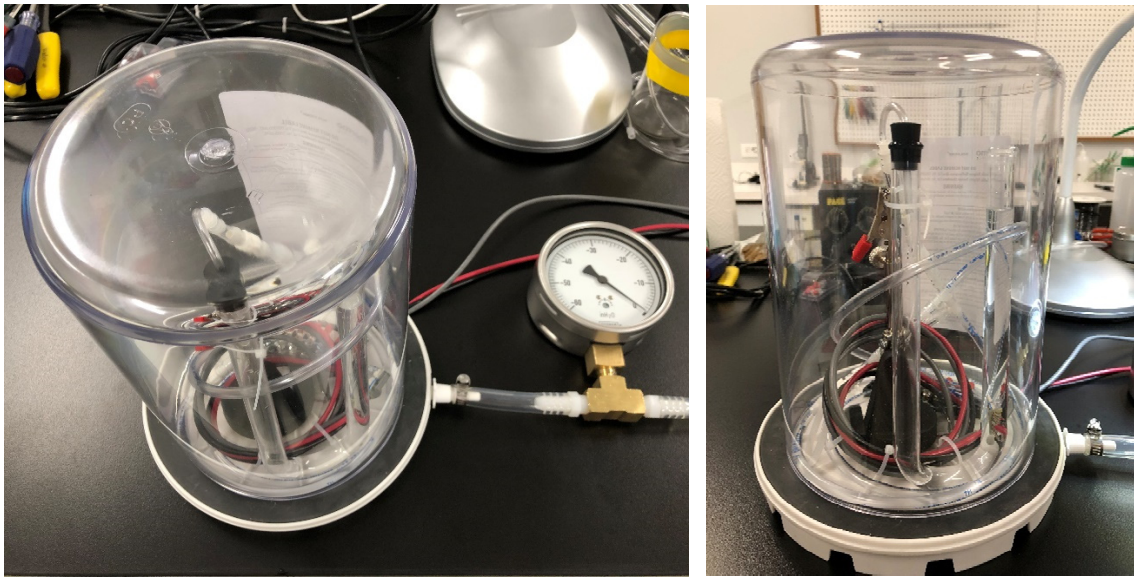


Figure 58 - Isolation pressure chamber with self-contained pressure source.

The new dual matched-die pressure sensor module was subjected to gain drifts of +20% and -20% to evaluate the system's ability to accurately negate the error. Barometric pressure (i.e. station pressure) at the time of testing was 29.138" Hg (10,062 mm H_2O), representing an offset of 75 mm H_2O (10,062 barometric less the integrated absolute chamber's pressure of 9,987 mm H_2O). The sensor module's reference fluid column was approximately 445 mm in length and the height of the reservoir was measured upon each positioning from 0° to -90°. Table 8 outlines the results of the custom sensor's self-calibration utilizing its reference fluid column.

For measurement series one, for example, an input stimulus of 100 mm H_2O (above barometric) was used to simulate ventricular pressure. A gain deficit of -20% was induced for the test. A 440 mm reference fluid column was connected to one of the two sensor dies (i.e. the reference die). For a patient deployment, the reference column length would be recorded upon implant. The system was then operated in calibration mode as if it were in-vivo. Signal measurements were taken by placing the reference column in both the 0° and -90° positions, as recorded in Table 8. The gain was then derived from single-ended measurements of the reference die, as follows:

$$A_{v-ref} = \frac{-0.449 - (-4.110)\,V}{-440\ mm\ H_2O} = 0.008320455\,\frac{V}{mm\ H_2O}$$

Next, the offset was calculated, based on the gain, using slope-intercept form. Barometric pressure was measured using the iPhone® Bosch BMP-280,

Table 8 – System calibrated dual matched-die sensor results at gain ±20%

Known Test Parameters	Measurement Series 1	2	3	4	5	6
Sensor Bridge Bias (V):	4.00	5.00	6.00	4.00	5.00	6.00
Sensor Bridge Bias (%):	80%	100%	120%	80%	100%	120%
CSF Test Pressure (mm H_2O):	100	100	100	150	150	150
Barometric Pressure (mm H_2O):	10,033	10,039	10,038	10,038	10,038	10,038
Ref. Column Pressure (mm H_2O):	-440	-444	-443	-444	-445	-445
0º Position Signals						
CSF (Vrms):	0.385	0.621	0.481	0.769	0.968	1.390
Ref (Vrms):	-0.449	-0.428	-0.799	-0.478	-0.611	-0.517
-90º Position Signals						
CSF (Vrms):	0.457	0.597	0.535	0.848	1.090	1.310
Ref (Vrms):	-4.110	-5.180	-6.390	-4.210	-5.260	-6.280
Derived Gain and Offset						
Measured Gain (V/mm H_2O):	-0.0083	-0.0107	-0.0126	-0.0084	-0.0104	-0.0130
Measured Gain (from nominal):	78%	--	118%	80%	--	124%
Offset (V):	83.03	107.02	125.89	83.90	104.26	129.48
CSF Pressure (mm H_2O):	100.2	98.0	101.4	148.4	151.1	147.3
Error:	0.23%	-1.99%	1.42%	-1.10%	0.76%	-1.83%

providing a specified 0.10 mm H_2O resolution and typical accuracy of 1.22 mm H_2O [136]. In a patient setting, the barometric pressure would be read ex-vivo and equated to the reference die's pressure reading in the supine, or 0° position, whereby the column pressure would be approximately zero.

$$b = -0.449\,V - 10{,}033\,mm\,H_2O * (-0.0083205\frac{V}{mm\,H_2O}) = 83.03\,V$$

Finally, with the gain and offset derived from using the sensor system's reference fluid column and externally measured barometric pressure, the ventricular pressure may be determined. The gain and offset values for the reference sensor can be applied to the ventricular pressure sensor, by virtue of matched dies, and intracranial pressure calculated as follows:

$$P_{CSF} = abs\left(\frac{0.385\,V - 83.03}{-0.008320455\frac{V}{mm\,H_2O}} - 10{,}033\,mm\,H_2O\right) = 100.2\,mm\,H_2O$$

The absolute value is taken due to the negative going signals arising from bottom side die stimulation. As can be seen from this measurement series, the actual versus derived CSF pressure resulted in an error of only 0.23% for a -20% gain drift and a 75 mm H_2O offset. Measurements were taken for ±20% induced gain drifts with the same 75 mm H_2O offset for both 100 and 150 mm H_2O simulated ventricular pressure. All measurements were within 2% of actual input pressure.

Table 9 provides the results of further inducing an offset using the

Table 9 - System calibrated dual matched-die sensor results for induced offset

Known Test Parameters	Measure-ment #1	Measure-ment #2
Sensor Bridge Bias (V):	5.00	5.00
Sensor Bridge Bias (%):	100%	100%
CSF Test Pressure (mm H_2O):	150	150
Barometric Pressure (mm H_2O):	10061	9810
Ref. Column Pressure (mm H_2O):	-254	-254
0º Position Signals		
CSF (Vrms):	0.805	-1.45
Ref (Vrms):	-0.791	-3.07
-90º Position Signals		
CSF (Vrms):	0.791	--
Ref (Vrms):	-3.491	--
Derived Gain and Offset		
Measured Gain (V/mm H_2O):	-0.01063	-0.01063
Offset (V):	106.16	101.21
CSF Pressure (mm H_2O):	150.14	152.40
Error:	0.09%	1.60%

isolation/vacuum pressure chamber shown in Figure 58. A simulated ventricular pressure of 150 mm H_2O was used in both measurements. Measurement 1 was taken outside the chamber to facilitate gain determination using the two different reference column positions. The calculated gain and offset at normal barometric pressure resulted in a CSF calculation of 150.14 mm H_2O, almost precisely the known true input. Measurement 2 was taken thereafter entirely within the pressure chamber at a reduced environmental pressure of -9.9" H_2O (i.e. -251 mm H_2O) as shown in Figure 59. This resulted in an absolute environmental pressure of 9,810 mm H_2O. For Measurement 2, the system's reference column line was flat against the bottom of the chamber, representing the 0° position and then the new offset was calculated. 90° signal measurements within the chamber were not necessary, or feasible, as the gain was determined outside the chamber. As can be seen from the table, the 150 mm H_2O pressure voltage shifted from +0.805 V to -1.45 V due to the environmental change. The derived offset shifted from 106.16 to 101.21. Combined, the CSF pressure derived for Measurement 2 within the chamber was 152.40 mm H_2O, representing only a 1.60% error. The test demonstrates the ability of the sensor system to correct large baseline shifts. Without the offset correction, the resulting error would have been over 100%.

Figure 60, Figure 61, and Figure 62 graph the test results of the system calibrated custom biopressure sensor. For 150 mm H_2O and either a gain of ±20% or offset of approximately 250 mm H_2O, the maximum error from true



Figure 59 – Vacuum pressure chamber measurement

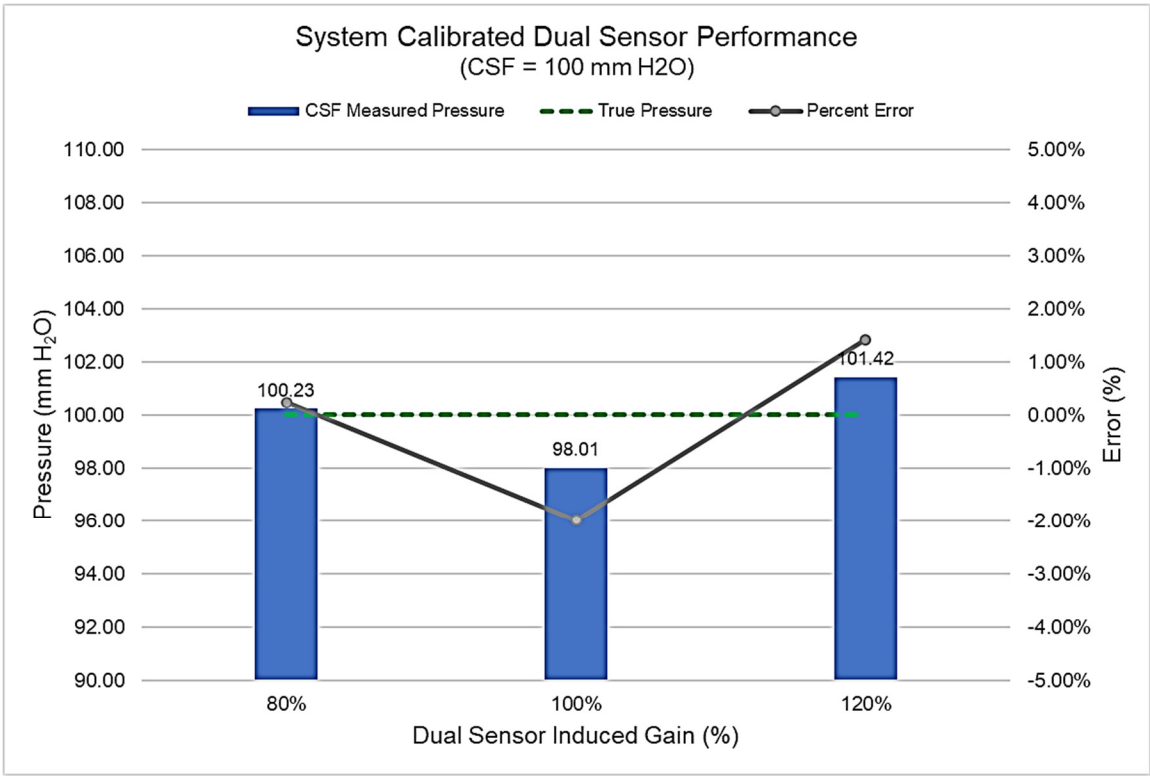


Figure 60 – System calibrated dual sensor performance for 100 mm H_2O and induced gain shift.

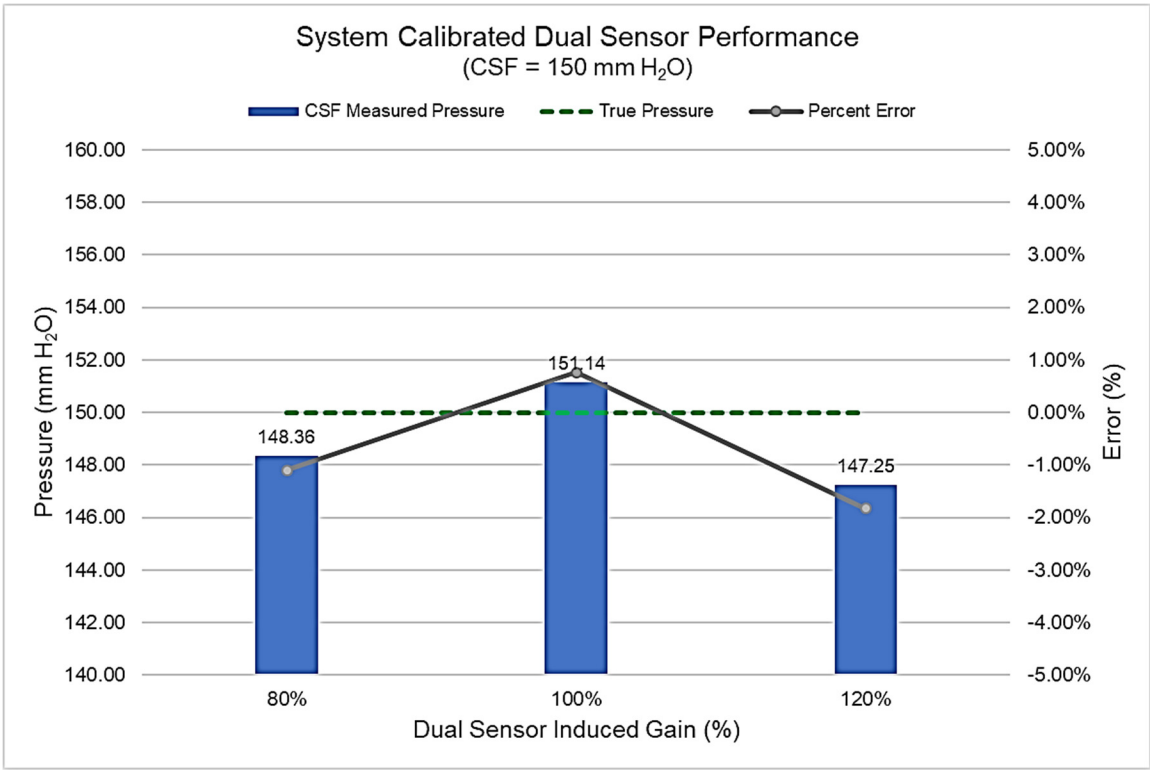


Figure 61 - System calibrated dual sensor performance for 150 mm H_2O and induced gain shift.

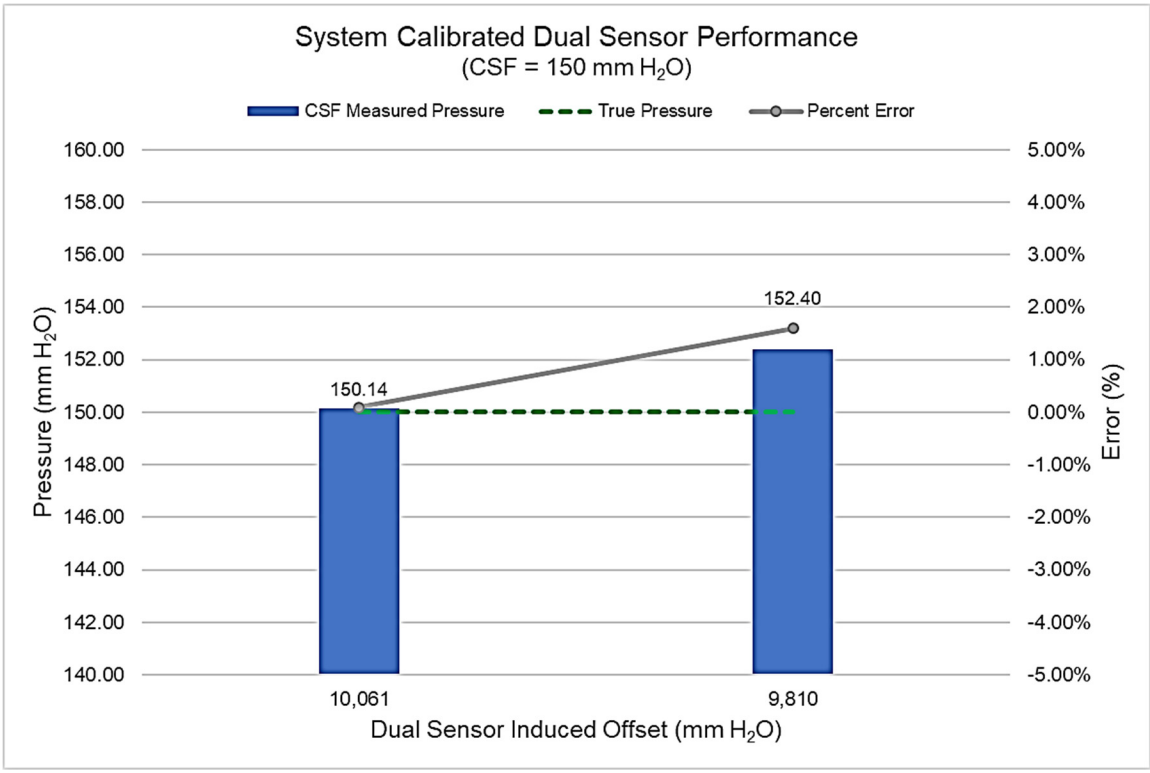


Figure 62 - System calibrated dual sensor performance for 150 mm H_2O and induced offset shift.

ventricular pressure was 2.75 mm H_2O, or 1.83%. For 100 mm H_2O, the maximum measured error was 1.99%. The system meets the objectives of O4.3 for gain and offset correction. Furthermore, for the extent of gain and offset induced and the corresponding calibration results, the sensor is anticipated to correct drift to within ±50 mm H_2O over its expected service life per O5.1. Although the research focus of this work is upon the system calibrated biopressure sensor and interface, as outlined in Figure 26, requirements were nevertheless considered in R4.0 that the sensor support non-invasive readout. The power consumption, signal levels, and geometry all come under consideration to facilitate such an implantable non-invasive readout system. Figure 26 illustrates one potential system design employing the Texas Instruments® TE CC2541 for providing Bluetooth Low Energy communications to and from the transponder. The CC2541 additionally integrates a 12-bit analog-to-digital converter (ADC) supporting an input range from 0 to 3.6 V. The laboratory front-end circuit given in Figure 48 can be modified to support the CC2541's ADC by reducing the gain of the instrumentation amplifier (IA). Although the laboratory's front-end circuit could be passively or actively attenuated to optimize the circuit's signal to noise ratio, doing so would consume additional power. Provided the sensor signal is amplified close to the die, reducing the IA may be the best compromise to preserve power consumption. Figure 63 shows the schematic of the reconfigured front-end circuit biased by a common positive rail of +5V with a reference of 1.54V to shift the output of the IA to support both positive and negative pressure signals. The sensor's +5V bridge

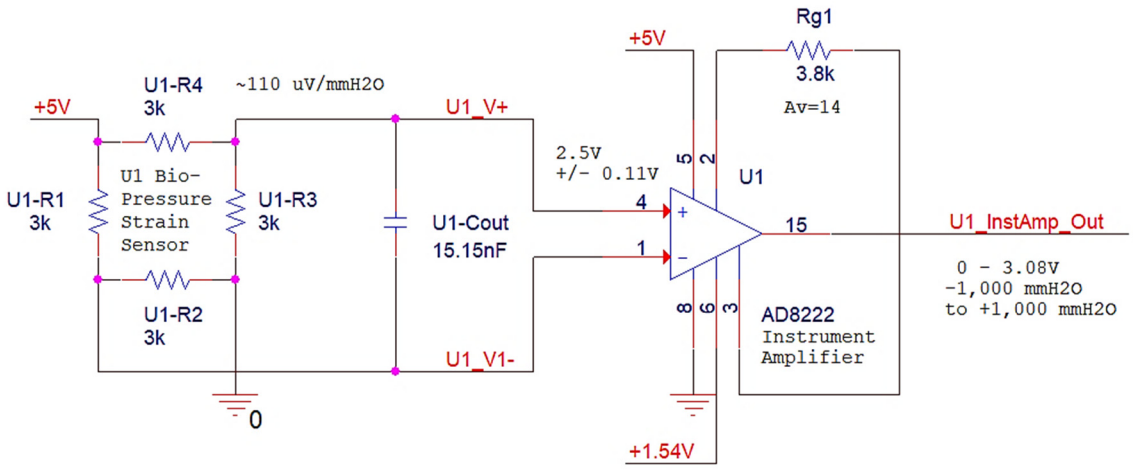


Figure 63 – 5V front-end circuit design with V_o of 0-3.08 V supporting TI CC2541

bias is the same as that used by the sensor's laboratory testing. The IA output range is designed in the circuit to support -1,000 mm H_2O to +1,000 mm H_2O over a 0 to 3.08V range with 1.54V representing the zero-pressure signal level. Therefore, the sensor's front-end electronics can be configured for compatibility with the TI CC2541 ADC per O4.1.Operating power consumption of the primary components outlined in Figure 25 was calculated and is shown in Table 10. Altogether, the custom dual matched-die transponder providing Bluetooth LE communications and wireless inductive powering is calculated to consume roughly 146 milliwatts. The amount of power that can be safely transmitted transcutaneously into humans has been studied and outlined by the Institute of Electrical and Electronic Engineers (IEEE) in standard C95.1 [137]. Maximum permissible exposure (MPE) for the general public in the frequency range of Bluetooth 4.0 or 5.0 (i.e. 2.4 GHz) is limited to 10 watts per square meter averaged over 30 minutes.

Sampling of the biopressure sensor transponder in two patient positions is anticipated to consume no more than 30 seconds of powering and communications in total (assuming one ICP sample per 30-minute period). With respect to the power transmission exposure area, the TI BQ500210EVM, as an example Qi transmitter, utilizes a 44 mm diameter coil, resulting in an area of 6,079 mm^2. The total permissible power transmission for this area, according to the standard, is 60.8 mW averaged over thirty minutes. Equivalently averaging this limit over 30-seconds of a 30-minute period results in 3.648 W, which is 25x

Table 10 – Power consumption of transponder's main components.

	Power (mW)	Notes
Sensor Die 1	8.3	At 5V bias.
Sensor Die 2	8.3	At 5V bias.
U1 IA	5.5	At 5V bias.
U2 IA	5.5	At 5V bias.
TI CC2541	60.1	In active transmit mode.
STWLC04	58.5	60% efficiency
Total:	146.2	milli-watts

the power estimation tabulated in Table 10 for the transponder. Therefore, the transponder's power requirements for transcutaneous transfer meets the safety limits of IEEE C95.1 as specified by O4.2.

pressure upon a resting hydrophobic surface. At any liquid-gas interface, a molecule residing at a free surface of the liquid will encounter a weaker binding energy than that within the bulk, thereby resulting in a net positive surface energy. For water, this surface energy is 72 milli-Joules per square meter (or milli-Newtons per meter) at 25°C. To minimize the liquid's surface energy state, higher energy surface molecules are minimized via cohesive intermolecular

Table 11 outlines the main component volumes for the transponder comprising a PCB substrate, sensors, readout electronics, power reception and regulation electronics, Bluetooth LE transceiver, and antenna component. The volume consumed is just under 3,000 mm^3. The maximum volume of a typical CSF reservoir dome indicated by O2.1 is 3,464 mm^3. Therefore, the biopressure sensor's transponder components meets the objectives of O2.1 with volume remaining.

Non-Ideal Effects and Challenges

During the course of this research numerous challenges arose with most being related to the measurement of very low pressures and challenges with small scale fluid transfer. Pressures distinguished by this work were on the order of 1 mm H_2O. Due to surface tension, a mere drop of water typically poses twice this pressure upon a resting hydrophobic surface. At any liquid-gas interface, a molecule residing at a free surface of the liquid will encounter a weaker binding energy than that within the bulk, thereby resulting in a net positive surface energy. For water, this surface energy is 72 milli-Joules per square meter (or milli-Newtons per meter) at 25°C. To minimize the liquid's surface energy state, higher energy surface molecules are minimized via cohesive intermolecular

Table 11 – Transponder primary component volumes

Component	X mm	Y mm	Z mm	Volume mm^3
Substrate	15.00	29.00	1.57	683.0
Sensor Die 1	2.10	2.10	0.65	2.9
Sensor Die 2	2.10	2.10	0.65	2.9
U1 IA	4.10	4.10	0.80	13.4
U2 IA	4.10	4.10	0.80	13.4
TI CC2541	6.15	6.15	1.00	37.8
STWLC04	3.09	4.70	0.55	8.0
Antenna (DIA)	33.00	33.00	0.64	2198.5
			Total:	2,960 mm^3

forces, resulting in minimal surface area. These internal surface forces are referred to as surface tension. Surface tension can easily result in several millimeters of water pressure in a closed system. The capillary effect, resulting from both cohesive intermolecular forces and adhesive forces to a surrounding vessel, is known to lift the sap in trees and plants several meters. While the benefits of these properties are abundant and critical, their effect can be detrimental in a low pressure measurement system.

As an example, Figure 64 shows the effects of initial outgassing from polyvinyl chloride (PVC) tubing used to hydraulically couple a liquid pressure source to one of the pressure sensors studied. While these bubbles certainly have a limited impact upon occupying volume within the system and increasing the liquid's pressure, they have not yet maximized their effect. With time, on the order of 24 hours, the microbubbles aggregate into air pockets making full contact with the interior circumference of the tubing as shown in Figure 65. At this point, surface tension and capillary effects take their toll upon accurately measuring the system's desired liquid pressure reservoir. Their effect reduces the reservoir pressure sensed by the sensor. Additionally, surface tension effects at edge interfaces were examined to withstand relatively large pressures before translating head pressure to the system.

The most challenging of air pockets was within the sensor die itself and its mating ceramic through-hole. Although the volume is estimated at only little more than 1 mm^3, as tabulated by Table 12, the resulting moisture transfer

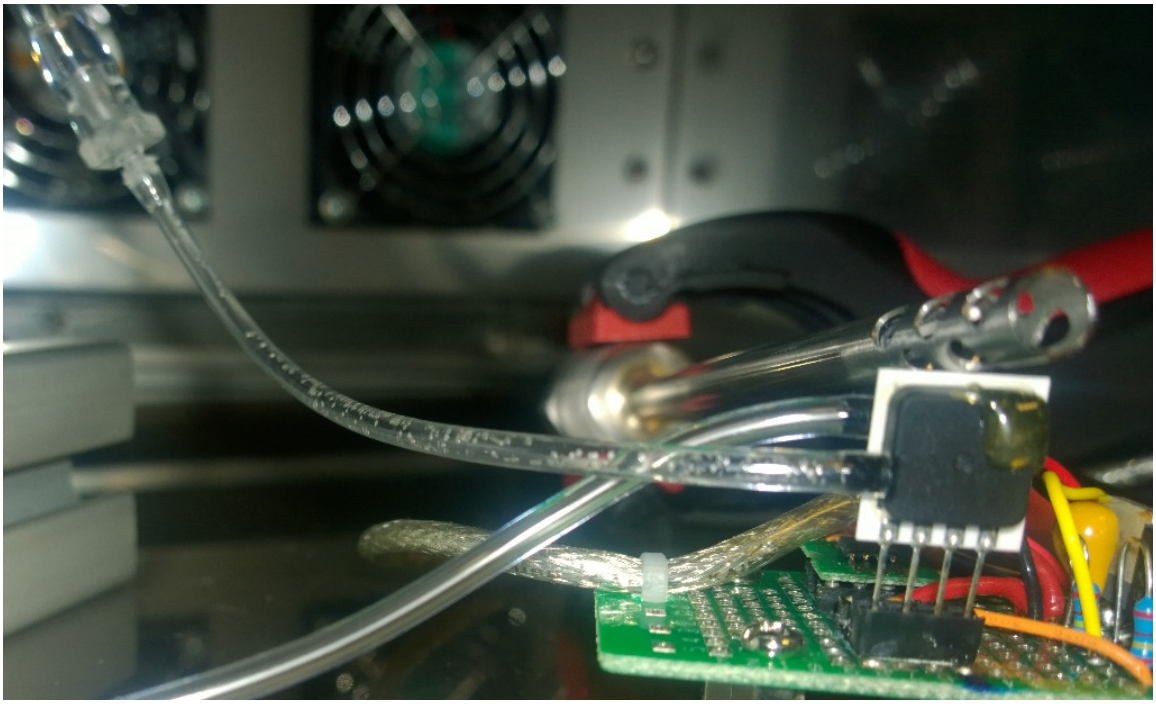


Figure 64 – Initial outgassing of polyvinyl chloride (PVC) tubing.

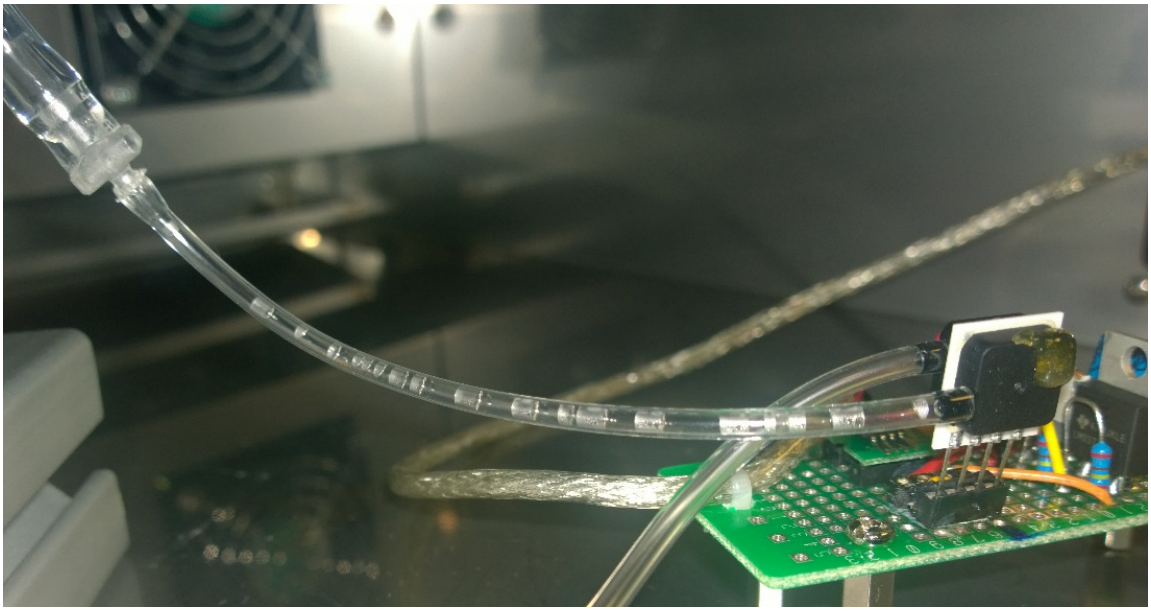


Figure 65 – Bubble formation and air voids from advanced outgassing of tubing.

Table 12 – Sensor and supporting substrate cavity volume.

Cavity	L (mm)	W (mm)	H (mm)	Radius (mm)	Volume (mm^3)
Ceramic Through-Hole	--	--	1.000	0.362	0.412
Chip Support	--	--	0.257	0.362	0.106
Si sensor	1.487	1.487	0.335	--	0.741
				Total:	1.258 mm^3

caused very non-linear and unstable pressures. Figure 66 charts the air-liquid transfer that began to occur within the first several days of pressurizing the BLVR sensor with liquid. The data shown was acquired using a National Instruments DAQ system utilizing a sampling period of one-minute. Corresponding observations of bubble formation are superimposed on the graph.

As can be seen from the graph, a sharp increase in pressure of approximately 13 mm H_2O occurs upon the initial condensation of liquid occupying the unwetted silicon cavity. A slight convex expansion of gas can next be observed just covering the sensor port. The following exponential response results from the slow fluid transfer occurring between the sensor's bottom-side air cavity and the liquid pressure chamber.

Air-liquid transfer was observed over five distinct phases, and the process is hypothesized as follows:

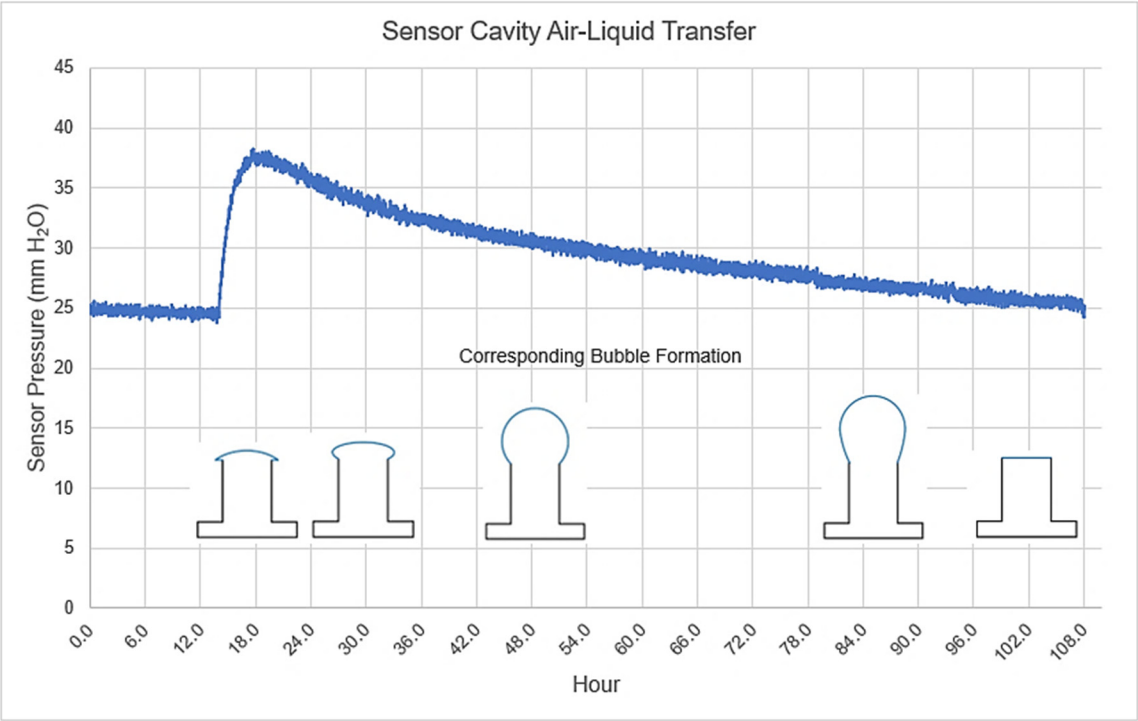


Figure 66 – Sensor cavity air-liquid transfer and bubble formation.

1. The initial air-liquid boundary interface, whereby surface tension and the air cavity's counterpressure counteract the liquid's hydrostatic pressure, maintains near-term equilibrium.
2. Water vapor transfer resulting from unequally bonded surface molecules on the liquid's surface concentrates within the chip's air cavity and condenses, resulting in initial mass transfer and air displacement. In this phase, pressure sharply increases, and a surface bubble begins to form on top of the ceramic substrate's port hole. Vapor transfer increasingly alters at this point due to the increased pressure within the air cavity.
3. Continued liquid mass transfer occurs resulting in a growing gas bubble with increased interior pressure yet with surface tension preventing complete displacement.
4. Additional accumulating water vapor condenses inside the pressure sensor's cavity further displacing air and increasing the size of the bubble. The bubble then extends beyond the circumference of the ceramic port hole and forms an underside curvature that results in a growing buoyant force due to the liquid's pressure gradient from the bottom of the spherical shape to the top. Although pressure within the sessile bubble increases, as evident by the diameter of the bubble versus the hydrostatic exterior pressure, the bubble's upward buoyancy force reduces pressure within the sensor's cavity.
5. Once buoyant forces exceed the partial bubble's surface tension forces surrounding the circumference of the pressure port, then the air pocket

ascends in the form of a complete sphere. Spherical shape is maintained upon evacuation whereby liquid water minimizes its surface energy counterbalanced by the positive pressure within the air bubble. At this point of equilibrium, distributed contraction forces equal the bubble's interior pressure by the Young-Laplace law [138]:

$$\Delta p = \frac{2\alpha}{r}$$

where Δp is the difference in pressure from within the sphere versus the exterior for a given bubble radius, r, and where α is the surface energy (or tension), which for water is approximately 70 mJ/m^2 (or 70 milli-Newtons/m) at 37°C. Relative positive pressure exists toward the center of curvature.

Steps 1 through 5 repeats until the entire cavity is at final equilibrium with stable pressure.

To gain further insight into this process a COMSOL Multiphysics simulation was undertaken. A 2-D axisymmetric two-phase flow, phase-field, study with heat transfer and moisture transport was setup for the sensor geometry under 4 mm of water pressure. The model utilized the Cahn-Hilliard equation with a chemical potential to represent the diffuse interface between the immiscible liquid and air domains. The Navier-Stokes equations were used for fluid transport and conservation of mass. Wetted walls were used for simulating surface tension or capillary effects encompassing a glass pressure cylinder atop the sensor's

ceramic substrate and the silicon support structure and sensor itself. The heat transfer from the sensor to the liquid was modeled by convection in moist air, as shown in Figure 38. Initially, the liquid pressure chamber contained 4 mm of water with a hydrostatic pressure of ρgz at the sensor's inlet port. The initial conditions for the sensor's port cavity was set to 40% humidity. Environmental conditions were set to 1 atmosphere at 37°C. Figure 67 reveals the pressure gradient after 90 minutes showing the pressure presented to the surface of the sensor, without any bubble formation, is indeed 4 mm H_2O.

The concentration of water vapor at 90 minutes is shown in Figure 68 with approximately 2.43 moles of water vapor, or 99.76% relative humidity. The difference in dew point and the cavity's ambient temperature under this pressure is only -0.05°C before condensation occurs. Figure 69 shows the water volume fraction of the assembly revealing only partial liquid penetration into the cavity under surface tension resistance. Figure 70 shows the corresponding fluid velocity of very small volumes at 100 to 250 microns per second. Convergence beyond 90 minutes for the multiphysics model was not achievable.

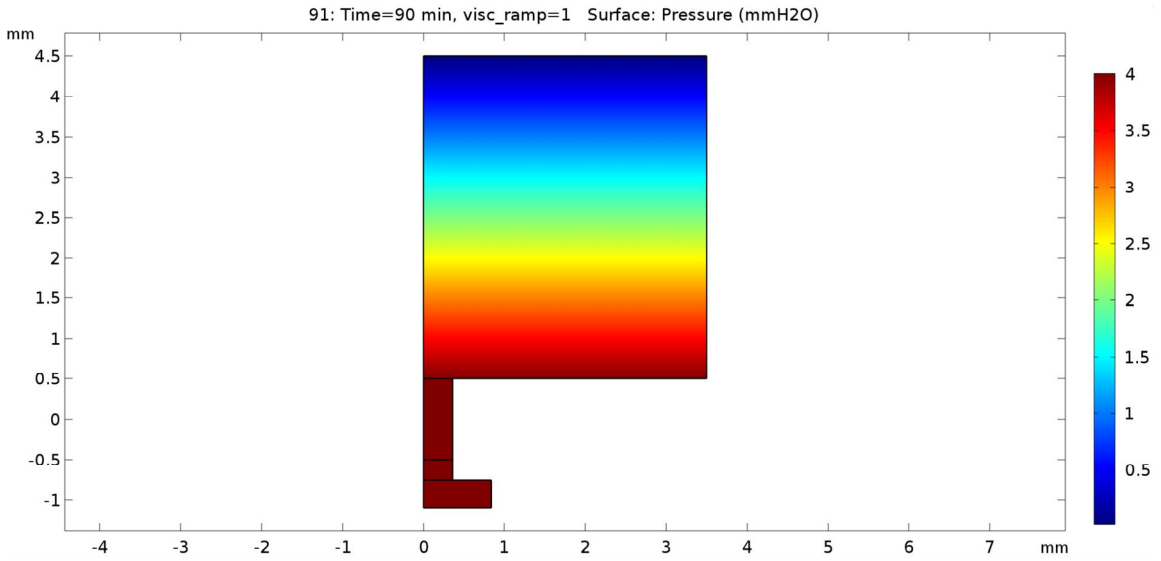


Figure 67 – COMSOL axisymmetric pressure gradient.

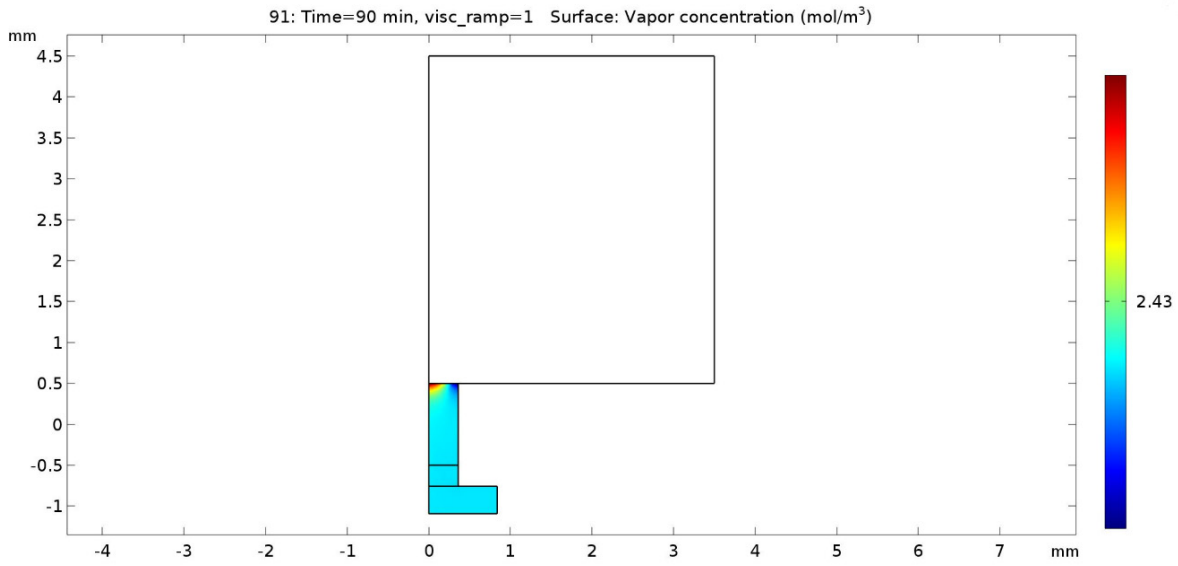


Figure 68 - COMSOL axisymmetric water vapor concentration.

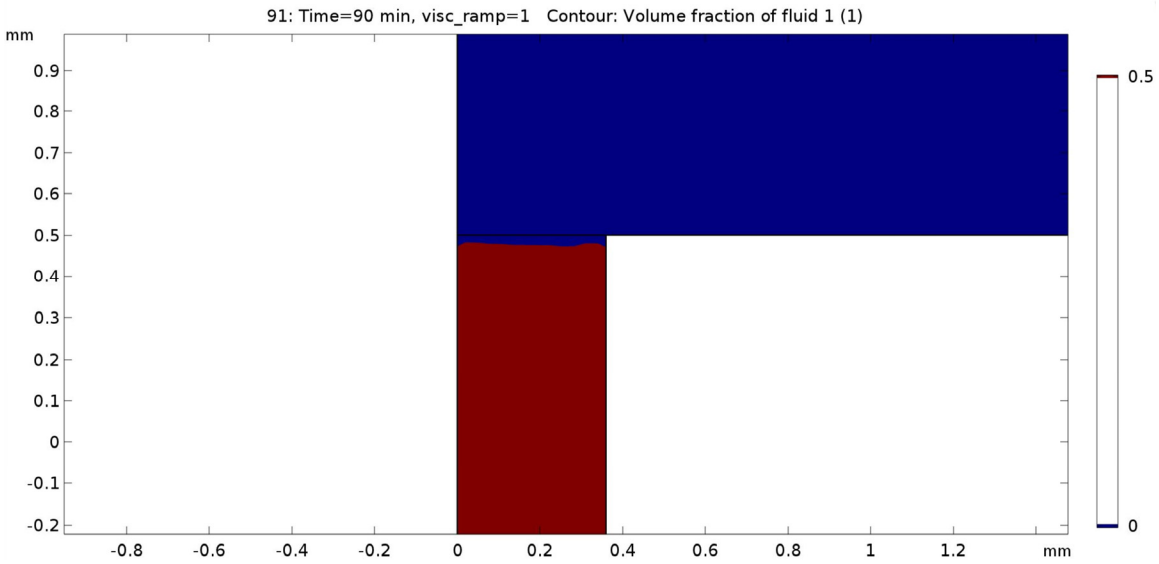


Figure 69 - COMSOL axisymmetric water volume fraction.

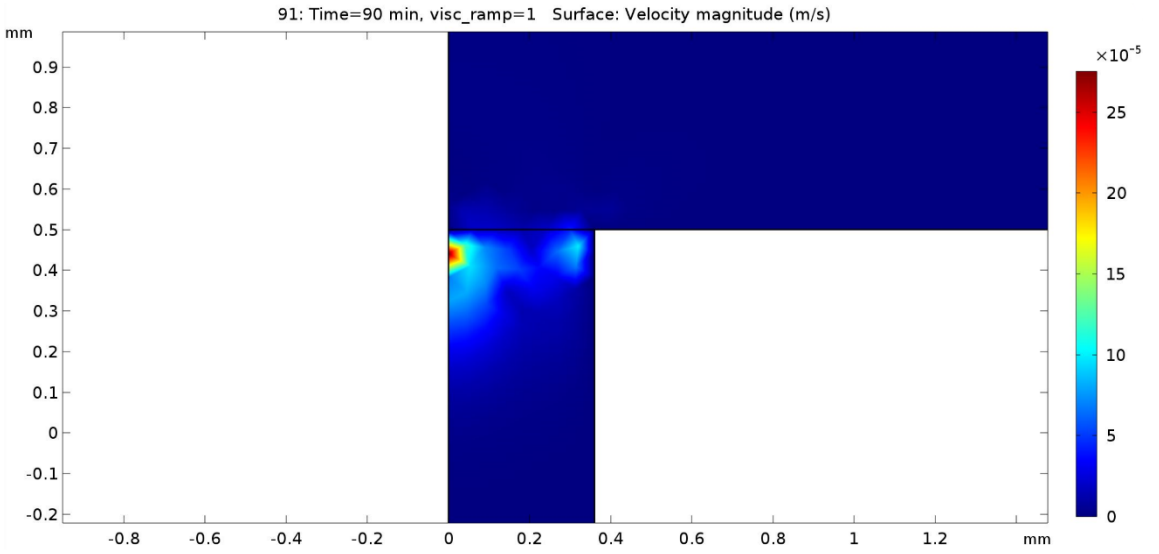


Figure 70 - COMSOL axisymmetric fluid velocity.

A re-setup of the model to include various forms of partial spherical microbubbles in contact with the ceramic substrate's port hole was unsuccessful at modeling the actual observed behavior. The intent of the bubble simulation was to evaluate fluctuating pressures produced within the sensor's cavity. However, within milli-seconds, the simulation collapsed the bubble and generally returned to the state of the prior model. It was therefore not possible to model the full behavior, including partial bubble formation adhered to the substrate, over several days. Nevertheless, the COMSOL simulation provided insight into the cavity's pressure in the absence of a bubble and to convey the extent of water vapor concentration within a short period of time.

Further challenges with air pockets were encountered beyond outgassing and air-liquid fluid transfer. Nucleation of microbubbles from entrained air was common with fresh water. The bleeding of air from small crevices and other cavities also had to be overcome. As can be seen in the lower right-hand quadrant of Figure 64, a venting port, later sealed with a viscous hard glue, was used to initially bleed the system. Unfortunately, each of these air voids would result in compression and potentially alter the baseline measurement of the fluid column's pressure as pressure was increased (such as in transfer function testing). By the Ideal Gas Law, pressure and volume have an inverse relationship, thereby as more pressure was added to a burette source, any downstream air pockets would compress and shift the total column of liquid, resulting in non-linearity in the measurement. For measuring transfer functions,

resolution, and other measurements, shifts of only a few millimeters could have significant impact. Therefore, it became paramount to eliminate gas sources such as entrained air in test liquids. Materials with significant outgassing was either eliminated (e.g. PVC), minimized via surface area, or mitigated though vent ports until outgassing diminished (e.g. epoxied materials).

Additional challenges early in the research ensued with top-side liquid media contact. Figure 71 shows a microphotograph of metal migration eventually resulting from distilled water testing, which quickly turned conductive. The allure of top-side liquid sensing was the alleviation of challenges with the bottom-side sensor cavity as described above. Some manufacturers, such as TE Connectivity, conduct top-side die biosensing with the use of a dielectric silicone gel for fluid isolation. However, the TE Connectivity device earlier described is limited to 72 hours use, likely in part due to the permeability of the gel.

Further PV=nRT effects were encountered by the custom dual biopressure sensor's absolute pressure chamber. The chamber is shared by both top-side dies, as shown in Figure 21 and Figure 45, and is temperature sensitive. The volume of the top-side chamber is approximately 180 mm^3. For a chamber sealed at standard atmospheric pressure and 21°C, the number of moles of air within the chamber equates to 7.46 micromoles. Under normal circadian fluctuations in brain temperature of 0.2°C, this results in only 7 mm H_2O change over the period. Given the biopressure sensor's deployment, which is intended

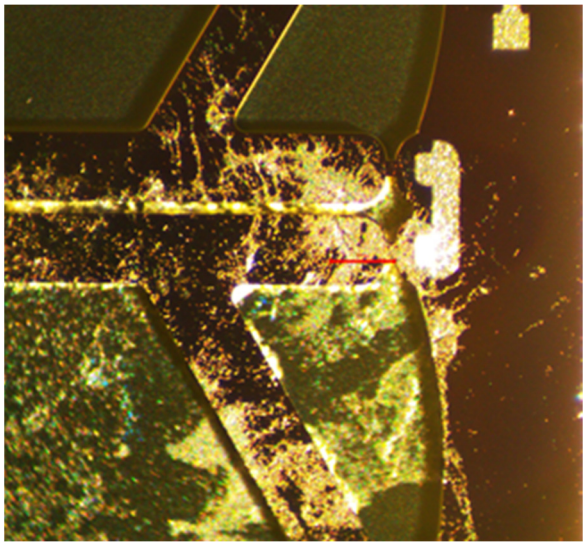


Figure 71 – Top-side die metal migration from liquid media contact.

to encounter only very short timeframes between two position calibration measurements, temperature fluctuation is of low concern. However, during thermal chamber testing in the laboratory, large temperature shifts occurred during the opening and closing of the chamber's door, which was captured in data acquisition, as shown in Figure 72.

Figure 72 shows the converted pressure read by each pressure sensor, U1 and U2. The setup for this particular snapshot of data was that each die had individual bottom-side pressure stimuli of equal pressure. However, due to fluid transfer earlier described, this particular acquisition period revealed an offset between the two dies. Furthermore, a large offset was induced by the change in temperature of the absolute pressure chamber from room temperature construction to chamber testing, resulting in absolute pressure readings much higher than otherwise expected. In essence, this snapshot of data altogether captures several of the non-ideal effects encountered.

Of particular relevance was the change in pressure for both dies resulting from the change in temperature of the chamber door opening. For U2, for example, the pressure reading just prior to opening the chamber door was 309 mm H_2O with a temperature probe in the chamber reading 36.25°C (the chamber's standard sensor read 37.0°C). One minute after opening the door, the temperature probe read 26.79°C and the pressure reading increased to 664 mm H_2O (+355 mm change). While it would intuitively seem that the pressure reading should drop with a reduction in temperature, it should be noted that the

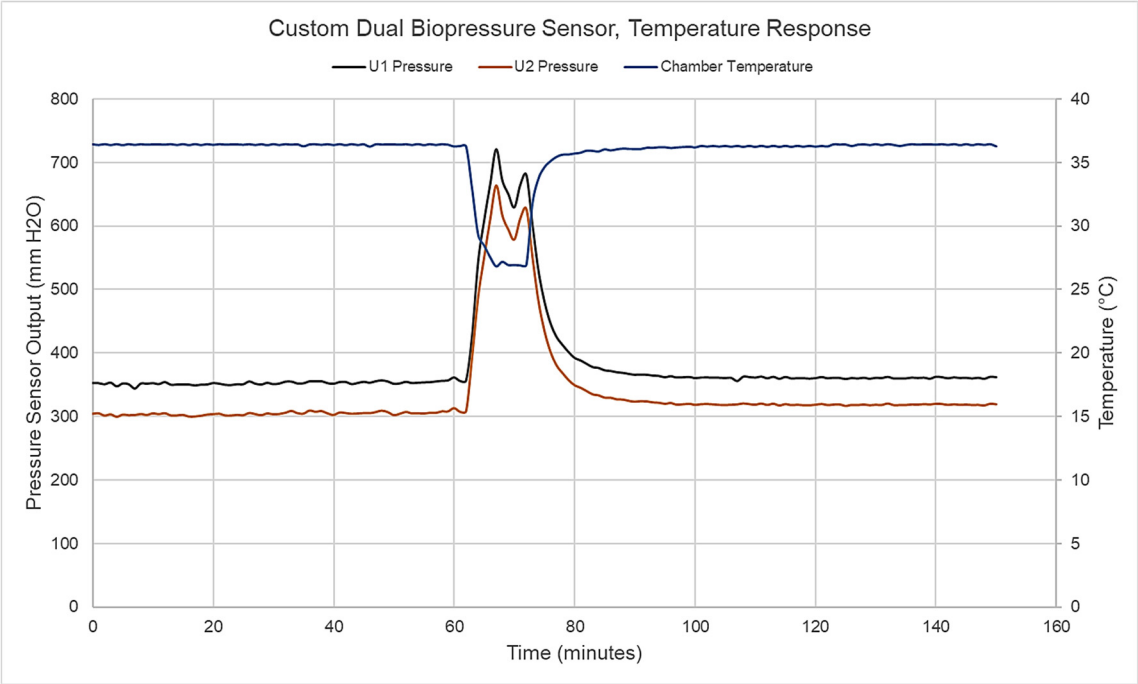


Figure 72 – Custom dual biopressure sensor absolute reference temperature response.

pressure chamber stimulates the top-side of both dies counteracting bottom-side liquid stimulation. Therefore, a drop in top-side pressure from a reduction in the absolute pressure chamber's pressure would equivalently result in an increased pressure reading bottom-side. The ideal gas law predicts a shift of 334 mm H_2O for the chamber's 9.5°C cooling. However, a shift of only 0.6°C further matches the measured 355 mm H_2O change, which is conceivable given the temperature probe was not placed directly onto the sensor's reference chamber, but further interior to the thermal chamber.

Additional consideration to the absolute pressure reference is necessary with respect to barometric pressure shifts. Similar to the effect of a large temperature swing upon the reference's pressure is the opposite effect of a large common-mode pressure swing to bottom-side sources such as that under atmospheric pressure shifts. As described in the Sensor System Design section, extreme barometric pressures can span from 8,872 mm H_2O on the low end up to 11,472 mm H_2O on the high end, a 2,600 mm H_2O range. Further to this point, on an airline flight, environmental pressures were recorded that spanned from 10,298 to 8,375 mm H_2O between near sea-level take-off to a cruising altitude of 9,449 meters (31,000 feet), a difference of 1,923 mm H_2O. However, the former weather pressure metrics were under extreme conditions and from world records such as a cyclone's interior pressure. The latter pressure range, taken during flight, was under conditions untypical of measuring ICP. Nevertheless, the sensor dies utilized within this research have a burst pressure of over 20,000 mm

H_2O and a proof pressure of 5,080 mm H_2O. During the course of this work, no non-linearity effects upon the sensors transfer function was observed, even under induced offset testing. As a more practical range, over the almost three-year period sensor testing was conducted, local barometric pressure conditions varied a maximum of 535 mm H_2O. In any event, should a further increase in tolerance to very large environmental pressure swings become necessary, matched pressure sensor dies could be fabricated at the potential expense of resolution.

Altogether, the non-ideal effects encountered by this research were surmountable. Solutions to many of the problems was to simply avoid or evacuate air intrusion into the system. Additionally, sufficiently large diameter lumens were employed where there was a free surface that would otherwise allow any surface tension or capillary effects to occur. Bottom-side die stimulation was used versus top-side for liquid media compatibility. Fluid transfer into the bottom-side cavity was eliminated by micro-positioning 30-gauge needles to pre-wet the cavity. Glass cylinders or tubing was utilized to eliminate outgassing. Where outgassing could elsewhere occur, material choices were made to minimize the impact or was otherwise allowed to stabilize prior to use.

CHAPTER FIVE

CONCLUSIONS AND RECOMMENDATIONS

In summary, chronic intracranial hypertension, or hydrocephalus**,** is a debilitating condition that affects millions of people. Prior to shunt treatments in the 1950's hydrocephalus was typically fatal. Shunts are life saving devices, but have yet to be perfected and, as a result, have about a 50% failure rate by their second year of implant. The typical onset of symptoms for hydrocephalus often begins with a headache which can shortly thereafter lead to fatal consequences without intervention. The same is true for a failed shunt and nearly all shunted patients undergo a surgical revision for replacement by year 10. Such headaches are not only associated with escalating hypertension, however. Shunts often under- or over-drain CSF, particularly under siphoning conditions, which also presents with a headache. Therefore, headaches for hydrocephalus patients are not always indicative of a forthcoming life-threatening emergency. The conundrum is, short of invasive procedures, there are currently no accurate means of measuring ICP to understand if a shunt has failed, needs adjustment, or if a headache is otherwise benign. Patients, well aware of shunt failure rates and the ensuing consequences frequently undergo ionizing imaging diagnostics. Such imaging is often inconclusive, and patients next undergo invasive techniques for assessing or revising their shunt. Billions of dollars are spent each year on the diagnostics and treatments of hydrocephalus when many of these costly procedures could be reduced with non-invasive and non-ionizing diagnostics for measuring ICP.

Similar to arterial blood pressure diagnostics, which are easily and reliably performed in a patient's home, a non-invasive means of quantitative ICP measurement would allow early alerts of escalating ICP and further enable hydrocephalus shunt valve optimization. Clearly, the need exists for such a diagnostic device and researchers have cited a long-standing need for telemetric ICP technology.

As found from a survey of the literature, drift in pressure measurement accuracy has been, and remains, the inhibiting factor to enabling a viable long-term implantable ICP device. Offset error has been identified to frequently occur from a change in ex-vivo to in-vivo temperatures upon implant. Gain error, however, has been found multifactorial, yet with thermally induced packaging stress as the predominant factor. Other degradations include bonding damage, oxidation growth, and the deterioration of an integrated circuit's photo-resistive layer. A recent study concluded that sensor drift was largely unpredictable, making deterministic compensation techniques challenging. Evaluations conducted over several years of this research found even the most sophisticated driftless commercial devices drift in excess of 20% and with large unpredictable shifts.

The research herein has resulted in a new, novel, and patented diagnostic approach to mitigating both offset and gain drift in low-pressure liquid-media sensing. The approach exploits the effect of gravitational siphoning in shunt systems to provide a means for gain and offset calibration. By utilizing two independent, yet matched, silicon sensor dies, known pressure changes in one

bio-compartment can be used for calibrating sensor measurements in another, such as the brain. The work herein included construction of the new device and the evaluation of crucial performance aspects necessary for long-term ICP measurement.

Several custom dual biopressure sensors were constructed and tested over the course of this research. As outlined in Chapter Three's Requirements, a number of research objectives were established for evaluating the new sensor. Table 13 provides the keyed objectives which were traced throughout Chapter Four's Results and Discussion.

O1.1 – 1.3 relate to the overall requirement that the implantable biopressure sensor provide biocompatible interfaces. The results from Chapter Four examined the materials of the new sensor as well as materials that may be used in conjunction with the sensor dies. Overall, the materials were referenced to prior studies showing strong biocompatibility and hermeticity suitable for sterilization and implant in humans.

O2.1 relates to the requirement that the overall transponder be geometrically compatible as a cranial implant. A very standard device geometry, currently in clinical use, was selected to compare its volume with that of the sensor's overall transponder components. Chapter Four tabulated the results and demonstrated fulfillment of the objective.

Table 13 – Research Objective Fulfillment

Research Objectives		Fulfillment
O1.1	Justification of sensor to present a bottom-side bulk micromachined monocrystalline die surface for the pressure diaphragm to meet biocompatibility. Die must be capable of bonding to suitably hermetic biocompatible materials. Sensor must withstand sterilization method(s).	✓
O1.2	Device to be capable of sustaining a compatible wash and autoclaving, ethylene oxide, or gamma radiation sterilization without damage.	✓
O1.3	Surfaces to be capable of hermeticity to meet the intended service life of the implant.	✓
O2.1	The sensor's transponder components must be capable of being contained within a typical CSF reservoir's volume (34 mm diameter and 7.2mm height) for suitable implantation below the scalp, yet above the skull, with pressure communication through a cranial burr hole.	✓ 2,960 < 3,464 mm^3 Limit
O3.1	Sensor must provide a pressure range from -500 mm H_2O to +500 mm H_2O.	✓
O3.2	Sensor must provide a 10 mm H_2O resolution, or less, up to 200 mm H_2O and within a 10% maximum beyond.	✓ 3.4 mm H_2O
O3.3	Sensor must provide a maximum accuracy (or trueness) of ±5 mm H_2O.	✓ 3.73 mm H_2O
O3.4	Sensor must provide a maximum precision of ±5 mm H_2O.	✓ 1.16 mm H_2O

Table 13 (continued)

Research Objectives		Fulfillment
O3.5	The sensor must overall provide a combined maximum accuracy (incl. precision) of ±10 mm H_2O.over a ±200 mm H_2O range and 10% maximum beyond.	✓ 4.89 mm H_2O
O4.1	Buffered sensor output must be capable of providing a signal within a 0 - 3.3 volt range for interfacing to the Texas Instruments CC2541 ADC and Bluetooth LE system-on-chip.	✓ 0 - 3.08V
O4.2	The estimated power consumption of the sensor's transponder must be less than that which can be transcutaneously transmitted safely per IEEE Standard for Safety Levels with Respect to Human Exposure to Radio Frequency Electromagnetic Fields, C95.1.	✓ 0.146 < 3.648 W Limit
O4.3	The sensor must be capable of gain and offset calibration to meet the specified accuracy.	✓
O5.1	Expected drift over the device's intended service life must be less than ±50 mm H_2O.	✓ Correctable to within 2.75 mm H_2O

O3.1 – 3.5 stem from the requirement that the sensor provide clinically acceptable ICP resolution and accuracy. Each objective was justified within the context of clinical literature for providing diagnostics to hydrocephalus patients. The pressure range, resolution, and accuracy were all demonstrated by the new custom device to fulfill the objectives.

Objectives O4.1 – 4.3 relate specifically to the sensor's ability to support non-invasive calibration and readout. The sensor and front-end electronics were shown compatible with a prevailing wireless Bluetooth LE system-on-chip (SoC). Additionally, the power consumption of the sensors and transponder components were shown to be within safe limits for transcutaneous powering. Finally, both objectives O4.3 and O5.1 were satisfied with data demonstrating the new device's capability for self-calibration to mitigate large gain and offset drifts to within 3 mm H_2O.

In conclusion, a survey of the literature and of the most recent technology indicates that measurement drift over time is the limiting factor to enabling long-term implantable ICP monitoring. Research herein pursued a means of reducing and overcoming such drift. A new novel patented device and calibration method thereof utilizing matched-dies with dual references to mitigate drift was developed and evaluated. The device and method demonstrated the ability to negate large shifts in gain and offset in the laboratory to within a few millimeters of water pressure, showing promise for in-vivo application. Future research will seek to replicate the sensor system and performance in-vivo in an animal model.

LIST OF REFERENCES

[1] H. Kimelberg, "Water Homeostasis in the Brain: Basic Concepts," *Neuroscience,* vol. 129, pp. 851-860, 2004.

[2] R. Ravi and R. Morgan, "Intracranial Pressure Monitoring," *Current Anaesthesia and Critical Care,* vol. 14, pp. 229-235, 2003.

[3] J. M. Drake and C. Sainte-Rose, The Shunt Book, Cambridge: Blackwell Science, 1995.

[4] J. Sotelo, "The hydrokinetic parameters of shunts for hydrocephalus might be inadequate," *Surgical Neurology International,* vol. 3, no. 40, 2012.

[5] L.-O. D. Koskinen and M. Olivecrona, "Clinical Experience with the Intraparenchymal Intracranial Pressure Monitoring Codman MicroSensor System," *Neurosurgery,* vol. 56, pp. 693-698, 2005.

[6] M. J. McGirt, J.-C. Leveque, J. C. W. III, A. T. Villavicencio, J. S. Hopkins, H. E. Fuchs and T. M. George, "Cerebrospinal Fluid Shunt Survival and Etiology of Failures: A Seven-Year Institutional Experience," *Pediatric Neurosurgery,* vol. 36, p. 248–255, 2002.

[7] P. Chumas, A. Tyagi and J. Livingston, "Hydrocephalus—what's new?," *Arch Dis Child Fetal Neonatal Ed,* vol. 85, pp. F149-F154, 2001.

[8] N. Lundberg, "Continuous Recording and Control of Ventricular Fluid Pressure in Neurosurgical Practice," *Acta Psychiatrica Scandinavica Supplement,* vol. 36, no. Suppl 149, pp. 1-193, 1960.

[9] J. Young, O. Blow, F. Turrentine, J. Claridge and A. Schulman, "Is there an upper limit of intracranial pressure in patients with severe head injury if cerebral perfusion pressure is maintained?," *Neurosurgical Focus,* vol. 15, no. 6, p. E2, 2003 .

[10] K. Holloway, T. Barnes and e. a. S. Choi, "Ventriculostomy infections: the effect of monitoring duration and catheter exchange in 584 patients.," *Journal of Neurosurgery,* vol. 85, pp. 419-424, 1996.

[11] I. Piper, A. Barnes, D. Smith and L. Dunn, "The Camino Intracranial Pressure Sensor: Is it Optimal Technology? An Internal Audit with a Review of Current Intracranial Pressure Monitoring Technologies," *Neurosurgery,* vol. 49, no. 5, pp. 1158-1165, 2001.

[12] A. Lozier, R. Sciacca, M. Romagnoli and E. C. Jr., "Ventriculostomy-related infections: a critical review of the literature," *Neurosurgery,* vol. 51, no. 1, pp. 170-182, 2002.

[13] H. I. Fried, B. R. Nathan, A. S. Rowe, J. M. Zabramski, N. Andaluz, A. Bhimraj, M. M. Guanci, D. B. Seder and a. J. M. Singh, "The Insertion and Management of External Ventricular Drains: An Evidence-Based Consensus Statement," *Neurocritical Care Society,* vol. 24, no. 1, pp. 61-81, 2006.

[14] FISO, "Fiber Optic Sensing Solutions for the Medical Industry," 2018. [Online]. Available: https://fiso.com/en/service/medical/. [Accessed 21 October 2018].

[15] Natus Medical, "Camino Intracranial Pressure Monitor," 2018. [Online]. Available: https://neuro.natus.com/products-services/camino-intracranial-pressure-monitor. [Accessed 20 October 2018].

[16] Integra Life Sciences, "Codman Microsensor ICP Transducer," September 2015. [Online]. Available: https://www.integralife.com/file/general/1529421641.pdf. [Accessed 21 October 2018].

[17] C. Wiegand and P. Richards, "Measurement of Intracranial Pressure in Children: A Critical Review of Current Methods," *Developmental Medicine adn Child Neurology,* vol. 49, pp. 935-941, 2007.

[18] X. Zhang, J. E. Medow, B. J. I. F. Wang, M. Shokoueinejad, J. Koueik and J. G. Webster, "Invasive and noninvasive means of measuring intracranial pressure: a review," *Institute of Physics and Engineering in Medicine,* vol. 38, p. R143–R182, 2017.

[19] M. I. Hirzallah and H. A. Choi, "The Monitoring of Brain Edema and Intracranial Hypertension," *Jounal of Neurocritical Care,* vol. 9, no. 2, pp. 92-104, 2016.

[20] C. Robba, S. Bacigaluppi, D. Cardim, J. Donnelly, A. Bertuccio and M. Czosnyka, "Non-invasive assessment of intracranial pressure," *Acta Neurologica Scandinavica,* vol. 134, no. 1, pp. 4-21, 2016.

[21] Hydrocephalus Association, About Hydrocephalus, San Francisco, 2010.

[22] G. Cinalli, W. Maixner and C. Sainte-Rose, Pediatric Hydrocephalus, Milano: Springer-Verlag Italia, 2005.

[23] J. H. Chir, H. J. Fullerton and N. Gupta, "Time trends and demographics of deaths from congential hydrocephalus in children in the United States: National Center for Health Statistics data, 1979 to 1998," *Journal of Neurosurgery,* vol. 103, pp. 113-118, 2005.

[24] Hydrocephalus Association, "Hydrocephalus," [Online]. Available: https://www.hydroassoc.org/hydrocephalus. [Accessed 19 October 2019].

[25] R. A. Rachel, "Hydrocephalus - The Dana Guide," The Dana Foundation, New York, 2007.

[26] American Association of Neurological Surgeons, "AANS National Neurosurgical Procedural Statistics," AANS, Rolling Meadows, 2012.

[27] R. V. Patwardhan and A. Nanda, "Implanted ventricular shunts in the United States: The billion-dollar-a-year cost of hydrocephalus treatment," *Neurosurgery,* vol. 56, no. 1, pp. 139-145, 2004.

[28] F. Nulsen and E. Spitz, "Treatment of hydrocephalus by direct shunt from ventricle to jugular vein," *Surg. Forum,* vol. 1951, pp. 399-403, 1951.

[29] R. Pudenz, F. Russell, A. Hurd and C. Shelden, "Ventriculoauriculostomy; a technique for shunting cerebrospinal fluid into the right auricle; preliminary report," *Journal of Neurosurgery,* vol. 14, pp. 171-179, 1957.

[30] R. Ames, "Ventriculo-peritoneal shunts in the management of hydrocephalus," *Journal of Neurosurgery,* vol. 27, pp. 525-529, 1967.

[31] J. M. Drake, J. R. Kestle, R. Milner, G. Cinalli, F. Boop, J. P. Jr., S. Haines, S. Schiff, D. D. Cochrane, P. Steinbok and N. MacNeil, "Randomized Trial of Cerebrospinal Fluid Shunt Valve Design in Pediatric Hydrocephalus," *Neurosurgery,* vol. 43, no. 2, pp. 294-303, 1998.

[32] C. Sainte-Rose, J. Piatt, D. Renier, A. Pierre-Kahn, H. H. J.F. Hirsch and E. H. R.P. Humphreys, "Mechanical complications in shunts," *Pediatric Neurosurgery,* vol. 17, no. 1, pp. 2-9, 1991.

[33] J. P. Jr. and C. Carlson, "A search for determinants of cerebrospinal fluid shunt survival: retrospective analysis of a 14-year institutional experience.," *Pediatric Neurosurgery,* vol. 19, pp. 233-242, 1993.

[34] J. J. Stone, C. T. Walker, M. Jacobson, V. Phillips and H. J. Silberstein, "Revision rate of pediatric ventriculoperitoneal shunts after 15 years," *Journal of Neurosurgery,* vol. 11, no. 1, pp. 15-19, 2013.

[35] A. Haridas and T. Tadanori, "Hydrocephalus in children: Management and prognosis," Wolters Kluwer Health, 2018.

[36] M. S. B. Edwards and M. Derechin, "Hydrocephalus in children: Management and Prognosis," Hydrocephalus Association, San Francisco, 2010.

[37] S. Antes, C. A. Tschan, M. Heckelmann, D. Breuskin and J. Oertel, "Telemetric Intracranial Pressure Monitoring with the Raumedic Neurovent P-tel," *World Neurosurgery,* vol. 91, pp. 133-148, 2016.

[38] S. Welschehold, E. Schmalhausen, P. Dodier, S. Vulcu, J. Oertel, W. Wagner and C. A. Tschan, "First Clinical Results With a New Telemetric Intracranial Pressure-Monitoring System," *Operative Neurosurgery,* vol. 70, no. 1, pp. 44-49, 2012.

[39] F. Freimann, C. Sprung, S. Chopra, P. Vajkoczy and S. Wolf, "Large-scale referencing of the telemetric neurovent-P-tel intracranial pressure sensor in a porcine model," *Pediatric Neurosurgery,* vol. 49, pp. 29-32, 2013.

[40] T. O. H. Miyake, Y. Kajimoto, M. Matsukawa and a. H. Miyake, "A new ventriculoperitoneal shunt with a telemetric intracranial pressure sensor: clinical experience in 94 patients with hydrocephalus," *Neurosurgery,* vol. 40, no. 5, pp. 931-935, 1997.

[41] T. Kamiryo, Y. Fujii, M. Kusaka, S. Kashiwagi and H. Ito, "Intracranial pressure monitoring using a programmable pressure valve and a telemetric intracranial pressure sensor in a case of slit ventricle syndrome after multiple shunt revisions," *Child's Nervous System,* vol. 7, no. 4, pp. 233-234, 1991.

[42] S. Antes, A. Stadie, S. Mueller, S. Linsler, D. Breuskin and J. Oertel, "Intracranial PressureeGuided Shunt Valve Adjustments with the Miethke," *World Neurosurgery,* vol. 10, no. 44, pp. E642-E650, 2017.

[43] M. Harary, R. G. F. Dolmans and W. B. Gormley, "Intracranial Pressure Monitoring—Review and Avenues for Development," *Sensors,* vol. 18, no. 465, pp. 1-15, 2018.

[44] E. Stehlin, "Clinical Compatibility of an Implantable Pressure Sensing Device With Consideration of the Intracranial Pressure Application," The University of Auckland, New Zealand, Auckland, 2015.

[45] K. March and L. Madden, "Intracranial Pressure Management," in *Monitoring technologies in critically ill neuroscience patients*, Sudbury, Jones and Bartlett, 2009, p. 37.

[46] L. Yu, B. J. Kim and E. Meng, "Chronically Implanted Pressure Sensors: Challenges and State of the Field," *Sensors,* vol. 14, pp. 20620-20644, 2014.

[47] C. E. Seaver, "An Implantable Dual Sensor Bio-Pressure Transponder and Method of Calibration". U.S.A. Patent 9,668,663, 6 June 2017.

[48] P. H. Raboel, J. B. Jr., M. Andresen, B. M. Bellander and B. Romner, "Intracranial PressureMonitoring: Invasive versus Non-InvasiveMethods—A Review," *Critical Care Research and Practice,* vol. 2012, 2012.

[49] C. Hawthorne and I. Piper, "Monitoring of intracranial pressure in patients with traumatic brain injury," *Frontiers in Neurology,* vol. 5, no. 121, pp. 1-16, 2014.

[50] T. Luerssen, "Intracranial pressure: Current status in monitoring and management.," *Elsevier: Pediatric Neurology,* vol. 4, pp. 146-155, 1997.

[51] I. Pople, M. Muhlbauer, R. Sanford and e. al., "Results and Complications of Intraaranial Pressure Monitoring in 303 Children.," *Pediatric Neurosurgery,* vol. 23, pp. 64-67, 1995.

[52] S. Shapiro, R. Bowman, J. Callahan and e. al., "The Fiberoptic Intraparenchymal Cerbral Pressure Monitor in 244 Patients," *Surgical Neurology,* vol. 145, pp. 278-282, 1996.

[53] E. Münch, R. Weigel, P. Schmiedek and L. Schürer, "The Camino intracranial pressure device in clinical practice: reliability, handling characteristics and complications.," *Acta Neurochirurgica,* vol. 140, no. 11, pp. 1113-1120, 1998.

[54] M. Gelabert-Gonzalez, V. Ginesta-Galan, R. Sernamito-Garcia, A. G. Allut, J. Bandin-Dieguez and R. M. Rumbo, "The Camino intracranial pressure device in clinical practice. Assessment in a 1000 cases.," *Acta Neurochirurgica,* vol. 148, no. 4, pp. 435-441, 2006.

[55] M.-A. Poca, J. Sahuquillo, M. Arribas, M. Báguena, S. Amorós and E. Rubio, "Fiberoptic intraparenchymal brain pressure monitoring with the Camino V420 monitor: reflections on our experience in 163 severely head-injured patients.," *Journal of Neurotrauma,* vol. 19, no. 4, pp. 439-448, 2002.

[56] J. Hayward and M. Baker, "Role of cerebral arterial blood in the regulation of brain temperature in the monkey.," *American Journal of Physiology,* vol. 215, no. 2, pp. 389-403, 1968.

[57] W. Young, Roark's Formulas for Stress and Strain, McGraw-Hill Professional, 2011.

[58] M. D. Giovanni, Flat and Corrugated Diaphragm Design Handbook, New York: Marcel Dekker, 1982.

[59] N. Ross and C. Eynon, "Intracranial Pressure Monitoring," *Current Anaesthesia and Critical Care,* vol. 16, pp. 255-261, 2005.

[60] Y. Z. Al-Tamimi, A. Helmy, S. Bavetta and S. J. Price, "Assessment of zero drift in teh Codman intracranial pressure monitor: A study from 2 neurointensive care units.," *Neurosurgery,* vol. 64, no. 1, pp. 94-99, 2009.

[61] A. Oshorov, I. A. Savin, K. A. Goriachev, K. A. Popugaev, A. A. Polupan, A. A. Sychev and T. F. Tabasaranskiĭ, "Post-monitoring changes in zero drift of Codman intracranial pressure sensors.," *Anesteziologiia i Reanimatologiia ,* vol. 3, pp. 62-66, 2011.

[62] Y. H. Yau, I. R. Piper, R. E. Clutton and I. R. Whittle, "Experimental evaluation of the Spiegelberg intracranial pressure and intracranial compliance monitor," *Journal of Neurosurgery,* vol. 9, no. 5, pp. 1-6, 2000.

[63] J.-M. Lang, J. Beck, M. Zimmermann, V. Seifert and A. Raabe, "Clinical evaluation of intraparenchymal Spiegelberg pressure sensor," *Neurosurgery,* vol. 52, no. 6, pp. 1455-1459, 2003.

[64] Möller Medical GmbH, "LiquoGuard," 2018. [Online]. Available: https://www.moeller-medical.com/en/end-user/liquoguardr.html. [Accessed 9 November 2018].

[65] Moller Medical, GmbH, *LiquoGuard 7,* Albany: Moeller Medical Devices USA, 2015.

[66] B. J. E. Misgeld, I. M. Elixmann, L. Fahnster, M. Walter, M. Weinzierl, W.-I. Steudel and S. Leonhardt, "Design and Evaluation of an Automatic Extraventricular Drainage Control System," *IEEE Transactions on Control Systems Technology,* vol. 23, no. 6, pp. 2283-2292, 2015.

[67] Möller Medical GmbH, "LiquoGuard 7 (U.S. FDA 510k: K150898)," FDA, Silver Spring, 2015.

[68] Samaun, K. D. Wise and J. B. Angell, "An IC Piezoresistive Pressure Sensor for Biomedical Instrumentation," *IEEE Transactions on Biomedical Engineering,* vol. 20, no. 2, pp. 101-109, 1973.

[69] S. Y. Yurish, "Universal Interfacing Circuit for Resistive-Bridge Sensors," in *IEEE 2010 Conference on Sensor Device Technologies and Applications*, Venice, 2010.

[70] D. Crescini, V. Ferrari, Z. Vajna, D. Marioli, A. Taroni, A. Borgese, M. Marinelli, E. Milani, A. Paoletti, A. Tucciarone and G. Verona-Rinati, "Design and Development of a Piezoresistive Pressure Sensor on Micromachined Silicon for High Temperature Applicatoins and of a Signal-Conditioning Electronic Circuit," *Microsystem Technologies,* vol. 9, pp. 431-435, 2003.

[71] A. George, W. P. Chan, M. Narducci, Z. H. Kong and M. Je, "CMOS-MEMS Capacitive Sensors for Intra-cranial Pressure Monitoring: Sensor Fabrication & System Design," *IEEE ISOCC,* pp. 375-378, 2012.

[72] L. Y. Chen, B. C. Tee, A. L. Chortos, G. Schwartz, V. Tse, D. J. Lipomi, H. P. Wong, M. V. McConnell and Z. Bao, "Continuous wireless pressure monitoring and mapping with ultra-small passive sensors for health monitoring and critical care," *Nature Communications,* vol. 5, p. 5028, 2014.

[73] M. Behfar, "Design, Development and in vivo Evaluation of a Wireless Platform for Intracranial Pressure Monitoring Using Inductive Passive Implants," Tampere University of Technology, Tampere, 2018.

[74] Abbott, "CardioMEMS," 2018. [Online]. Available: https://www.sjm.com/en/sjm/cardiomems. [Accessed 20 October 2018].

[75] M. G. Allen, "Micromachined Endovascularly-Implantable Wireless Aneurysm Pressure Sensors: From Concept to Clinic," in *IEEE Solid-State Sensors, Actuators and Microsystems*, Seoul, 2005.

[76] S. C. Lee and C. J. Lueck, "Cerebrospinal Fluid Pressure in Adults," *Journal of Neuro-Ophthalmology,* vol. 34, no. 3, pp. 278-283, 2014.

[77] J. Vender, J. Waller, K. Dhandapani and D. McDonnell, "An evaluation and comparison of intraventricular, intraparenchymal, and fluid-coupled techniques for intracranial pressure monitoring in patients with severe traumatic brain injury," *Journal of Clinical Monitoring and Computing,* vol. 25, p. 231, 2011.

[78] B. B. Bruce, "State-of-the-Art Review: Non-invasive assessment of cerebrospinal fluid pressure," *Journal of Neuroophthalmology,* vol. 34, no. 3, p. 288–294, 2014.

[79] W. Newman, A. Hollman, G. Dutton and R. Carachi, "Measurement of Optic Nerve Sheath Diameter by Ultrasound: A Means of Detecting Acute Raised Intracranial Pressure in Hydrocephalus," *British Journal of Ophthalmology ,* vol. 86, pp. 1109-1113, 2002.

[80] "Boston Neurosciences," 2017. [Online]. Available: http://bostonneurosciences.com. [Accessed 4 August 2018].

[81] A. Ragauskas, V. Matijosaitis, R. Zakelis, K. Petrikonis, D. Rastenyte, I. Piper and G. Daubaris, "Clinical assessment of noninvasive intracranial pressure absolute value measurement method," *Neurology,* 2012.

[82] L. Desch, "Longitudinal Stability of Visual Evoked Potentials in Children and Adolescents with Hydrocephalus.," *Developmental Medicine and Child Neurology,* vol. 43, pp. 113-117, 2001.

[83] K. A. Townsend, J. W. Haslett, T. K. Tsang, M. N. El-Gamal and K. Iniewski, "Recent Advances and Future Trends in Low Power Wireless Systems for Medical Applications," in *IEEE Fifth International Workshop on System-on-Chip for Real-Time Applications*, Calgary, 2005.

[84] J. R. Atkinson, D. B. Shurtleff and E. L. Foltz, "Radio telemetry for the measurement of intracranial pressure," *Journal of Neurosurgery,* vol. 27, no. 5, pp. 428-432, 1967.

[85] R. MacKay, Telemetering from within the body, New York: Academic Press, 1965, p. 185.

[86] E. Cosman, N. Zervas, P. Chapman, B. Cosman and M. Arnold, "A telemetric pressure sensor for ventricular shunt systems," *Surgical Neurology,* vol. 11, no. 4, pp. 287-294, 1979.

[87] N. Zervas, E. Cosman and B. Cosman, "A pressure-balanced radio-telemetry system for the measurement of intracranial pressure monitoring by telemetry," *Journal of Neurosurgery,* vol. 47, no. 6, pp. 899-911, 1977.

[88] G. Güçer, L. Viernstein, A. Wang and R. Szymanski, "Ten-Year Follow-up on the Performance of a Telemetric Intracranial Pressure Sensor," *Neurosurgery,* vol. 22, no. 5, p. 892–896, 1988.

[89] A. Kim, C. R. Powell and B. Ziaie, "An Universal packaging technique for low-drift implantable pressure sensors," *Biomedical Microdevices,* vol. 18, no. 2, p. 32, 2016.

[90] L. Brancato, G. Keulemans, T. Verbelen, B. Meyns and R. Puers, "An Implantable Intravascular Pressure Sensor for a Ventricular Assist Device," *Micromachines,* vol. 7, no. 135, pp. 1-17, 2016.

[91] A. D. DeHennis and K. D. Wise, "A Fully Integrated Multisite Pressure Sensor for Wireless Arterial Flow Characterization," *IEEE Journal of Microelectromechanical Systems,* vol. 15, no. 3, pp. 678-685, 2006.

[92] Raumedic Ag, "Telemetric ICP Measurement," Raumedic Ag, 2018. [Online]. Available: https://www.raumedic.com/neuromonitoring/neuro-icu/telemetry/. [Accessed 4 August 2018].

[93] Miethke, "SENSOR RESERVOIR," Christoph Miethke GmbH & Co. KG, 2018. [Online]. Available: https://www.miethke.com/en/products/sensor-reservoir/. [Accessed 4 August 2018].

[94] Christoph Miethke GmbH & Co. KG, "Sensor Reservoir Brochure," [Online]. Available: https://www.miethke.com/en/products/sensor-reservoir/. [Accessed 05 August 2018].

[95] M. A. Flitter, M. Sussman and e. al., *ANSI/AAMI NS28:1988/(R)2015 Intracranial pressure monitoring devices,* Arlington: American National Standard, Association for Advancement of Medical Instrumentation, 2015.

[96] A. Aschoff, P. Kremer, C. Benesch, K. Fruh, A. Klauk and S. Kunze, "Overdrainage and Shunt Technology," *Child's Nervous System,* vol. 11, pp. 193-202, 1995.

[97] S. Lollis, A. Mamourian, T. Vaccaro and A. Duhaime, "Programmable CSF Shunt Valves: Radiographic Identification and Interpretation," *American Journal of Neuroradiology,* vol. 31, no. 7, pp. 1343-1346, 2010.

[98] Medtronic, Inc., "Delta® Valves and Shunt Assemblies IFU," 2016. [Online]. Available: http://manuals.medtronic.com/content/dam/emanuals/st/CONTRIB_087685.pdf. [Accessed 21 July 2018].

[99] G. Zemack, J. Bellner, P. Siesjo, L. Stromblad and B. Romner, "Clinical Experience with the Use of a Shunt with an Adjustable Valve in Children with Hydrocepalus," *Journal of Neurosurgery,* vol. 98, pp. 471-476, 2003.

[100] L. J. Viernstein, "Intracranial Pressure Monitoring," *John Hopkins APL Technical Digest,* vol. 1, no. 2, pp. 135-138, 1980.

[101] A. A. Barlian, W.-T. Park, J. R. M. Jr., A. J. Rastegar and B. L. Pruitt, "Review: Semiconductor Piezoresistance for Microsystems," *Proceedings of the IEEE,* vol. 97, no. 3, pp. 513-552, 2009.

[102] W. P. Eaton and J. H. Smith, "Micromachined Pressure Sensors: Review and Recent Developments," *Smart Materials and Structures,* vol. 6, no. 5, p. 530ff, 1997.

[103] E. Kennedy, Operational Amplifier Circuits: Theory and Applications, Fort Worth: Holt, Rinehart and Winston, Inc., 1988.

[104] C. S. Smith, "Piezoresistive effect in germanium and silicon," *Physical Review,* vol. 94, no. 1, pp. 42-49, 1954.

[105] C. Herring, "Transport properties of a many valley semiconductor," *Bell System Technical Journal,* vol. 34, no. 2, pp. 237-290, 1955.

[106] S. K. Clark and K. D. Wise, "Pressure sensitivity in anisotropically etched thin-diaphragm pressure sensors," *IEEE Transactions on Electron Devices,* vol. 26, no. 12, pp. 1887-1896, 1979.

[107] J. C. Doll and B. L. Pruitt, Piezoresistor Design and Applications, New York: Springer, 2013.

[108] C. Liu, Foundations of MEMS, Upper Saddle River: Pearson, 2011.

[109] M. Bao, Handbook of Sensors and Actuators, Volume 8, Micromechanical Transducers, Amsterdam: ElSevier B.V., 2000.

[110] R. Spencer, B. M. Fleischer, P. W. Barth and J. B. Angell, "A theoretical study of transducer noise in piezoresistive and capacitive silicon pressure sensors," *IEEE Transactions on Electron Devices,* vol. 35, no. 8, pp. 1289-1298, 1988.

[111] K. Hoffman, An Introduction to Measurements Using Strain Gages, Darmstadt: Hottinger Baldwin Messtechnik GmbH, 1989.

[112] K. Petersen, "Silicon as a Mechanical Material," *Proceedings of the IEEE,* vol. 70, no. 5, pp. 420-457, 1982.

[113] A. C. Fischer, F. Forsberg, M. Lapisa, S. J. Bleiker, G. Stemme, N. Roxhed and F. Niklaus, "Integrating MEMS and ICs," *Nature: Microsystems & Nanoengineering,* vol. 1, no. 15005, p. 1016, 2015.

[114] S. Meti, K. B. Balavald and B. G. Sheeparmatti, "MEMS Piezoresistive Pressure Sensor: A Survey," *International Journal of Engineering Research and Applications,* vol. 6, no. 4, pp. 23-31, 2016.

[115] A. Pinato, "Reliability and Parylene encapsulation of organic devices," University of Padova, Padua , 2011.

[116] D. A. Dauenhauer and H. Reimann, "Silicon Pressure Sensor Chip with a Shear Element on a Sculptured Diaphragm". U.S.A Patent 5,178,016, 12 January 1993.

[117] M. Esashi, H. Komatsu, T. Matsuo, M. Takahashi, T. Takishima, K. Imabayashi and H. Ozawa, "Fabrication of catheter-tip and sidewall miniature pressure sensors," *IEEE Transactions on Electron Devices,* vol. 29, no. 1, pp. 57-63, 1982.

[118] L. F. Fuller and S. Sudirgo, "Bulk Micromachined Pressure Sensor," in *IEEE Proceedings of the 15th Biennial: University/Government/Industry Microelectronics Symposium, 2003;*, Boise, 2003.

[119] A. Schmidt, "Wheatstone Bridge Input and Output Resistance," 20 June 2017. [Online]. Available: https://www.digikey.com/eewiki/x/OYF8Aw. [Accessed 05 August 2018].

[120] D. Dauenhauer, D. Dauenhauer, A. Breitenbach and H. Erichsen, "Pressure Transducer with Error Compensation from Cross-Coupling Outputs of Two Sensors". U.S.A. Patent 6,023,978, 15 February 2000.

[121] A. D. Kurtz and A. A. Ned, "Combined Absolute Differential Transducer". U.S.A. Patent 7,057.247, 6 June 2006.

[122] W. T. Ulrich, A. F. Gebert, H. Haberl and M. Schulz, "Shunt survival rates by using the adjustable differential pressure valve combined with a gravitational unit (proGAV) in pediatric neurosurgery," *Childs Nervous System,* vol. 29, p. 425–431, 2013.

[123] M. Paff, D. Alexandru-Abrams, M. Muhonen and W. Loudon, "Ventriculoperitoneal shunt complications: A review," *Interdisciplinary Neurosurgery: Advanced Techniques and Case,* vol. 13, pp. 66-70, 2018.

[124] J. Walker and L. M. Criddle, "Pathophysiology and Management of Abdominal Compartment Syndrome," *American Journal of Critical Care,* vol. 12, pp. 367-371, 2003.

[125] National Oceanic and Atmospheric Administration, "Most intense tropical cyclone on record," 21 April 2010. [Online]. Available: http://www.aoml.noaa.gov/hrd/tcfaq/E1.html. [Accessed 26 July 2013].

[126] World Meteological Organization, "World: Highest Sea Level Air Pressure Above 750 meters," Arizona State University School of Geographical Sciences, 2012. [Online]. Available: https://wmo.asu.edu/content/highest-sea-lvl-air-pressure-above-700m. [Accessed 21 October 2018].

[127] World Meteorlogical Organization, "World: Highest Sea Level Air Pressure Below 750 meters," Arizona State University School of Geographical Sciences, 2012. [Online]. Available: https://wmo.asu.edu/content/world-highest-sea-level-air-pressure-below-700m. [Accessed 21 October 2018].

[128] C. E. Seaver, "An Implantable Low Pressure Biosensor Transponder," Trace: Tennessee Research and Creative Exchange, Knoxville, 2013.

[129] F. Maloberti, Analog Design for CMOS VLSI Systems, Boston: Springer, 2003.

[130] I. Glass, D. Budgett, S. Malpas and D. McCormick, "Isolation of Drift Factors in MEMS Pressure Sensors," in *Auckland Bioengineering Institute*, Auckland, 2015.

[131] G. Kotzara, M. Freasa, P. Abelb, A. Fleischmanc, S. Royc, C. Zormand, J. M. Morane and J. Melzak, "Evaluation of MEMS materials of construction

for implantable medical devices," *Biomaterials,* vol. 23, pp. 2737-2750, 2002.

[132] A. Hogg, T. Aellen, S. Uhl, B. Graf, H. Keppner, Y. Tardy and J. Burger, "Ultra-thin layer packaging for implantable electronic devices," *Journal of Micromechanics Microengineering,* vol. 23, pp. 1-12, 2013.

[133] G. Jiang, "Design challenges of implantable pressure monitoring system," *Frontiers in Neuroscience,* vol. 4, no. 29, 2010.

[134] M. R. Dokmeci, J. v. Arx and K. Najafi, "Accelerated testing of anodically bonded glass-silicon packages in salt water," in *IEEE Solid State Sensors and Actuators*, Chicago, 1997.

[135] S. Weisenberg, S. TerMaath, C. Seaver and J. Killeffer, "Ventricular catheter development: past, present, and future," *Journal of Neurosurgery,* vol. 125, pp. 1504-1512, 2016.

[136] Bosch Sensortec, "BMP280," Bosch Sensortec GmbH, 2018. [Online]. Available: https://www.bosch-sensortec.com/bst/products/all_products/bmp280. [Accessed 19 10 2018].

[137] IEEE International Committee on Electromagnetic Safety, "IEEE Standard for Safety Levels with Respect to Human Exposure to Radio Frequency Electromagnetic Fields, 3 kHz to 300 GHz," IEEE, New York, 2005.

[138] B. Lautrup, Physics of Continuous Matter, Boca Raton: CRC Press, 2011.

[139] M. Rosner and D. Becker, "ICP monitoring: Complications and Associated Factors," *Clinical Neurosurgery,* vol. 23, pp. 494-519, 1976.

[140] M. Czonsnka and J. Pickard, "Monitoring and Interpretation of Intracranial Pressure," *Journal of Neurology Neurosurgery Psychiatry,* vol. 75, pp. 813-821, 2004.

[141] M. Ghovanloo and S. Atluri, "An Integrated Full-Wave CMOS Rectifier With Built-In Back Telemetry for RFID and Implantable Biomedical Applications," *IEEE Transactions on Circuits and Systems,* vol. 55, no. 10, pp. 3328-3334, 2008.

[142] H. Ali, T. J. Ahmad and S. A. Khan, "Inductive Link Design for Medical Implants," in *IEEE Symposium on Industrial Electronics and Applications*, Kuala Lumpur, Malaysia, 2009.

[143] G. Wang, W. Liu, M. Sivaprakasam and G. A. Kendir, "Design and Analysis of an Adaptive Transcutaneous Power Telemetry for Biomedical Implants," *IEEE Transactions on Circuits and Systems,* vol. 52, no. 10, pp. 2109-2117, 2005.

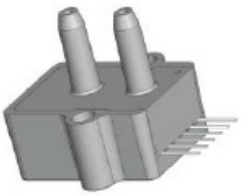
[144] J. V. Ham and R. Puers, "A Power and Data Front-end IC for Biomedical Monitoring Systems," *Sensors and Actuators,* vol. 147, pp. 641-648, 2008.

[145] B. J. Iskandar, C. McLaughlin, T. B. Mapstone, P. A. Grabb and W. J. Oakes, "Pitfalls in the Diagnosis of Ventricular Shunt Dysfunction: Radiology Reports and Ventricular Size," *Pediatrics,* vol. 101, pp. 1031-1036, 1998.

APPENDIX

Millivolt Output Pressure Sensors

Low Pressure (0.5" H_2O to 30 " H_2O) Sensors



Features

- 0 to 0.5" H_2O to 0 to 30" H_2O Pressure Ranges
- Temperature Compensated
- Calibrated Zero and Span

Applications

- Medical Instrumentation
- Environmental Controls
- HVAC

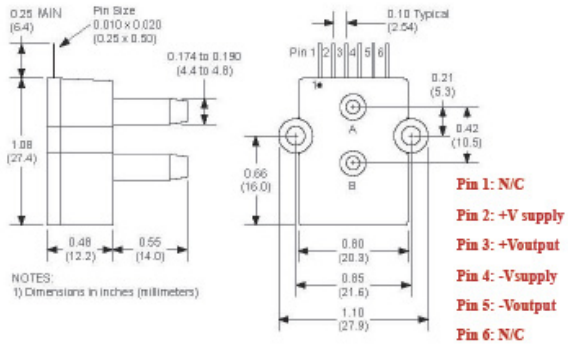
General Description

The Millivolt Output pressure sensor is based upon a proprietary technology to reduce all output offset or common mode errors. This model provides a calibrated millivolt output with superior output offset characteristics. Output offset errors due to change in temperature, stability to warm-up, stability to long time period, and position sensitivity are all significantly reduced when compared to conventional compensation methods. In addition the sensor utilizes a silicon, micromachined, stress concentration enhanced structure to provide a very linear output to measured pressure.

These calibrated and temperature compensated sensors give an accurate and stable output over a wide temperature range. This series is intended for use with non-corrosive, non-ionic working fluids such as air, dry gases and the like.

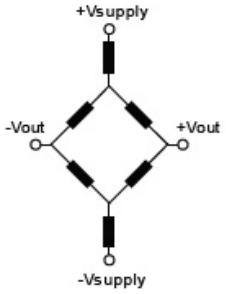
The output of the device is ratiometric to the supply voltage and operation from any D.C. supply voltage up to +16 V is acceptable.

Physical Dimensions



Pin 1: N/C
Pin 2: +V supply
Pin 3: +Voutput
Pin 4: -Vsupply
Pin 5: -Voutput
Pin 6: N/C

Equivalent Circuit



Input Resittance	4.5 k ohm
Output Resistance	1.5 k ohm

Approvals

MKT DATE	MFG DATE	ENG DATE	QA DATE
☐ As Is ☐ With Change	☐ As Is ☐ With Change	☐ As Is ☐ With Change	☐ As Is ☐ With Change

ALL SENSORS
A 16035 Vineyard Blvd. Morgan Hill, CA 95037 P 408 225 4314 F 408 225 2079 E www.allsensors.com

Signed Original On File www.allsensors.com

Pressure Sensor Ratings

Supply Voltage Vs, max	16 Vdc
Common-mode pressure	-10 to +10 psig
Lead Temperature, max (soldering 2-4 sec.)	270°C

Environmental Specifications

Temperature Ranges	
Compensated	0 to 50(70)° C
Operating	-25 to 85° C
Storage	-40 to 125° C
Humidity Limits	0 to 95% RH (non condensing)

Standard Pressure Ranges

Part Number	Operating Pressure	Nominal Span	Proof Pressure	Burst Pressure
0.5 INCH-D-MV	0 - 0.5" H2O	10mV	100 "H2O	200 "H2O
1 INCH-D-MV	0 - 1" H2O	10 mV	100 "H2O	200 "H2O
2 INCH-D-MV	0 - 2" H2O	10mv	100 "H2O	200 "H2O
5 INCH-D-MV	0 - 5" H2O	20 mV	200 "H2O	300 "H2O
10 INCH-D-MV	0 - 10" H2O	20 mV	200 "H2O	300 "H2O
20 INCH-D-MV	0 - 20" H2O	20 mV	200 "H2O	500 "H2O
30 INCH-D-MV	0 - 30" H2O	20 mV	200 "H2O	800 "H2O

Performance Characteristics for 0.5 INCH-D-MV

Parameter, note 1	Minimum	Nominal	Maximum	Units
Operating Range, differential pressure	--	0.5	--	"H2O
Output Span, @ 0.5"H2O, note 5	9.0	10.0	11.0	mV
Offset Voltage @ zero differential pressure	--	--	±500	uV
Offset Temperature Shift (0°C-50°C), note 2	--	--	±250	uV
Offset Warm-up Shift, note 3	--	--	±100	uV
Offset Position Sensitivity (1g)	--	--	±5.0	uV
Offset Long Term Drift (one year)	--	--	±200	uV
Linearity, hysteresis error, note 4	--	0.05	0.25	%fs
Full Scale Shift (0°C-50°C), note 2	--	--	±200	uV

Performance Characteristics for 1 INCH-D-MV

Parameter, note 1	Minimum	Nominal	Maximum	Units
Operating Range, differential pressure	--	1.0	--	"H2O
Output Span, @ 1"H2O, note 5	9.0	10.0	11.0	mV
Offset Voltage @ zero differential pressure	--	--	±500	uV
Offset Temperature Shift (0°C-50°C), note 2	--	--	±250	uV
Offset Warm-up Shift, note 3	--	--	±100	uV
Offset Position Sensitivity (1g)	--	--	±50	uV
Offset Long Term Drift (one year)	--	--	±200	uV
Linearity, hysteresis error, note 4	--	0.05	0.25	%fs
Full Scale Shift (0°C-50°C), note 2	--	--	±200	uV

www.allsensors.com Signed Original On File

Performance Characteristics for 2 INCH-D-MV

Parameter, note 1	Minimum	Nominal	Maximum	Units
Operating Range, differential pressure	--	2.0	--	"H2O
Output Span, note 5	9.0	10.0	11.0	mV
Offset Voltage @ zero differential pressure	--	--	±500	uV
Offset Temperature Shift (0°C-50°C), note 2	--	--	±250	uV
Offset Warm-up Shift, note 3	--	--	±100	uV
Offset Position Sensitivity (1g)	--	--	±50	uV
Offset Long Term Drift (one year)	--	--	±200	uV
Linearity, hysteresis error, note 4	--	0.05	0.25	%fs
Full Scale Shift (0°C-50°C), note 2	--	--	±200	uV

Performance Characteristics for 5 INCH-D-MV

Parameter, note 1	Minimum	Nominal	Maximum	Units
Operating Range, differential pressure	--	5.0	--	"H2O
Output Span, note 5	19.0	20.0	21.0	mV
Offset Voltage @ zero differential pressure	--	--	±500	uV
Offset Temperature Shift (0°C-50°C), note 2	--	--	±150	uV
Offset Warm-up Shift, note 3	--	--	±50	uV
Offset Position Sensitivity (1g)	--	--	±10	uV
Offset Long Term Drift (one year)	--	--	±100	uV
Linearity, hysteresis error, note 4	--	0.05	0.25	%fs
Full Scale Shift (0°C-50°C), note 2	--	--	±200	uV

Performance Characteristics for 10 INCH-D-MV

Parameter, note 1	Minimum	Nominal	Maximum	Units
Operating Range, differential pressure	--	10.0	--	"H2O
Output Span, note 5	19.0	20.0	21.0	mV
Offset Voltage @ zero differential pressure	--	--	±500	uV
Offset Temperature Shift (0°C-70°C), note 2	--	--	±150	uV
Offset Warm-up Shift, note 3	--	--	±50	uV
Offset Position Sensitivity (1g)	--	--	±5	uV
Offset Long Term Drift (one year)	--	--	±100	uV
Linearity, hysteresis error, note 4	--	0.05	0.25	%fs
Full Scale Shift (0°C-70°C), note 2	--	--	±200	uV

ALL SENSORS
A 16035 Vineyard Blvd. Morgan Hill, CA 95037 P 408 225 4314 F 408 225 2079 E www.allsensors.com

www.allsensors.com Signed Original On File

Performance Characteristics for 20 INCH-D-MV

Parameter, note 1	Minimum	Nominal	Maximum	Units
Operating Range, differential pressure	--	20.0	--	"H2O
Output Span, note 5	19.0	20.0	21.0	mV
Offset Voltage @ zero differential pressure	--	--	±500	uV
Offset Temperature Shift (0°C-70°C), note 2	--	--	±150	uV
Offset Warm-up Shift, note 3	--	--	±50	uV
Offset Position Sensitivity (1g)	--	--	±5	uV
Offset Long Term Drift (one year)	--	--	±100	uV
Linearity, hysteresis error, note 4	--	0.05	0.25	%fs
Full Scale Shift (0°C-70°C), note 2	--	--	±200	uV

Performance Characteristics for 30 INCH-D-MV

Parameter, note 1	Minimum	Nominal	Maximum	Units
Operating Range, differential pressure	--	30.0	--	"H2O
Output Span, note 5	19.0	20.0	21.0	mV
Offset Voltage @ zero differential pressure	--	--	±500	uV
Offset Temperature Shift (0°C-70°C), note 2	--	--	±150	uV
Offset Warm-up Shift, note 3	--	--	±50	uV
Offset Position Sensitivity (1g)	--	--	±5	uV
Offset Long Term Drift (one year)	--	--	±100	uV
Linearity, hysteresis error, note 4	--	0.05	0.25	%fs
Full Scale Shift (0°C-70°C), note 2	--	--	±200	uV

Specification Notes

NOTE 1: ALL PARAMETERS ARE MEASURED AT 12.0 VOLT EXCITATION, FOR THE NOMINAL FULL SCALE PRESSURE AND ROOM TEMPERATURE UNLESS OTHERWISE SPECIFIED. PRESSURE MEASUREMENTS ARE WITH POSITIVE PRESSURE APPLIED TO PORT B.

NOTE 2: SHIFT IS RELATIVE TO 25°C.

NOTE 3: SHIFT IS WITHIN THE FIRST HOUR OF EXCITATION APPLIED TO THE DEVICE.

NOTE 4: MEASURED AT ONE-HALF FULL SCALE RATED PRESSURE USING BEST STRAIGHT LINE CURVE FIT.

NOTE 5: THE VOLTAGE ADDED TO THE OFFSET VOLTAGE AT FULL SCALE PRESSURE.

Pressure Response: for any pressure applied the response time to get to 90% of pressure applied is typically less than 100 useconds.

All Sensors reserves the right to make changes to any products herein. All Sensors does not assume any liability arising out of the application or use of any product or circuit described herein, neither does it convey any license under its patent rights nor the rights of others.

www.allsensors.com® Signed Original On File

VITA

Chad Eric Seaver is a native of East Tennessee, graduating from Volunteer High School in 1992. He thereafter attended the University of Tennessee where he studied Electrical Engineering with an emphasis on embedded processing. He joined the Oak Ridge National Laboratory's (ORNL) Chemical Technology division in 1995 supporting the development of remotely operated robotics as an Engineering Intern. Upon graduating with his Bachelor of Science degree in Electrical Engineering in 1996, he joined the full-time staff of ORNL continuing to develop remotely operated robotics for hazardous duty environments. He thereafter developed control systems for unmanned autonomous vehicles (UAV) with Northrup Grumman.

Upon joining CTI Molecular Imaging as a Development Engineer in 2000, he began designing medical imaging electronics for positron emission tomography (PET) scanners. Chad advanced to Business Manager with CTI and, upon the company's acquisition by Siemens Medical Solutions, was promoted to Senior Manager. Chad led numerous projects for the Molecular Imaging division of Siemens. His position was responsible for two-dozen direct reports while concurrently and separately leading cross-functional teams for business integration activities and other special projects. Chad co-led the commercialization of the company's first time-of-flight PET tomograph. He additionally led several strategic business engagements with global industry conglomerates, top-tier research universities, and small innovative overseas businesses. While at

Siemens, Chad undertook graduate studies in pursuit of his Master of Science degree in Electrical Engineering. His education focused upon analog electronics for biosensing and medical physics. Chad earned his Professional Engineering licensure in 2011 and thereafter completed his Master of Science degree in 2013. His research thesis was entitled “An Implantable Low Pressure Biosensor Transponder,” which focused upon intracranial pressure sensing. Following completion of his Master’s degree, Chad began doctoral studies in Biomedical Engineering furthering research into the diagnostics of intracranial hypertension.

Chad co-founded and initiated operations of Arkis BioSciences in 2013. As Chief Executive Officer, he currently leads financing, business development, and engineering of the company’s products for advancing the treatments of intracranial hypertension. Chad led the commercialization and 2016 debut of the company’s proprietary minimally invasive surgical instrumentation. He additionally commenced business development leading to an international strategic partnership enabling Arkis to be the first to commercialize fluoropolymer macromolecular additives into the central nervous system. Chad is currently named inventor of eight United States issued patents, five international patents, with numerous others pending. In 2018, Chad completed his Doctor of Philosophy degree in Biomedical Engineering from the University of Tennessee. As a student of the University, he was elected to the Phi Kappa Phi and Tau Beta Pi honor societies. Chad enjoys travel and his hobbies include sailing and diving. He and his wife Patricia are the proud parents of two sons, Alex and Evan.